Title
Influence of the Solar Wind on the Dynamics of Relativistic Electrons in the Earth's Radiation Belts

Author
Pinto Abarzua, Victor Alejandro

Publication Date
2019

UNIVERSITY OF CALIFORNIA
Los Angeles

Influence of the Solar Wind on the Dynamics of Relativistic Electrons in the Earth's Radiation Belts

A dissertation submitted in partial satisfaction
of the requirements for the degree
Doctor of Philosophy in Atmospheric and Oceanic Sciences

by

Victor Alejandro Pinto Abarzua

2019

ABSTRACT OF THE DISSERTATION

Influence of the Solar Wind on the Dynamics of Relativistic Electrons in the Earth's Radiation Belts

by

Victor Alejandro Pinto Abarzua
Doctor of Philosophy in Atmospheric and Oceanic Sciences
University of California, Los Angeles, 2019
Professor Jacob Bortnik, Co-Chair
Professor Lawrence Lyons, Co-Chair

The Earth's electron outer radiation belt is a highly variable region in which the populations can vary by several orders of magnitude in a minute to hours. Such extreme dynamics depends on a complex and delicate balance between source and loss processes that are ultimately driven by the interactions between the interplanetary medium and the Earth's magnetosphere. In recent years, several efforts have been carried out to improve our understanding of the controlling processes driving radiation belt dynamics and to improve the predictability of the relativistic electrons that populate it. In the first part of this dissertation, we study the solar wind parameters that are relevant for the understanding and prediction of relativistic electron enhancement events and relativistic electron persistent depletion events at geostationary orbit and what have the largest potential for prediction. We then use these results to explore the extent of the effects of the solar wind through the outer belt by comparing relativistic electron enhancement events at geostationary orbit with the response at lower radial distances and so try to understand how deep within the inner magnetosphere the solar wind influence can reach. In the second half of this dissertation we explore the recently discovered phenomena of ultrarelativistic remnant belts that can lead to a triple belt configuration of the Earth's radiation belts. Such events were first reported shortly after the launch of the Van Allen Probes mission but are poorly understood. We identify three-belt events to characterize their occurrence rate, and the geomagnetic conditions under which they occur. We investigate their location, characteristic energy and general properties of the magnetosphere and solar wind that can favor their formations. We finally look at remnant belt persistence by statistically calculating their lifetime and decay rates. Using these results, we study the physical mechanism of ultrarelativistic remnant belts decay by comparing with previously reported analytical estimates.

The dissertation of Victor Alejandro Pinto Abarzua is approved.

Vassilis Angelopoulos

Chih-Ping Wang

Lawrence Lyons, Committee Co-Chair

Jacob Bortnik, Committee Co-Chair

University of California, Los Angeles

2019

Para mi familia y mis amigos,
ustedes son la razón de que estas páginas existen.
Pero por sobre todo para Violeta y Tomás,
ustedes son la razón para seguir intentándolo día a día.

TABLE OF CONTENTS

LIST OF FIGURES

LIST OF TABLES

ACKNOWLEDGMENTS

During my years at UCLA I was fortunate to learn from an exceptional group of people. I want to express my deepest gratitude to them as they contributed in many different ways to the completion of this dissertation and made my years in the Ph.D. program a great personal experience.

I would like to start by thanking my co-advisor, Larry Lyons who brought me to the UCLA group, and who taught me how to be disciplined and dedicated to my research work. I would also like to thank my co-advisor Jacob Bortnik who gave me the impulse I needed to turn ideas into written paragraphs, who has constantly encouraged me to become a better scientist and who I now consider a mentor. This dissertation would have never be possible without their help and dedication.

I want to also give special thanks to David Sibeck for inviting me to work during a summer at NASA Goddard Space Flight Center at a period of time where I didn't have a clear vision of how to move forward. I consider that summer visit a critical turning point in my doctoral studies towards a more clearly defined path of research. Along the same line I want to thank my mentor and close friend and collaborator Pablo Moya who has guided and inspired me, and who first suggested that I look at the Van Allen Probes mission data. Turned out to be extremely good advice and several successful collaborations have come to fruition ever since.

Special thanks to Vassilis Angelopoulos and Chih-Ping Wang for being part of my doctoral committee and for putting taking the time and dedication to help me polish my thesis project with important feedback and useful suggestions through the entire process. I want to also thank Richard Thorne and Jochen Stutz who were part of my early committee.

In the past year I had the pleasure to work with an enormous group of very inspiring people at UCLA and different institutions. I want give special thanks to co-authors and collaborators: Didier Mourenas, Christine Gabrielse, Marina Stepanova, Xiaojia Zhang, Anton Artemyev, Elizaveta Antonova, Cristian Farias.

A fundamental part of my studies involved analyzing data provided by the instrument teams of the Van Allen Probes mission. I want to give special thanks to Harlan Spence, Shrikanth Kanekal and Dan Baker for the amazing job they did providing high quality data but also for the feedback they personally gave me while I was involved on investigations that used the ECT-REPT instrument.

Many friends and colleagues have also contributed to my formation and have made my stay at the AOS department a very positive experience. I want to specially thank, Bea Gallardo-Lacourt, Xin An, Tersi Arias, Chao Yue, Xinjin Li, Boyi Wang, Cristian Martinez, David Gonzalez, Katie Tutie, Colin Wilkins, Gonzalo Cortes, Pablo Saide and many others.

Finally, I want to thank my family for their continuous support. Being away from them for a very long time, they have never stopped encouraging me to keep going. Additionally, I want to thank all my friends in Los Angeles, who have always been supportive. I want to specially thank my wife Paulina who had to deal with the long hours of work that were required for the completion of this dissertation. She has always been there for me, and has given me more support than I probably deserved.

Chapter 3 is a modified version of "Pinto, V. A., Kim, H.-J., Lyons, L. R., & Bortnik, J. (2018). Interplanetary parameters leading to relativistic electron enhancement and persistent depletion events at geosynchronous orbit and potential for prediction. J. Geophys. Res. Space Physics, 123, 1134–1145. https://doi.org/10.1002/2017JA024902"

Chapter 5 is a modified version of "Pinto, V. A., Bortnik, J., Moya, P. S., Lyons, L. R., Sibeck, D. G., Kanekal, S. G., et al. (2018). Characteristics, occurrence, and decay rates of remnant belts associated with three-belt events in the Earth's radiation belts. Geophysical Research Letters, 45, 12,099–12,107. https://doi.org/10.1029/2018GL080274"

Chapter 6 is a modified version of "Pinto, V. A., Mourenas, D., Bortnik, J., Zhang, X.-J., Artemyev, A. V., Moya, P. S., & Lyons, L. R. (2019). Decay of ultrarelativistic remnant belt electrons through scattering by plasmaspheric hiss. Journal of Geophysical Research: Space Physics, 124, 5222– 5233. https://doi.org/10.1029/2019JA026509"

The research leading to this dissertation was partially funded by the Becas Chile Doctoral Fellowship from the Chilean government and by NASA grant NNX14AI18G.

VITA

2002–2006	B.S. Physics, Universidad de Chile
2009	**Grant for thesis in Antarctic topics, Chilean Antarctic Institute**
2009–2011	M.S. Physics, Universidad de Chile
2011	**Fellowship for Graduate Studies (Becas Chile)**
2012–014	M.S. Atmospheric and Oceanic Sciences, UCLA
2015–2019	Teaching Fellow (formerly Associate, Assistant) Department of Atmospheric and Oceanic Sciences, UCLA
2016	Visiting Researcher, NASA Goddard Space Flight Center
2017	**AGU Outstanding Student Paper Award**
2019	Graduate Student Researcher Department of Atmospheric and Oceanic Sciences, UCLA

PUBLICATIONS

1. **Pinto, V. A.**, Mourenas, D., Bortnik, J., Zhang, X.-J., Artemyev, A. V., Moya, P. S., & Lyons, L. R.. (2019), Decay of ultrarelativistic remnant belt electrons through scattering by plasmaspheric hiss. Journal of Geophysical Research: Space Physics, 124.
2. **Pinto, V. A.**, Bortnik, J., Moya, P. S., Lyons, L. R., Sibeck, D. G., Kanekal, S. G., et al. (2018). Characteristics, occurrence, and decay rates of remnant belts associated with three-belt events in the Earth's radiation belts. Geophysical Research Letters, 45, 12,099–12,107.

3. **Pinto, V. A.**, Kim, H.-J., Lyons, L. R., & Bortnik, J. (2018). Interplanetary parameters leading to relativistic electron enhancement and persistent depletion events at geosynchronous orbit and potential for prediction. Journal of Geophysical Research: Space Physics, 123, 1134–1145.

4. **Pinto, V. A.,** Stepanova, M., Antonova, E. E., & Valdivia, J. A. (2011). Estimation of the eddy-diffusion coefficients in the plasma sheet using THEMIS satellite data. Journal of Atmospheric and Solar-Terrestrial Physics, 73(11–12), 1472–1477.

5. Gabrielse, C., **Pinto, V. A.**, Nishimura, Y., Lyons, L., Gallardo-Lacourt, B., & Deng, Y. (2019). Storm time mesoscale plasma flows in the nightside high-latitude ionosphere: A statistical survey of characteristics. Geophysical Research Letters, 46, 4079–4088.

6. Stepanova, M., Antonova, E. E., Moya, P. S., **Pinto, V. A.**, & Valdivia, J. A. (2019). Multisatellite analysis of plasma pressure in the inner magnetosphere during the 1 June 2013 geomagnetic storm. Journal of Geophysical Research: Space Physics, 124, 1187–1202.

7. Antonova, E. E., Stepanova, M. V., Moya, P. S., **Pinto, V. A.**, Vovchenko, V. V., Ovchinnikov, I. L., & Sotnikov, N. V. (2018). Processes in auroral oval and outer electron radiation belt. Earth, Planets and Space, 70(1), 127.

8. Farías, C., **Pinto, V. A.**, & Moya, P. S. (2017). What is the temperature of a moving body? Scientific Reports, 7(1), 17657.

9. Moya, P. S., **Pinto, V. A.**, Sibeck, D. G., Kanekal, S. G., & Baker, D. N. (2017). On the effect of geomagnetic storms on relativistic electrons in the outer radiation belt: Van Allen Probes observations. Journal of Geophysical Research: Space Physics, 122, 11,100–11,108.

10. Kim, H.-J., Lyons, L., **Pinto, V. A.**, Wang, C.-P., and Kim, K.-C. (2015), Revisit of relationship between geosynchronous relativistic electron enhancements and magnetic storms, Geophys. Res. Lett., 42, 6155–6161

11. Moya, P. S., **Pinto, V. A.**, Viñas, A. F., Sibeck, D. G., Kurth, W. S., Hospodarsky, G. B., and Wygant, J. R. (2015), Weak kinetic Alfvén waves turbulence during the 14 November 2012 geomagnetic storm: Van Allen Probes observations, J. Geophys. Res. Space Physics, 120, 5504–5523.

CHAPTER 1

Introduction

1.1 The Earth's Magnetosphere

Earth's internal magnetic field can be approximated to first order as a dipolar field. It is believed that Earth's magnetic field is generated by the internal flow of the planet's metal molten core and its dynamics are currently explained through "dynamo theory" (*Parker*, 1955). Earth's magnetic dipole is tilted with respect to the geographical poles by $\sim 11.5°$, and has a surface intensity of $\sim 0.25 - 0.65$ μT. The region of space in which the internal magnetic field of the planet dominates over the interactions between individual particles and their collective behavior is known as the Earth's magnetosphere. Its lower boundary corresponds to the region in which the ionized plasma starts to dominate over the neutral interactions of the atmosphere, usually at an altitude of $\sim 80 - 100$ km from the planet's surface. Its outer boundary corresponds to the region where the magnetospheric magnetic pressure equals the solar wind dynamic pressure. At its closest point, this outer boundary region, —*the magnetopause*— is located around $\sim 67,000$ km, or $\sim 10R_E$ (Earth Radii) in the direction facing towards the sun. The solar wind, blowing constantly away from the sun with speed between $\sim 400 - 600$ km/s impinges in the dayside region of the magnetosphere and compresses it. The same interaction with the solar wind results in an expansion of the magnetic field lines on the nightside region of the Earth, giving the magnetosphere its characteristic form of a tear-shaped cavity with a very extended tail that has an extension up to $80 - 100R_E$. The Earth's magnetosphere is a region in which many complex plasma processes occur, which are driven by both its internal configuration and the external influence of the

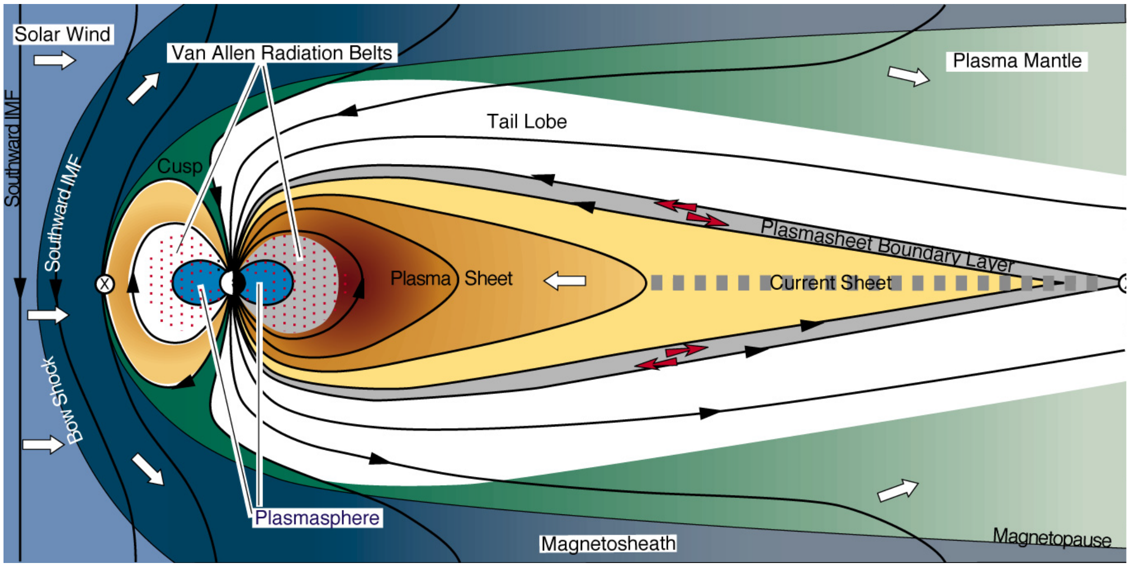

Figure 1.1: Schematic illustration of Earth's magnetosphere in the plane perpendicular to the ecliptic, illustrating major distinct regions. The sun is located towards the left of the image. Figure adapted from *Hill and Dessler* (1991)

solar wind. This results in several different internal regions that can be differentiated by their plasma properties and behavior of the particle populations that reside in them. Figure 1.1 shows a schematic two-dimensional diagram in the plane perpendicular to the ecliptic that describe the locations of the main regions of the Earth's magnetosphere.

The solar wind, flowing at supersonic Alfvén speeds of $\sim 400 - 600$ km/s in the ecliptic plane before encountering the Earth's magnetosphere, must be decelerated upon arrival. This deceleration produces a bow-shock upstream of the magnetopause. The region between the magnetopause location and the bow shock results in thermalized plasma and its known as the magnetosheath. In the nightside of the planet, the stretched magnetic field lines form a tail-like structure. The magnetotail is mainly populated by particles coming from the ionosphere and the solar wind. For the purposes of this dissertation, the magnetotail is important as it provides the seed particles that are injected into the inner magnetosphere and are important for the interactions that lead to the dynamics of the radiation belts. However, regions outside the inner magnetosphere, including the tail dynamics are not going to be discussed extensively.

1.2 Structure of the Inner Magnetosphere

This dissertation will focus on the dynamics of the Earth's radiation belts, located in the Earth's inner magnetosphere. However, the inner magnetosphere is populated by three distinct regions that coexist with each other; the plasmasphere, the ring current and the radiation belts, each of them having their own unique characteristics locations, populations, densities and energies, some of which overlap and many of which interact with each other. Here we present a brief description of these three regions, and their more relevant interactions.

The Van Allen Radiation Belts

The launch of Explorer 1 in 1958 resulted in the discovery of a region of intense radiation at high altitudes. Subsequent experiments led to the discover the Van Allen radiation belts, named after James Van Allen who initially reported the discovery (*Van Allen and Frank*, 1959). The Van Allen radiation belts consist of two distinct regions of the inner magnetosphere populated by highly energetic trapped electrons that are separated by a zone relatively devoid of particles and is located approximately at altitudes between $1.2 \leq R_E \leq 8$. Figure 1.2 is an illustration of the Earth's radiation belts in the plane perpendicular to the ecliptic. Warm colors indicate the regions of greater intensity. The *inner* belt, located approximately in the region $1.2 \leq R_E \leq 2$ is a very stable region and consist mostly of energetic protons of energies as high as 100 MeV and is thought to be populated as a result of cosmic rays interacting with the atmosphere that produce decay of energetic neutrons (*Pizzella et al.*, 1962; *Selesnick et al.*, 2014). The region between $2 \leq R_E \leq 2.5$ is relatively devoid of particles and is referred to as the "slot" region. Particles that enter this region are quickly precipitated into the atmosphere and lost mostly through resonant pitch-angle scattering with waves (*Lyons et al.*, 1972; *Lyons and Thorne*, 1973). The outer zone $2.5 \leq R_E \leq 7$ is populated mostly by energetic *or relativistic* ($>$ 0.5 MeV) electrons and is an extremely dynamic region. Electron populations in the outer zone can be depleted, energized and transported with the result that their fluxes

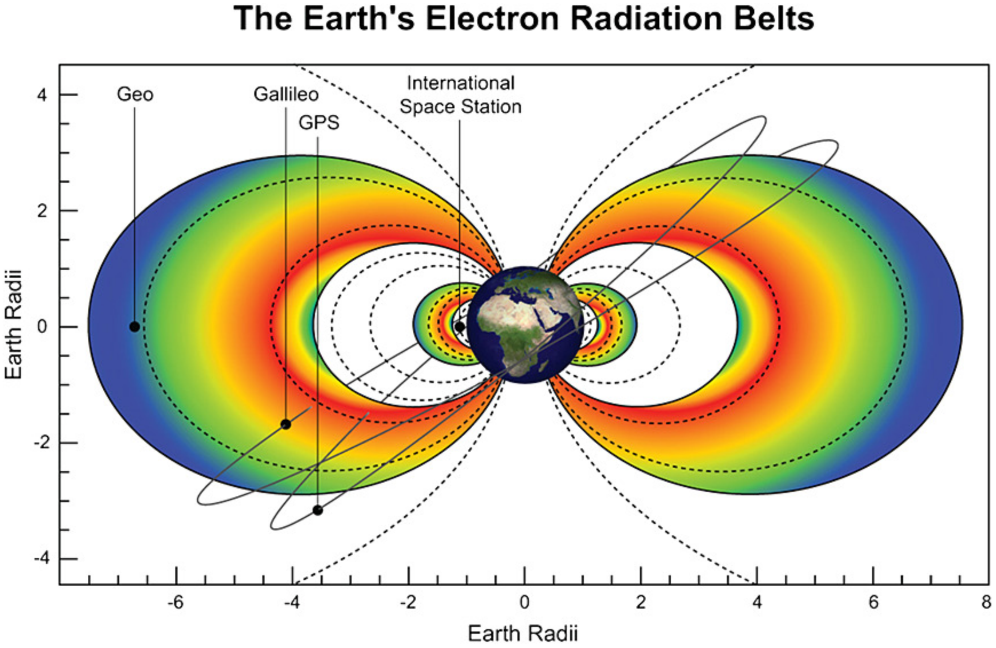

Figure 1.2: Schematic illustration of the Earth's electron radiation belts and some of the most commonly used satellite orbits. Colors represent the intensity (increasing from blue to red) of the stored radiation at different radial distances. Figure from *Horne et al.* (2013)

vary by several orders of magnitude in time periods ranging from hours to a few days (*Baker et al.*, 1994).

It is the outer radiation belt that is the region that has gathered most of the attention in the past several years for both scientific and technical reasons. Fast changes in energetic particle populations pose a significant threat to the instrumentation that orbits the planet (*Baker*, 2000; *Wrenn et al.*, 2002; *Wrenn*, 2009) and are require to be explained by processes strong and fast enough that can provide the required energization and transport conditions in relatively small timescales. The broad range of energies to be studied, the harsh environment and the relatively fast interactions that occur in the radiation belts made it difficult to study in the past, and it is only recently, with the launch of the Van Allen Probes mission that many of this studies have been possible. The Van Allen Belts are the focus of the studies presented in this dissertation and therefore will be explored in depth in the following chapters.

The Ring Current

The ring current is a region of energetic particles (although not relativistic, at energies of $\sim 10-100$ keV), located between $2 \leq R_E \leq 7$ that is composed of electrons and ions drifting longitudinally around the Earth. Because electrons and ions drift in opposite directions due to the gradient and curvature of the Earth's magnetic fields, with electrons drifting to the east and ions to the west, they produce a westward directed current in the magnetosphere. Such current produces a magnetic field perturbation in the opposite direction to the internal magnetic field of the planet, which results in an effectively lower magnetic field that can be measured by ground magnetometers. In fact, early ground measurements have been transformed in useful indices to indicate geomagnetic activity and in particular, the hourly D_{st} index and the similar but 1-minute index, the $SYM-H$ index try to measure the magnetic field depression caused by the Earth's ring current. The main ion component in the ring current is H^+, generally about 85% and as low as 74% during geomagnetic stoms with a certain percentage of energetic heavier ions He^+ (2-5%) originating from solar wind and O^+ from the ionosphere which corresponds to about 6% during quiet conditions and up $\sim$ 20% during active times *Daglis et al.* (1999).

The ring current has a relatively low density compared, for example, to the plasmasphere (typically $1-5$ cm^{-3}, however, the ring current contains the bulk of the energy density in the inner magnetosphere and therefore provides most of the free energy needed for waves growth, considered to be one of the main mechanism for acceleration and losses of radiation belt particles. The ring current strength and composition is highly dependent on geomagnetic activity, and it is the main reason why much of the radiation belt phenomena is closely tied to geomagnetic storms.

The Plasmasphere

The Earth's plasmasphere, first discovered by *Carpenter* (1963), is a region of relatively dense ($\sim 50-10^4$ cm^{-3}) cold plasma ($\sim$ 1 eV) that co-rotates with the Earth and that extends from the ionosphere and up to anywhere between $\sim 3-7$ R_E depending on geomagnetic conditions, with a tendency to expand during quiet geomagnetic conditions, but generally being compressed during active times. Its outer boundary is known as the plasmapause, and corresponds to the region in which the plasma density drops sharply by at least an order of magnitude over less than $0.5R_E$ (*Carpenter and Anderson*, 1992). The region outside the plasmasphere is often referred to as the plasmatrough. Plasmaspheric composition consists of mostly H^+ ions, followed by He^+, O^+, with some heavier ions sometimes observed (*Comfort et al.*, 1988). The cold plasma in the plasmasphere is fundamental in controlling the resonance conditions between plasma waves and the particle populations (e.g. *Chen et al.*, 2009) and is therefore also fundamental for acceleration and loss processes in the radiation belts.

1.3 Single Particle Motion

This section provides a brief introduction to particle motion in near collisionless plasmas, such as the Earth's inner magnetosphere. The following subsections describe the most relevant equations of motion for the trapped particles that reside in the inner magnetosphere, in particular, those in the radiation belts. More information can be found in the books *Basic Space Plasma Physics* (*Baumjohann and Treumann*, 1997), *Introduction to Space Physics* (*Kivelson and Russell*, 1995), *Introduction to Plasma Physics and Controlled Fusion* (*Chen*, 1983) and from the course reader *Solar System Plasma Physics* by professor Richard Thorne at the Department of Atmospheric and Oceanic Sciences, UCLA.

Motion in Uniform Fields

In the presence of an electric and magnetic field, a particle of charge q moving with a velocity $\mathbf{v}$ in a near collisionless plasma (which the magnetosphere can generally assumed to be) will experience a force known as Lorentz force,

$$\frac{d\mathbf{p}}{dt} = q(\mathbf{E} + \mathbf{v} \times \mathbf{B}) \tag{1.1}$$

where $\mathbf{p} = \gamma m \mathbf{v}$ is the particle's momentum and $\gamma = 1/\sqrt{1 - v^2/c^2}$ is the relativistic Lorentz factor. In the general case, when other forces are considered, the equation of motion, will be given by

$$m\frac{d\mathbf{v}}{dt} = q\mathbf{E} + q\mathbf{v} \times \mathbf{B} + \mathbf{F_g} \tag{1.2}$$

where $\mathbf{F_g}$ corresponds to all non electro-magnetic forces, such as the gravitational force. For the regions of the magnetosphere that are of interest to this dissertation, that is, the radiation belts, we can generally assume $\mathbf{F_g} \approx 0$ and therefore negligible compared to the electromagnetic forces. If we consider the particular (and ideal) case of a uniform magnetic field in an arbitrary directions ($\mathbf{B} = B_0\hat{z}$) and no electric field ($\mathbf{E} = 0$), a charged particle will gyrate with cyclotron motion around the field, with an angular frequency (or gyrofrequency) given by

$$\Omega_c = \frac{qB}{m}. \tag{1.3}$$

The gyration radius (*Larmor radius*) is determined by the component of the particle's velocity perpendicular to the background magnetic field and is given by

$$\rho_L = \frac{v_\perp}{\Omega_c} = \frac{m v_\perp}{qB}. \tag{1.4}$$

The gyration motion depend on the charge and mass of the particles, and therefore, positively charged ions and negatively charged electrons will execute trajectories with different gyroradii and in opposite directions. If a finite and uniform electric field $\mathbf{E} \neq 0$ is added in a direction not parallel to the magnetic field, the movement of the particle will now be given by a combination of the magnetic gyration and the electric field effect. In general we can describe this motion as a superposition of the two different motions, this is,

$$\mathbf{r} = \mathbf{R} + \vec{\rho_L} \tag{1.5}$$

with $\mathbf{R}$ the location of the particle's *guiding center* and $\vec{\rho_L}$ the vector Larmor radius. If we choose $\mathbf{E}$ to be such that the electric field components parallel to the magnetic field disappear, that is, $\mathbf{E} \cdot \mathbf{B} = 0$ (a reasonable assumption in magnetospheric plasmas), then,

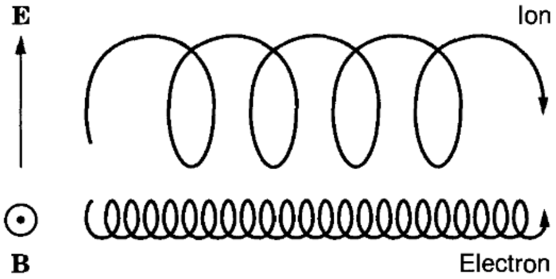

Figure 1.3: Diagram of the $\mathbf{E} \times \mathbf{B}$ drift for electrons and ions in uniform fields. Figure from *Baumjohann and Treumann* (1997)

if $\mathbf{E} = E\hat{x}$ and $\mathbf{B} = B\hat{z}$ we can find a frame of reference in which we know that the acceleration occurs only in the circular motion, we therefore obtain

$$\mathbf{E} + \mathbf{v} \times \mathbf{B} = 0 \tag{1.6}$$

If we take the cross product with $\mathbf{B}$ we have

$$\mathbf{E} \times \mathbf{B} + \mathbf{v} \times \mathbf{B} \times \mathbf{B} = \mathbf{v}B^2 - \mathbf{B}(\mathbf{v} \cdot \mathbf{B}) \tag{1.7}$$

and from the transverse components of this equations we obtain the electric drift of the guiding center

$$\mathbf{v}_E = \frac{\mathbf{E} \times \mathbf{B}}{B^2} \tag{1.8}$$

In this case, v_E is independent of q, m, and $\mathbf{v}_\perp$. The reason is that during the first half of the particles orbit, they gain energy from the electric field and increase their $v_\perp$ and therefore ρ_L. In the second half of the orbit, the particles lose energy and decrease their ρ_L. This difference in the gyroradius on the first and second half of the orbit is responsible for the v_E drift motion. For particles of the same velocity but different mass, the lighter ones will have smaller ρ_L and therefore will drift less per cycle, however, its gyration frequency will also be larger, and the two effects exactly cancel. Two particles of the same mass but different energies would have the same gyrofrequency. The slower one will have smaller ρ_L and therefore will gain less energy from the electric field in half a gyration. For this reason, in collisionless plasmas the electric drift will force the motion of particles in the same direction and speed, as shown in Figure 1.3 and therefore the electric drift will result in no electric currents generated in the system. It is relevant to mention that this drift motion will also occur in the presence of any force **F** such as gravity. However, in such cases the drift will be charge dependent and may result in drift motions in opposite directions, resulting in currents being generated in the system. Equation 1.8 can be written as a general expression to account for the drift motion produced by any force **F** in a uniform magnetic field:

$$\mathbf{v}_F = \frac{\mathbf{F} \times \mathbf{B}}{B^2}. \tag{1.9}$$

Motion in Non-uniform Magnetic Fields

In the most realistic case, inhomogeneities in the magnetic field need to be considered. In the case of spatially changing magnetic fields (such as the Earth's magnetic field), particle motion will be affected by the gradient ∇B in the form of a drift motion if no electric field ($\mathbf{E} = 0$) is present. In the simplest case, we assume a static (or slowly varying) magnetic field with a gradient pointing perpendicular to the direction of the field ($\nabla B \perp \mathbf{B}$). As the particle gyrates, the magnitude of **B** will no longer be constant over its trajectory, and thus, ρ_L will vary in one gyration. Although the process is similar to the process described in the $\mathbf{E} \times \mathbf{B}$ drift, in the case of the ∇B drift, particles of opposite charge drift in opposite directions, and the drift velocity is dependent on the particle's charge, mass, and velocity (energy), and can be described as

$$\mathbf{v}_\nabla = \frac{m v_\perp^2}{2qB^3} \left(\mathbf{B} \times \nabla B \right) \tag{1.10}$$

The gradient drift is only one component of the particle drift in an inhomogeneous magnetic field. When the field lines are curved (such as in a dipolar field), a curvature drift will also be present. Due to their parallel velocity $v_\parallel$, the particles experience a

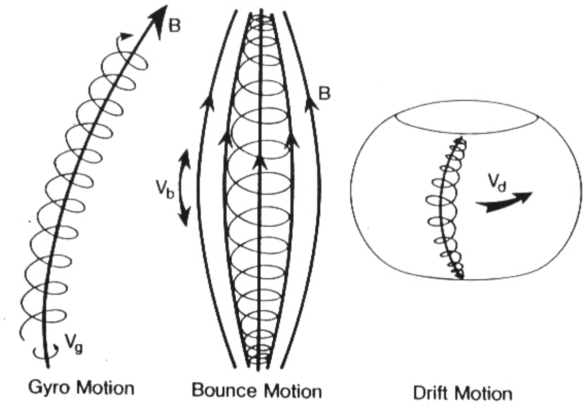

Figure 1.4: Schematic of three different particle motions in a magnetic field occurring in different time scales. Gyro motion, Bounce Motion and Drift Motion with characteristic timescales such that $\tau_{\text{gyro}} \ll \tau_{\text{bounce}} \ll \tau_{\text{drift}}$. Figure from *Kivelson and Russell* (1995).

centrifugal force

$$\mathbf{F_R} = mv_{\|}^2 \frac{\mathbf{R}_c}{R_c^2} \tag{1.11}$$

where $\mathbf{R}_c$ is the radius of curvature. This expression can be replaced in Equation 1.9 to derive the drift caused by a curvature of the magnetic field lines, which results in

$$\mathbf{v}_c = \frac{mv_{\|}^2}{q} \frac{\mathbf{R}_c \times \mathbf{B}}{R_c^2 B^2} \tag{1.12}$$

The curvature drift is thus proportional to the parallel particle energy, $E_{\|} = 1/2mv^2$ and is oriented in a direction that is perpendicular to the magnetic field and its curvature.

Adiabatic Invariants of Motion

Because of the geometry of the Earth's magnetic field, charged particles in the inner magnetosphere can be described, during quiet times, by three different types of motion: 1) gyro-motion around the field lines, 2) bounce motion along the field lines between the mirror points and 3) an azimuthal drift motion around the Earth. Figure 1.4 illustrates these three type of characteristic motions.

The timescales involved in each type of motion are such that $\tau_{\text{gyro}} \ll \tau_{\text{bounce}} \ll \tau_{\text{drift}}$

and thus they can be considered independent of each other most of the time. If the magnetic (and any electric) field is slowly varying, the three types of motion can be considered invariant (or adiabatic invariants). The first adiabatic invariant μ, also known as the magnetic moment, is derived from the fact that a magnetic field does not exert a force over a particle that moves perpendicular to it, and this can be expressed as

$$\mu = \frac{p_\perp^2}{2mB} \tag{1.13}$$

where $p_\perp$ is the relativistic momentum of the particle perpendicular to the local magnetic field, m is the rest mass of the particle and B is the local magnetic field component. The conservation of the first adiabatic invariant is equivalent to the conservation of the magnetic flux through the particle's gyro-orbit. A commonly used quantity to calculate the parallel or perpendicular component of the particle's velocity is the pitch angle, defined as the angle between **v** and **B**. The pitch angle can be expressed as

$$\alpha = \tan^{-1}\left(\frac{v_\perp}{v_\parallel}\right) \tag{1.14}$$

If we consider a particle trapped between two magnetic mirror points, it bounces between them and therefore has a periodic motion given by its "bounce frequency." A constant of this motion is given by the integral of the parallel momentum through the bounce path of the guiding center along a field line. However, since the guiding center drifts across field lines, the guiding center motion is not exactly periodic, and the constant motion is the bounce period which becomes an adiabatic invariant. This invariant is labeled J and is defined for a half-cycle between the two mirror points as

$$J = \int_a^b v_\parallel ds \tag{1.15}$$

and can be re-written in terms of the magnetic field across the path $B(s)$ and the magnetic field at the mirror point B_m which results in

$$J = 2\sqrt{2m\mu}\int_{m_1}^{m_2}\sqrt{B_m - B(s)}ds \tag{1.16}$$

with m_1 and m_2 correspond to the location of the mirror points, and μ is the first adiabatic invariant. This relationship between the first and the second adiabatic invariants is written in a different and more commonly use form by defining

$$K = \int_{m_1}^{m_2}\sqrt{B_m - B(s)}ds \tag{1.17}$$

as the component that only depends on the magnetic field, and therefore

$$J = 2\sqrt{2m\mu}K \tag{1.18}$$

and so the second adiabatic invariant is also written in terms of the first adiabatic invariant μ. Another useful computation is to rewrite K in the form

$$I = \int_{m_1}^{m_2}\sqrt{1 - \frac{B(s)}{B_m}}ds \tag{1.19}$$

which is used in the definition of the McIlwain parameter L *McIlwain* (1961), and that is going to be used extensively through this dissertation and to represent the radial distance from the Earth at which a magnetic field line crosses the equator. Therefore with this definition we can tell that particles bounce through the magnetic field at constant L.

A third invariant invariant of motion, Φ corresponds to the conserved magnetic flux encircled by the periodic orbit of a particle trapped in the magnetic field when it is moving in a closed drift shell orbit around the magnetic field axis. This drift invariant can be written as

$$\Phi = \oint v_d r d\Psi \tag{1.20}$$

where v_d is the perpendicular drift velocity, Ψ is the azimuthal angle and the integration must be performed over a full drift path of the particle. Whenever the typical frequency

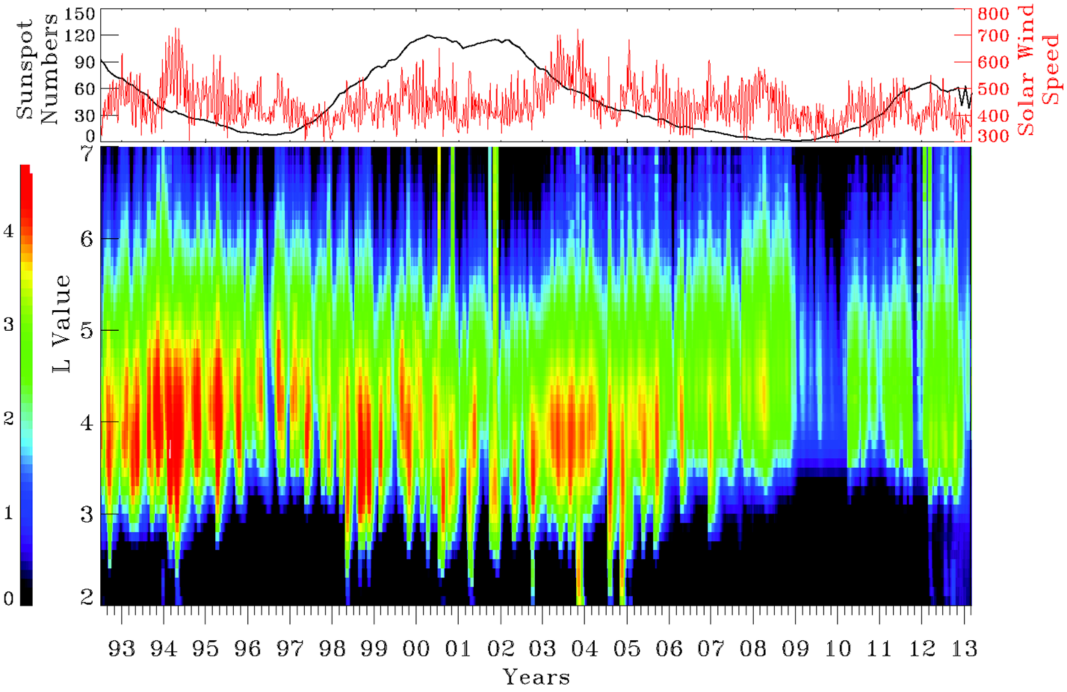

Figure 1.5: Top: sunspot numbers and daily averaged solar wind speed for 20 years, from 1993 to 2013. Bottom: 2-6 MeV electron observations from SAMPEX as a function of L for the same period of time. The color scale on the main plot shows electron flux intensity. Figure from *Baker et al.* (2018)

of the electromagnetic field variation is much smaller than the drift frequency, $\omega \ll \omega_d$, then Φ is invariant and essentially equal to the magnetic flux enclosed by the orbit. This relationship can be expressed as

$$\Phi = \frac{2\pi m}{q^2} M = \text{const.} \tag{1.21}$$

where M is the magnetic moment of the magnetic field. It is often relevant when analyzing the motion of particles in the magnetosphere, to utilize the quantity L^* as the third adiabatic invariant, defined as

$$L^* = \frac{2\pi M}{\Phi R_E} \tag{1.22}$$

1.4 Outer Radiation Belt Dynamics

Fluxes in the outer radiation belt are highly variable. Such variability occurs on both short and long timescales. For example, Figure 1.5 shows low-altitude radiation belt relativistic electron fluxes measured by the Solar Anomalous and Magnetospheric Particle Explorer (SAMPEX) mission from 1993 to 2013. It can be seen that the intensity and location of the electron fluxes varies on short timescales, from days to weeks, but also correlates with long term solar activity, in this case, the sunspot number and hence the $\sim$ 11 year solar cycle. Figure 1.5 is a remarkable example of how outer radiation belt electron fluxes correlate extremely well with solar activity (*Baker et al.*, 1986) and in particular with the solar wind (*Paulikas and Blake*, 1979). The outer radiation belt also responds on time scales of hours to days, usually in association with enhanced geomagnetic activity, that can result in prompt responses, either removing, transporting or energizing particles. Outer radiation belt dynamics have been described as a "delicate equilibrium of acceleration, loss and transport processes" (*Reeves et al.*, 2003), as it is not always straightforward to anticipate or forecast the radiation belt response to a strong geomagnetic disturbance providing free energy to the system. For example, *Reeves et al.* (2003) analyzed geosynchronous data from 276 geomagnetic storms and compared electron fluxes at geostationary orbit before and after each event. They found that the response varied from event to event, with 53% of the storms resulting in enhancement of fluxes, 28% resulting in no significant change, and 19% resulting in depletion of fluxes.

One of the goals of this dissertation is to study the solar wind conditions that favor acceleration or depletion of relativistic electron fluxes in the radiation belts, the influence of the solar wind is ultimately driven by internal processes of the inner magnetosphere and outer radiation belt that result in its extreme dynamics. We describe below the most commonly studied and accepted source and loss processes that act in the outer radiation belts. It is important to mention that the effectiveness of a particular process can vary greatly from event to event, and that in general, these processes do not occur in isolation and often operate at the same time or in rapid succession.

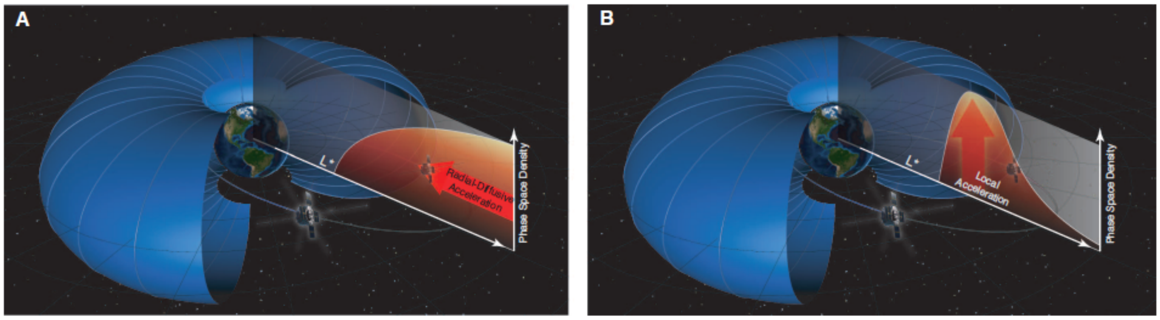

Figure 1.6: Schematic of the outer radiation belt and the two main mechanisms of relativistic electron sources (a) Phase space density expected for radial-diffusive acceleration. (b) Local wave-particle acceleration. Figure from *Reeves et al.* (2013)

Radiation Belt Sources

Sources of energetic particles in the radiation belt are usually the result of non-adiabatic processes that violate one or more adiabatic invariants and can be broadly be separated in two categories: radial transport and acceleration. Figure 1.6 shows a schematic of the outer radiation belt and the phase space density profiles associated with local acceleration and inward radial transport.

Transport of particles generally takes the form of inward radial diffusion and involves motion of particles from the tail region to the inner magnetosphere. It occurs when phase space density gradients appear and allows for particles to diffuse inward to lower L regions (*Schulz and Lanzerotti*, 1974; *Green*, 2004). Since this process violates the third adiabatic invariant of motion, but not the first two, as the particles move into regions of stronger magnetic fields, they are energized. Inward diffusion processes can be enhanced by interactions with magnetospheric ULF waves (e.g. *O'Brien et al.*, 2001; *Mann et al.*, 2004; *Hudson et al.*, 2008) and can also be the result of direct particle injections from the tail generally associated with substorm activity. Although injections could in principle energize electrons up to relativistic energies (e.g. *Schiller et al.*, 2016) they are most commonly responsible for facilitating local acceleration mechanisms.

The second source mechanism is related to local acceleration. Figure 1.7 shows a schematic of the sequence of processes required for strong enhancement of outer belt

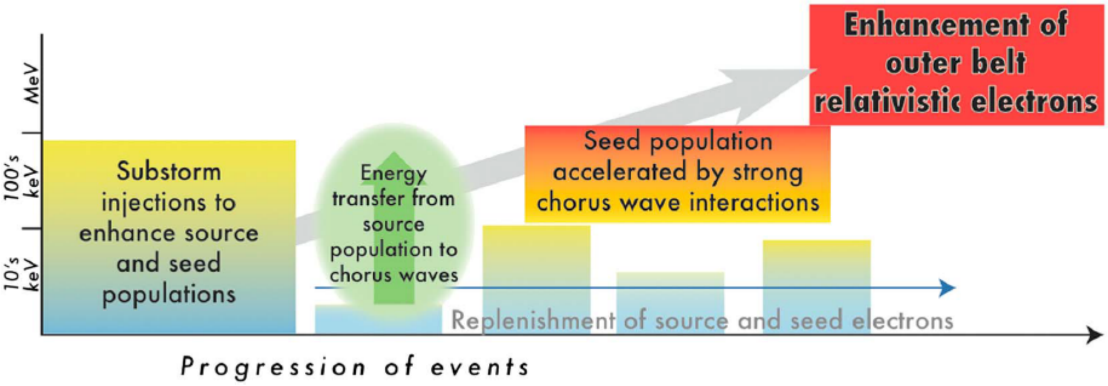

Figure 1.7: Schematic sequence of processes required for strong local acceleration of outer belt electrons to $E > 1$ MeV. Figure from *Jaynes et al.* (2015)

electrons. In this case, favorable solar wind conditions will drive injections of low-to-medium energy electrons (few to hundreds of keV) towards the inner magnetosphere. The low energy electrons, considered the source population, generally exhibit a strong anisotropic distribution by the time they reach the inner magnetosphere (*Thorne et al.*, 2013a) and therefore tend to release energy and feed electromagnetic waves, such as the whistler-mode chorus waves. These waves can then resonantly interact with the medium energy electrons (tens to hundreds of keV) (*Summers et al.*, 1998; *Bortnik and Thorne*, 2007; *Thorne*, 2010) resulting in acceleration up to MeV energies.

Radiation Belt Losses

Radiation belt electrons can also be lost by several different processes. These losses can be true losses or apparent losses due to adiabatic effect (*Kim and Chan*, 1997). In the case that the particles disappear through adiabatic effect (generally associated to the main phase of geomagnetic storms) it is very likely that once the magnetic field recovers, the particles will return to their original position. For the particles to be truly lost from the system, they need to either be pitch-angle scattered towards the loss cone, in which case the electrons get lost into the Earth's atmosphere while undergoing bounce motion (*Jordanova et al.*, 2008; *Hyun et al.*, 2014; *Gao et al.*, 2015) a process that generally requires local wave-particle interactions or the particles can be lost to the interplanetary medium due to magnetopause shadowing (*Turner et al.*, 2012), generally by a combination of outward radial diffusion (*Shprits et al.*, 2006) or simply by a compression of the magnetopause location.

1.5 Solar wind effects on the radiation belts

The variability of the energetic electron fluxes in the Earth's outer radiation belt is ultimately driven by the solar wind. In addition to the long-term variability known to be modulated by the solar cycle (*Baker et al.*, 1986) (and shown in Figure 1.5), large variations occur most of the time on shorter timescales. It is not unusual for the outer radiation belt to experience sudden decreases in flux levels that are typically followed by quick recoveries that occur on hours or days across different radial distances and in a wide energy range. The short and long term variations of relativistic electron flux levels to different solar wind and magnetospheric parameters has been studied extensively, from *Paulikas and Blake* (1979) who reported that high fluxes are linked to the solar wind speed, to other authors who have studied, for example, the variability and orientation of the interplanetary magnetic field B_z (*Blake et al.*, 1997; *O'Brien et al.*, 2001).

A common denominator to most studies of the variability in the outer radiation belt is that they generally focus on the response of the relativistic electron populations to storm-time conditions. As an example, Figure 1.8 shows a superposed epoch time analysis of different solar wind quantities for storms leading to an enhancement in relativistic electron fluxes at geostationary orbit compared to those storms that don't result in enhancement. We will take a similar approach in using the superposed epoch analysis technique for the study of the outer radiation belt, but not restricted exclusively to storm-time. It is our intention to first consider fluxes at geostationary orbit and then expand our study to fluxes across the outer radiation belt, a study made possible with the data provided by the Van Allen Probes Mission

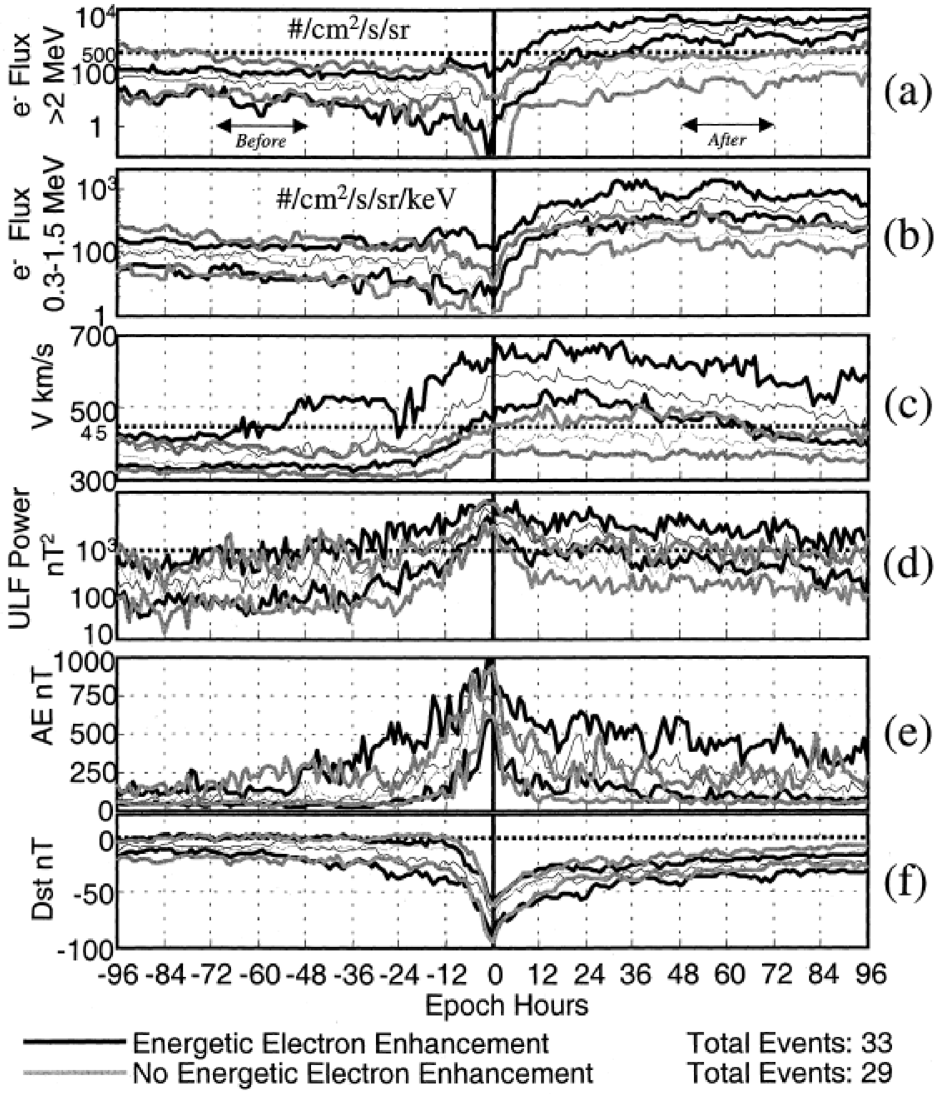

Figure 1.8: From *O'Brien et al.* (2001): The evolution of various quantities as a function of epoch time. Thick lines indicate upper and lower quartiles, and thin lines indicate median values.

Recent discoveries in the radiation belts: The third belt

One of the first results of the Van Allen Probes mission was the discovery of a completely new configuration of the radiation belts, a stable three-belt configuration that lasted for a month before being wiped out by a geomagnetic storm *Baker et al.* (2013a). The creation of this three-belt configuration was the product of a partial depletion of the external outer belt that left a remnant belt at $2.8 < L < 3.5$ and that was later followed by a recovery of electron fluxes at $L > 4$. The consequence of this external recovery is that a

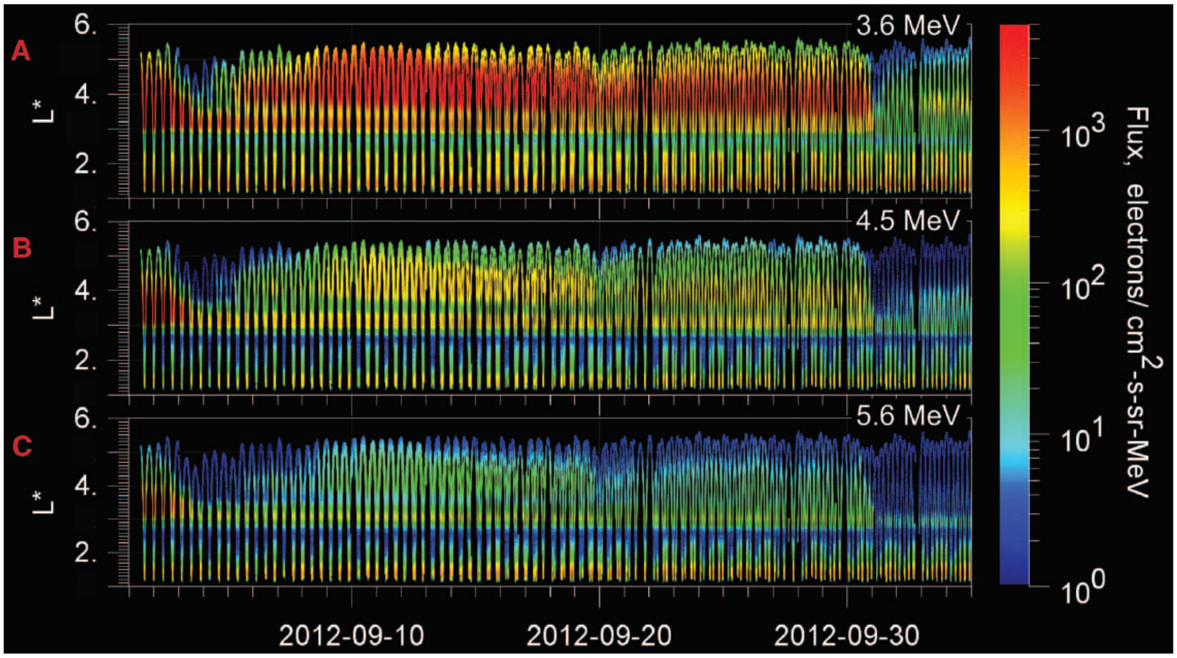

Figure 1.9: Electron fluxes from Van Allen Probes showing a remnant belt and three-belt configuration across several energy channels of the REPT instrument. (a) Electrons in the energy channel $E = 3.4$ MeV (b) Electrons with $E = 4.2$ MeV and (c) Electrons with $E = 5.2$ MeV. Figure from (*Baker et al.*, 2013a).

second "slot" region appeared in between the split outer belt. Figure 1.9 shows the first report of an ultrarelativistic remnant belt.

To explain the formation of the remnant belt, *Shprits et al.* (2013, 2018) has argued that simulation of losses dut to scattering of electrons by electromagnetic ion-cyclotron (EMIC) waves and losses to the interplanetary medium can successfully replicate the remnant belt formation, while *Mann et al.* (2016, 2018) has argued that EMIC waves scattering is not needed as losses to the magnetopause by a combination of traditional inward motion of the magnetopause and fast outward diffusion driven by ULF waves is enough to replicate the observations. The decay of the remnant belt has been studied by *Thorne et al.* (2013b) who argued that that a remnant belt trapped in the plasmasphere by a rapid expansion of the plasmapause will only present a slow decay associated with interactions with hiss waves. It is our intention to explore the phenomenon of the ultrarelativistic electron remnant belts associated with three-belt events in the outer radiation belt.

1.6 Objectives and Organization of the Dissertation

The major goals of this dissertation are

1. Establish what solar wind parameters are statistically relevant for enhancement and depletion events of MeV electrons at geostationary orbit regardless of storm-time conditions
2. Study the extent of the solar wind influence for the entire outer belt, by investigating to what extent enhancements of MeV electrons occurring at geostationary orbit will penetrate to lower L-shells
3. Improve our understand the morphology of the radiation belts, in particular of remnant belt of ultrarelativistic electrons that form at low L-shells by exploring their occurrence, location and decay mechanisms.

Chapter 2 describes the main datasets we are going to use, in particular the Van Allen Probes instruments and characteristics of the mission and the processing of the REPT data. In Chapter 3 we present the study *Interplanetary Parameters Leading to Relativistic Electron Enhancement and Persistent Depletion Events at Geosynchronous Orbit and Potential for Prediction* were we study the statistical state of the solar wind during relativistic electron enhancement events and persistent depletions at geostationary orbit. In Chapter 4 we present the study *Radial Response of Outer Radiation Belt Relativistic Electrons During Enhancement Events at Geostationary Orbit* that explores the response of the outer radiation belt during enhancement events detected at geostationary orbit and study the coherence in the response of different parts of the radiation belt. Chapter 5 corresponds to the study *Characteristics, Occurrence and Decay Rates of Remnant Belts associated with Three-Belt events in the Earth's Radiation Belts* that characterize the occurrence and main properties of ultrarelativistic remnant belts associated with three-belt events in the outer radiation belt. Chapter 6, the study entitled *Decay of Ultrarelativistic Remnant Belt Electrons Through Scattering by Plasmaspheric Hiss* extends the previous study by exploring in detail the mechanisms responsible for the slow decay of ultrarelativistic remnant belts. Finally, Chapter 7 presents a summary of the findings in this dissertation.

CHAPTER 2

Datasets and Data Processing

2.1 The Van Allen Probes Mission

The Van Allen Probes mission (*Mauk et al.*, 2013), formerly known as the Radiation Belt Storm Probes, consisted of two identical spacecraft, named RBSP-A and RBSP-B that were designed to survey the different particle populations and fields in the inner magnetosphere with emphasis in the extreme dynamics of the Earth's radiation belts. Both spacecraft carried a comprehensive suite of instruments designed for such purposes. The spacecraft were located in nearly identical highly elliptical, near-equatorial ($\sim 10^\circ$ inclination) orbits with an apogee at 5.8 R_E (geostationary transfer orbit), an orbital period of $\sim$ 9 hours, and a spin period of $\sim$ 11 seconds.

The satellites were designed to have a precession rate of $\sim 210^\circ$/year, so that their apogee-perigee line covered all magnetic local times (MLT) every $\sim$ 20 months. The individual orbits of the probes were slightly different so that one satellite overtakes the other every $\sim$2.5 months, allowing for measurements at variable distances between the two probes, simultaneous measures at different radial distances from the Earth and measurements at different MLT separation.

The mission was launch on an Atlas V 401 rocket on August 30, 2012, and some instruments turned on the following days. Relativistic electrons from REPT (the central pillar of this dissertation) are available starting September 3, 2012. The spacecraft started their decommission process in February 2019 with the lowering of their perigee orbits so that atmospheric drag eventually results in a re-entry to the atmosphere. It is expected that this re-entry will occur at some point in 2034. After running out of fuel, needed

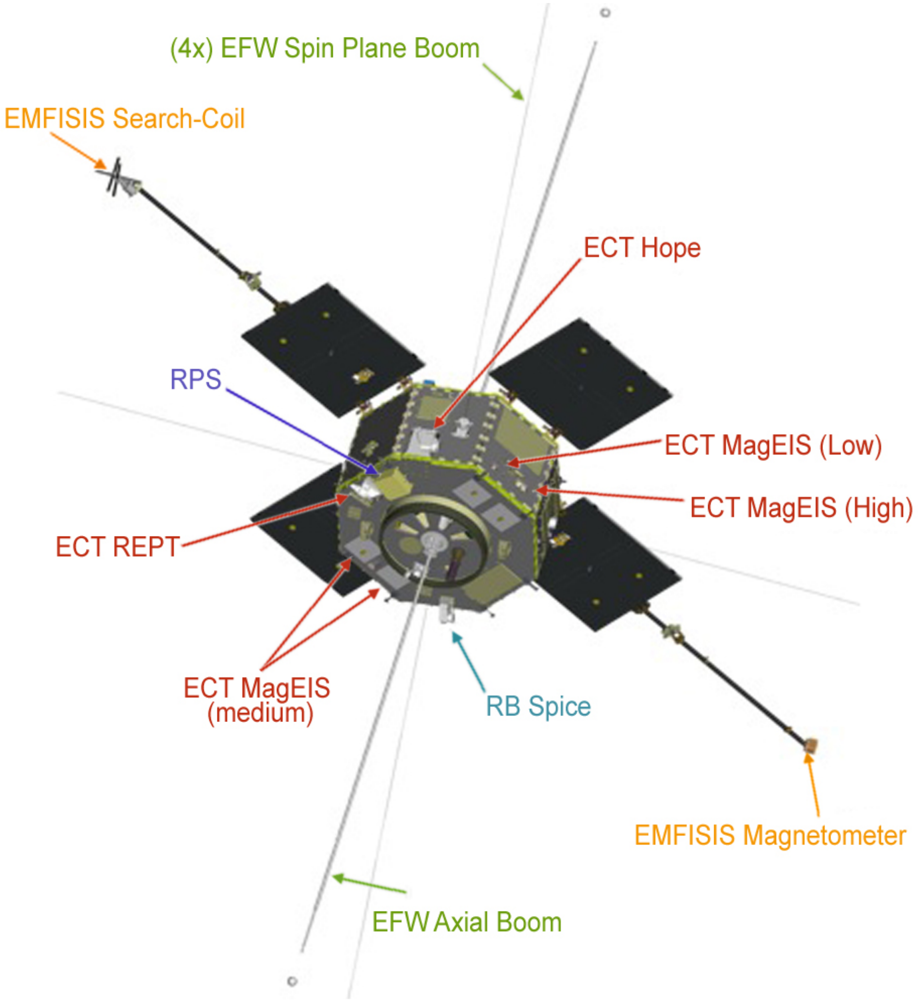

Figure 2.1: Rendered illustration of the Van Allen Probes and the location of the on-board suites of instruments carried by the mission. Source: NASA Van Allen Probes website (`http://nasa.gov/mission_pages/rbsp/spacecraft`)

to maintain the satellites pointing their solar panels in the direction of the sun, on July 19, 2019, RBSP-B was deactivated, and RBSP-A followed on October 18, 2019, in what is considered the official end of the mission. Figure 2.1 shows a diagram of the configuration of the Van Allen Probes suites of instruments. Of all the available instruments and measurements from the Van Allen Probes mission, we now describe the two we have used for the research presented in this dissertation: The ECT-REPT instrument and the EMFIFIS instrument.

ECT-REPT

The Relativistic Electron-Proton Telescope (REPT) instrument (*Baker et al.*, 2013b) was part of the Energetic Particle, Composition and Thermal Plasma (ECT) suite (*Spence et al.*, 2013). Designed to measure relativistic particles, REPT measures full pitch-angle distributions in the energy range from 1.6 MeV to $>$18.9 MeV for electrons, with an energy resolution $\Delta E/E$ 25% which results in 12 energy channels and from 17 MeV to $>$100 MeV for protons, with an energy resolution $\Delta E/E$ 25% resulting in 8 energy channels.

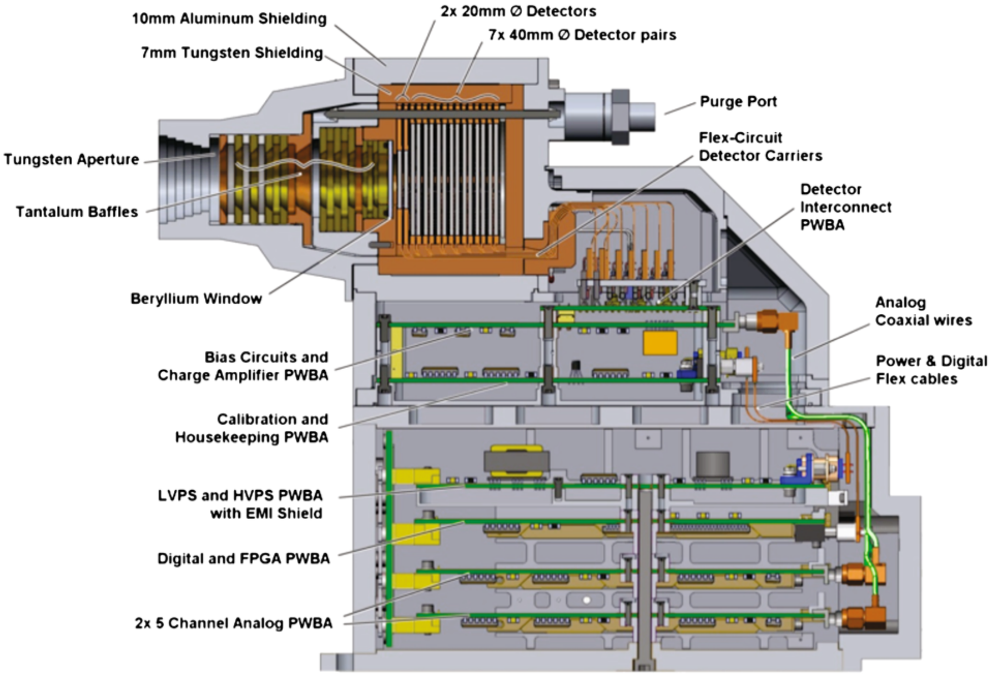

Figure 2.2: Profile diagram of the REPT instrument showing high-Z disk-loaded collimator, detectors and shielding along with the supporting electronics. Figure from *Baker et al.* (2013b)

Figure 2.2 shows a diagram of the REPT instrument, which pointed perpendicular to the spin axis of the spacecraft. REPT consisted of a stack of nine silicon solid state detectors placed behind a collimator and thick aluminum-tungsten protective casing and shielding. A beryllium window at the back of the collimator was in place to exclude electrons low energy electrons of $E < 1$ MeV and protons $E < 15$ MeV. The instrument has a geometric factor of 0.2 cm^2 sr and a field of view of 32°. Processing of the electron data is made available both as a sector measurements (L2) and pitch-angle resolved (L3) data that contains 17 pitch angles from $0^\circ - 180^\circ$. For this dissertation we used L3 pitch-angle resolved data, which is available in the instrument team website (`https://www.rbsp-ect.lanl.gov`).

EMFISIS

The Electric and Magnetic Field Instrument Suite and Integrated Science (EMFISIS) instrument *Kletzing et al.* (2013) suite provided measurements of DC magnetic fields and wave electric and magnetic fields covering the frequency range from 10 Hz up to 12 kHz (400 kHz for single-axis electric field. There were two sensors in EMFISIS: a tri-axial fluxgate magnetometer (MAG), and a tri-axial magnetic search coil magnetometer (MSC). The Waves instrument used signals from both the MSC and electric field measurements from the Electric Fields and Waves (EFW) instrument (*Wygant et al.*, 2013). The EMFISIS magnetic field sensors were mounted on booms as shown in Figure 2.1.

Several products are available from the EMFISIS instrument, including low cadence continuous survey and burst products such as magnetic field, HFR-spectra and WFR-waveforms (L2, calibrated in spacecraft coordinates), as well as magnetic fields in different coordinates (L3) in both high and low temporal resolution. Finally, the EMFIFIS team has produced some high-level processed data (L4) of which in this dissertation we will use the electron density obtained from the upper hybrid resonance f_{uh} (*Kurth et al.*, 2015). EMFISIS data is available in the instrument team website (`https://emfisis.physics.uiowa.edu/`)

2.2 GOES Data

The Geostationary Operational Environmental Satellite (GOES) (*Onsager et al.*, 1996) is the National Oceanic and Atmospheric Administration (NOAA) main environmental monitor for Earth and space. Orbiting the Earth in geosynchronous orbit, at about 6.6

R_E (35,800 km), the monitoring has been active since 1974, although the relevant space data for this dissertation, the relativistic electrons, has been available continually only since GOES-8 was launched in 1994. There is generally two GOES satellites operating at the same time, GOES-East positioned over the equator at 75 degrees West longitude, and the GOES-West satellite is positioned at 135 degrees West longitude. All of them, starting with GOES-8 carry a Space Environment Monitor (SEM) instrument which consists of a three-axis fluxgate magnetometer, energetic particle detector, and soft X-ray detector. Newer generations of GOES satellites (starting with GOES-13) also carry a medium energy particle detector. In this dissertation, we will use data from the GOES-8 (1996-2003) and GOES-10 (2003-2006) relativistic electron fluxes > 2 MeV sampled at 5 minutes of temporal resolution by the Energetic Particle Sensor (EPS) instrument (*Onsager et al.*, 1996) and from the Energetic Proton, Electrons and Alpha particles Detector (EPEAD) instrument (*Rodriguez et al.*, 2014) for GOES 15 (2012-2017).

Data from the GOES satellites has only been minimally processed, and generally to remove contamination from energetic protons (GOES-8 and GOES-10) or to obtain hourly or daily averages. All data used in this dissertation is available in the NOAA website (`https://satdat.ngdc.noaa.gov/sem/goes/data/`).

2.3 OMNI Data

The OMNI (currently OMNI-2) data set contains hourly, 1-minute and 5-minutes resolution of the solar wind magnetic field and plasma properties obtained from many spacecraft in geocentric orbit, in orbit about the L1 Lagrange point $\sim 225 R_E$ in front of the Earth among others. Since the creation of the minute datasets in 1995, the main contributors to the OMNI dataset have been the ACE, Wind and IMP 8 spacecraft. In recent years, data from Geotail and GOES has been added. The data set also contains geomagnetic activity indices (AE, D_{st}, etc.) and sunspot numbers.

Processing of the data includes time-shifting to the Earth's bow shock nose. Time shifting is based on the assumption that solar wind magnetic field values observed by a spacecraft at a given time and place lie on a planar surface convecting with the solar wind, and that the same values will be seen at a different place at the time that the phase front sweeps over that location, commonly referred to as "ballistic propagation". Specific details about the data processing and availability can be found in the OMNI website (`https://omniweb.gsfc.nasa.gov`)

For this dissertation we will mostly use the 1-minute resolved OMNI data except when certain quantities are not available, for example, D_{st} and Kp index are only available in hourly resolution. All the data used in this dissertation is available in the Coordinated Data Analysis Web (CDAWeb) repository (`https://cdaweb.gsfc.nasa.gov/`)

2.4 Data Processing

The data used in this dissertation is publicly available and generally pre-processed such that it can be used with minimal manipulation. During the following chapters, some derived quantities will be calculated, such as, for example, the southward (negative) accumulated interplanetary magnetic field B_z component. When a derived quantity is calculated, it will be described within the text.

One particular type of processing for the data that was used several times in this dissertation and that is worth disussing separately, is the binning of the Van Allen Probes REPT data in time and sometimes in space. Originally presented in 17 pitch angle bins and 12 energy channels, the L3 REPT data is sampled at 11 seconds (one measurement per satellite spin). For our research purposes, such high temporal resolution is not needed and it can significantly slow down the calculations when analyzing several days, months or even years of data. Therefore, the following standard procedures were applied to REPT data.

1. Individual daily files were processed by taking a simple geometric average of all pitch angle bins, and therefore changing from unidirectional fluxes to omnidirectional fluxes

2. The first 8 energy channels were kept and the 4 more energetic channels were dropped from the data since they rarely present useful information and therefore were not considered during this dissertation.

3. These daily files were combined into monthly files containing only electron data for the first 8 channels, time, and location of the satellites given in L and MLT format. Although these files are not published, they can be requested to me by email, as well as the processing routines (written in IDL)

The simplified dataset was used for the different studies carried out in this dissertation. Additionally, several other processing steps were carried out, and that are described in each chapter to account for small differences between studies. However, the general guidelines are the following

1. **Spatial binning of the datasets:** Considering that fast variations in fluxes were not fundamental to our purposes, and to reduce the size of the database to only one measurement for each satellite for each L every $\Delta L = 0.1$, we performed a binning by averaging all the data points available for that particular pass of the satellite in the region $L \leq r < L + 0.1$ with r the actual position of the satellite (in L units). The time of that measurement was chosen as the median time of the collection of points

2. **Merging of the datasets:** Most of the time data from RBSP-A and RBSP-B was merged to obtain a single dataset that contained all measurements from both satellites. This was done by simply combining both datasets and sorting them by time, without preservation of the identity of each probe. This merging allowed for increased temporal resolution of data for each L-shell, at the cost of presenting some variability given the slight differences in the satellites orbits.

3. **Temporal binning of the datasets:** For some studies, high temporal resolution was not as important as consistent time-dependent measurements. When that was the case, we performed a temporal binning in the merged datasets for a particular

$\Delta L = 0.1$ by by averaging all the measurements at that particular L within a time range of typically $\Delta t = 6$ hours. Although different studies used particular binning time, 6 hours produces consistent non null results in the range $2.5 \leq L \leq 6.0$, although sometimes a binning of $\Delta t = 4.5$ hours also produces satisfactory datasets

Background removal was performed depending on the particular needs of the investigation. The general background removal mechanism used for this dissertation was first presented in *Moya et al.* (2017) and follows the guidelines described by *Claudepierre et al.* (2015).

CHAPTER 3

Interplanetary Parameters Leading to Relativistic Electron Enhancement and Persistent Depletion Events at Geosynchronous Orbit and Potential for Prediction

The material in this chapter has already been published in the *Journal of Geophysical Research: Space Physics* (*Pinto et al.*, 2018a). The text is presented with some minor modifications to the original to include the supplementary information of the original published work.

3.1 Introduction

Fluxes of relativistic electron populations ($>$ 0.5 MeV) in the Earth's outer radiation belt are highly variable. There is a long-term variability that has been suggested to be modulated by the solar cycle (*Baker et al.*, 1986), but large variations also occur on short time scales. For example, sudden drops in flux levels that are typically followed by quick recoveries can occur on timescales of hours or days. Numerous studies have linked the short and long term variations of relativistic electron flux levels to different solar wind and magnetospheric parameters; the solar wind velocity (*Paulikas and Blake*, 1979; *Blake et al.*, 1997; *Baker et al.*, 1998; *Lyons et al.*, 2005, 2009; *Reeves et al.*, 2011; *Wing et al.*, 2016), showing that high-speed streams are favorable for increases in flux, the change and orientation of the interplanetary magnetic field B_z (*Blake et al.*, 1997; *O'Brien et al.*, 2001; *Iles et al.*, 2002; *Li et al.*, 2005; *Miyoshi and Kataoka*, 2008; *Gao et al.*, 2015; *Boynton et al.*, 2016), the solar wind proton density (*Lyons et al.*, 2005; *Lyatsky and Khazanov*, 2008;

Borovsky and Denton, 2010; *Balikhin et al.*, 2011), the auroral activity measured by the AE index (*Meredith*, 2002, 2003; *Li et al.*, 2009; *Kim et al.*, 2015; *Hajra et al.*, 2015) and the solar wind or magnetospheric ULF wave activity (*Rostoker et al.*, 1998; *Kim et al.*, 2006; *Kozyreva et al.*, 2007; *Potapov et al.*, 2014).

The physical processes that lead to the variations in relativistic electron fluxes in the outer radiation belt have been another important area of study. While the topic is still open, it is generally accepted that the main processes for relativistic electron losses are magnetopause shadowing (*Turner et al.*, 2012), outward radial diffusion (*Shprits et al.*, 2006) and pitch angle scattering to the atmosphere (*Thorne et al.*, 2013b; *Hyun et al.*, 2014; *Gao et al.*, 2015). For electron acceleration leading to an increase in relativistic electron fluxes, we point to wave-particle interactions (*Summers et al.*, 1998; *Bortnik and Thorne*, 2007; *Horne et al.*, 2007; *Thorne*, 2010) acting on a seed population and resonance with ULF wave activity (*Mathie and Mann*, 2000; *Mann et al.*, 2013) as the main causes. Understanding the processes that lead to variability is a major goal of radiation belt research. However, when it comes to applications, and in particular prediction, we need a better understanding of the external factors driving the relativistic electron fluxes, as it has become clear that elevated fluxes can damage satellites in geostationary orbit (*Baker*, 2000; *Wrenn et al.*, 2002; *Wrenn*, 2009), disrupt communications and pose a threat for space exploration. Therefore, having the ability to predict the outer belt variability accurately has important technical applications and several efforts have been conducted in this regard (*Baker et al.*, 1990; *Reeves*, 1998; *Li et al.*, 2001; *Turner and Li*, 2008; *McPherron et al.*, 2009; *Simms et al.*, 2014; *Boynton et al.*, 2015; *Simms et al.*, 2016).

Relativistic electron flux variations have been historically associated with geomagnetic storms (e.g., *Gonzalez et al.*, 1994), with a common proposition that storms are accompanied by a drop in the electron flux during the storm main phase followed by a recovery or increase during the storm recovery phase (e.g., *Reeves*, 1998). Even though this association is relatively common, not all storms result in enhancements from pre-storm levels. For example, *Reeves et al.* (2003) studied 276 storms and only 53% were associated with an enhancement event at geostationary orbit, while 19% were associated with a net flux loss and 28% showed no significant change. Similar results have been obtained in other studies (e.g., *Turner et al.*, 2013; *Zhao and Li*, 2013; *Moya et al.*, 2017), giving us confirmation that storms are not always associated with enhancement or depletion in relativistic electron fluxes.

To better understand the geomagnetic conditions needed for the fluxes of relativistic electrons to be enhanced or depleted, it is very important to study the problem from a non D_{st}-based point of view. By using D_{st} minima during storm to locate events, we restrict the studies to only a subset of all events and therefore limit our capacity to fully understand the enhancement and depletion phenomena and to develop fully functional predictive capabilities. For example, starting from enhancement events, *Kim et al.* (2015) showed that a geomagnetic storm, as defined by a drop in D_{st} index, is not necessary for a relativistic electron enhancement event to occur and that a persistent southward IMF or north-south IMF oscillations that can drive sufficiently large substorm activity as measured by AE index are key for enhancements occurrence (see also *Hajra et al.*, 2015; *Rodger et al.*, 2016, and references therein).

In this work, we study two types of events associated with flux variations: relativistic electron enhancement events and relativistic electron persistent depletion events that occurred during the years between 1996 and 2006. We examine various solar wind parameters that are associated with them to understand if there are critical parameters involved in the processes of enhancement or persistent depletion. Section 3.2 describes the event selection criteria and the data used for the study. Section 3.3 presents the results of a superposed epoch analysis of the events and cumulative distribution analysis for various solar wind parameters for both enhancement and persistent depletion events and the comparison between them. Section 3.4 discusses some ideas about the predictability of relativistic electron enhancement events and persistent depletion events based on our results

3.2 Selection of Events and Data

We use > 2 MeV electron flux data sampled at 5 minutes by the Energetic Particle Sensor (EPS) instrument on-board the Geostationary Operational Environmental Satellite (*Onsager et al.*, 1996) GOES-8 (1996–2003), and GOES-10 (2003–2006) satellites located at geostationary orbit to identify the events to study, and GOES-11 (2007–2010) to test the predictive power of the results. To avoid background contamination from energetic solar protons, we have used NOAA definition of solar proton events (SEP) of > 10 cm^{-2} sr^{-1} s^{-1} in the > 10 MeV proton channel as a criterion for exclusion if they were measured during the first two days following the start of our events. Relativistic electron enhancement events (REE) are defined by an increase in the minimum daily flux from less than 10^2 cm^{-2} sr^{-1} s^{-1} to more than 2×10^3 cm^{-2} sr^{-1} s^{-1} in less than 48 hours, followed by an average daily flux larger than 0.5×10^3 cm^{-2} sr^{-1} s^{-1} for at least 3 days, and a relative increase of at least a factor of 4 for the flux daily average. Time t=0 corresponds to the time when the increase in flux initiates. Relativistic electron persistent depletion events (REPDE) are defined as a drop to less than 10^1 cm^{-2} sr^{-1} s^{-1} in the maximum daily flux resulting in a decrease of a factor of 4 or more with respect to the pre-drop flux and with daily average flux remaining below 10^1 cm $^{-2}$ sr^{-1} s^{-1} for at least 3 days. For REPDE, time t=0 is determined by the time at which flux reaches its minimum value after the initial drop. Figure 3.1 shows a schematic of the electron flux evolution for REE and REPDE. During the period covered by this study, from 1996 to 2006, we identified 61 REE and 21 REPDE.

To study solar wind parameters, we use the OMNI database that provides 1-minute temporal resolution data obtained from ACE, WIND and IMP-8 satellites processed to be shifted to the position of the Earth's bow shock nose, and that can be obtained through CDAWeb (`http://cdaweb.gsfc.nasa.gov`). IMF ULF index corresponds to a 1-hour average of the spectral power in the Pc5 range (1–8 mHz) calculated from WIND, ACE and IMP-8 1 minute resolution IMF data time-shifted to the magnetopause nose using the method of *Kozyreva et al.* (2007), and the data can be obtained from the Augsburg website

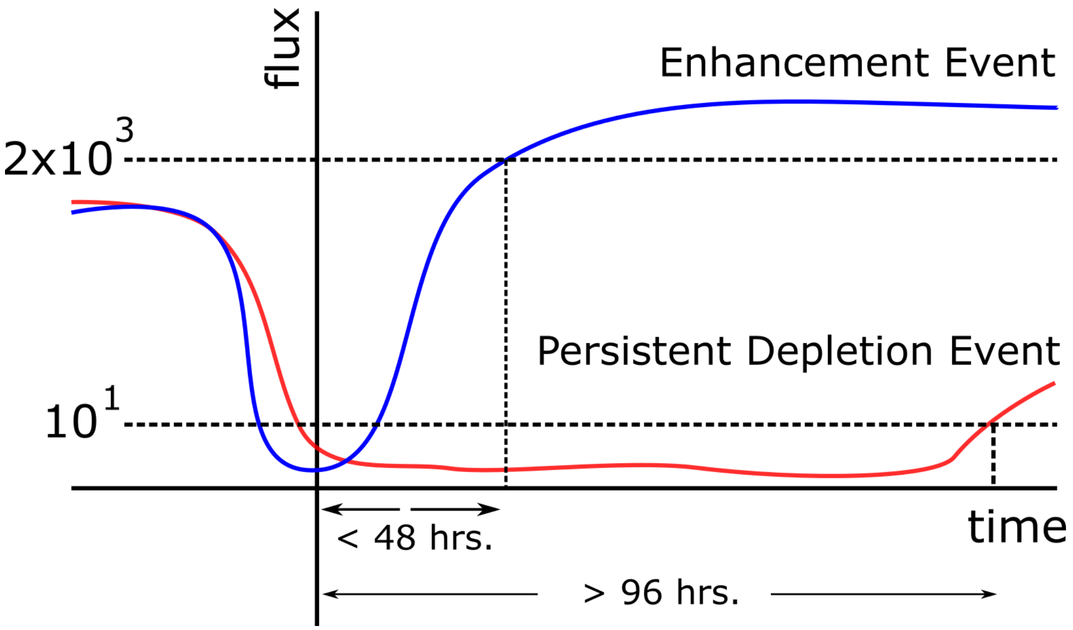

Figure 3.1: Scheme of the flux evolution for an idealized relativistic electron enhancement event (red) and a relativistic electron persistent depletion event (blue). $t = 0$ corresponds to the time when the enhancement can be first appreciated (REE) or when the depletion is complete (REPDE), vertical dashed lines represent the time in which threshold value should be reached for REE and the minimum duration allowed for persistent depletions.

(`http://space.augsburg.edu/MACCS/ULF_index`). IMF ULF power is then calculated as 10^{index} with a 1-hour resolution.

We have also cataloged the events by their associated solar driver, i.e. Interplanetary Coronal Mass Ejection (CME) or Co-rotating Interaction Region (CIR). The identification of the solar wind driver was based on the observation of solar wind speed changes (V_x and V_y), proton density changes, and IMF B_z response around the time of the events. For REE, 53 events are associated with a CIR and 8 with a CME, while for REPDE, 18 are associated with a CIR and 3 with a CME. The full list of events with their respective start times and geomagnetic drivers is shown in Table 3.1 for REE events and in Table 3.2 for REPDE events.

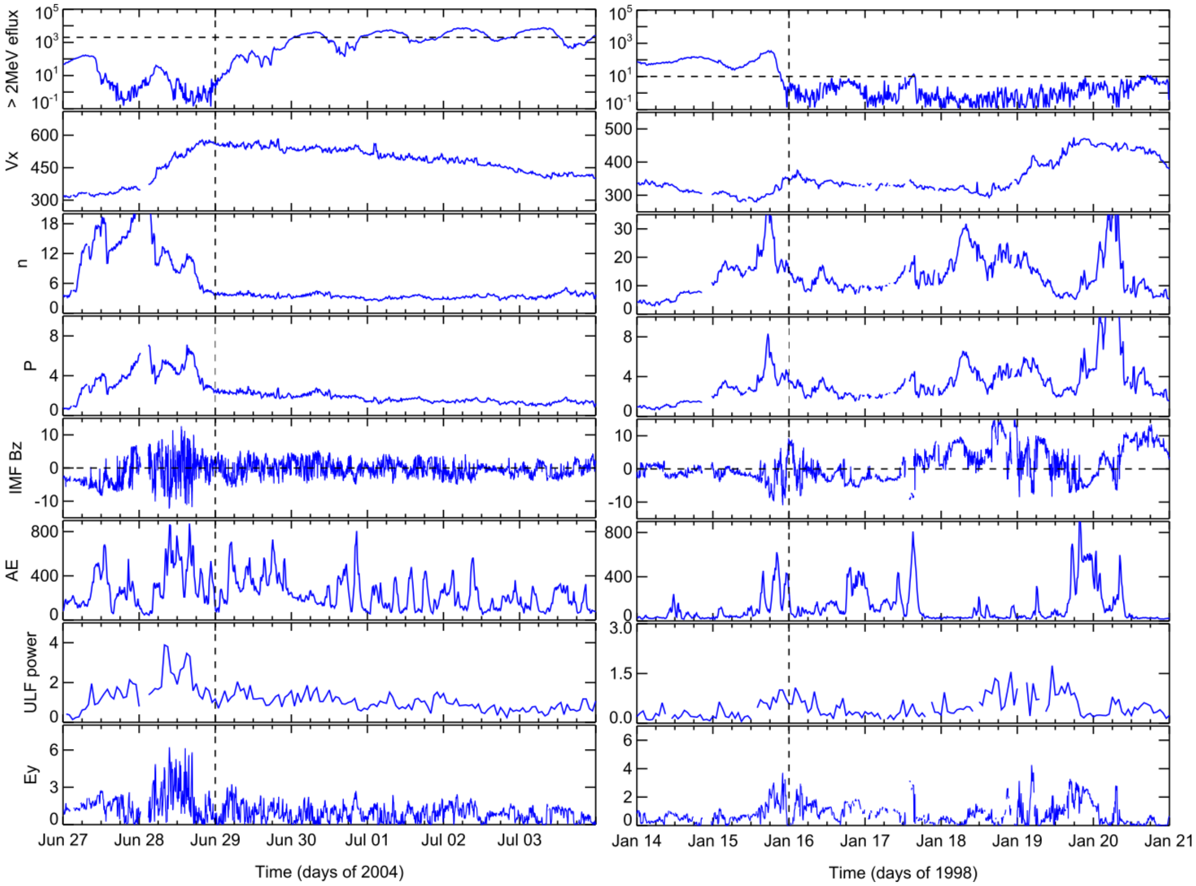

Figure 3.2: Example of a relativistic electron enhancement event occurred on 29 June 2004 (left) and persistent depletion event occurred on 16 January 1998 (right). From top to bottom, panels show: $>$ 2 MeV electron flux (cm^{-2} sr^{-1} s^{-1}) from GOES, solar wind speed V_x (km/s), solar wind proton density n (cm^{-3}), solar wind dynamic pressure p_{dyn} (nPa), interplanetary magnetic field (IMF) B_z (nT), AE Index (nT), solar wind ULF power (nT^2) and solar wind reconnection electric field E_y (mV/m). Vertical dashed line indicates the time $t = 0$; enhancement start or depletion of flux.

3.3 Superposed epoch time analysis

Figure 3.2 shows an example of a relativistic electron enhancement event that occurred on 29 June 2004 (left) and a relativistic electron persistent depletion event that occurred on 16 January 1998 (right). For both events, we also show the different parameters that are considered in this work; from top to bottom: solar wind speed V_x, solar wind proton density n_{sw}, solar wind dynamic pressure p_{dyn}, interplanetary magnetic field B_z, AE index, IMF ULF power and solar wind reconnection electric field E_y component (*Kan and Lee*, 1979). Note that the SYM-H index has been deliberately excluded because we collected our events without considering SYM-H drops. To examine a possible SYM-H influence, Figure 3.3 shows the time difference between the SYM-H minimum value for each individual event and the time we have labeled as t=0. Negative values indicate that SYM-H minimum occurred before time t=0. We have indicated in red the events associated with a CME and in blue those associated with a CIR. While a spread in time is expected, it is interesting to note that relativistic enhancement event can start before SYM-H minimum when that minimum is modest, and there are several enhancement events for SYM-H minimum > -50 nT, which are not traditionally considered geomagnetic storms. For persistent depletion events, we would expect the SYM-H minimum to occur at positive time (after flux minimum) if we assume depletions occur during the storm main phase. However, this is not true for all our events as can be seen in the figure. Figure 3.3 is consistent with results that magnetic storms are not directly related to relativistic electron enhancements at geostationary orbit, (*Hajra et al.*, 2015; *Kim et al.*, 2015), as events can occur at any time relative to, and for any value of, SYM-H minimum. While the occurrence of geomagnetic storm was not a criteria for event selection, we note that all REE are associated with some type of geomagnetic disturbance.

Figure 3.4 shows a superposed epoch time analysis of the solar wind and magnetospheric parameters displayed in Figure 3.2 to statistically identify common features that are associated with the relativistic electron enhancement events. Every individual event is shown in light grey to illustrate the spread of each parameter. The upper and lower quartile values are shown in blue and the median values in red. The top panel in Figure 3.4 show the time evolution of the > 2 MeV electron flux, and we can observe the statistical shape of an enhancement, modulated by the MLT dependence (diurnal variation) of the flux. For negative time, the flux oscillates in the range 10^0 to 10^2 cm^{-2} sr^{-1} s^{-1}. At time $t = 0$ the enhancement in flux starts, and in the first 12 hours each quartile value rapidly increases by 2 orders of magnitude. Within 36 hours after the enhancement initiation, the ratio of the flux levels to pre-flux values is larger than 3 orders of magnitude. Around this time, we consider the enhancement to have stopped, despite some minor

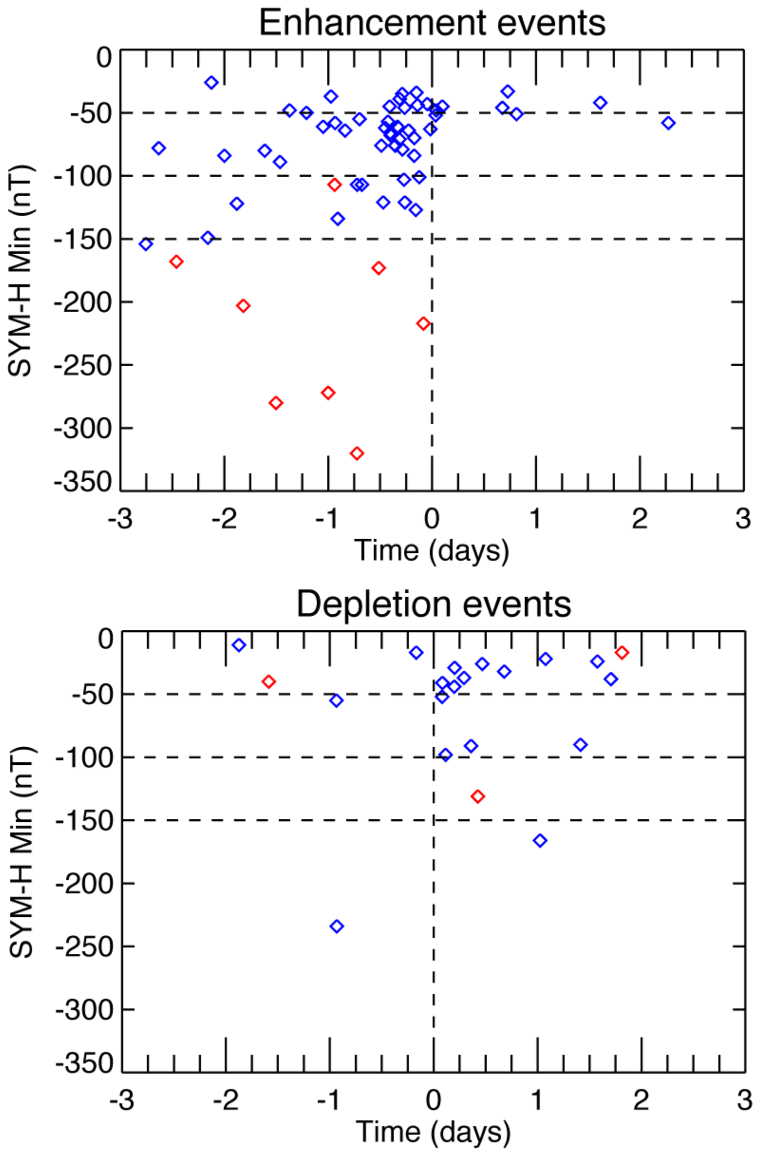

Figure 3.3: Minimum SYM-H value for enhancement events (top) and dropouts (bottom) and their time of occurrence with respect to start time $t = 0$. Red marks indicate CME events and blue marks indicate CIR events. Horizontal dashed lines indicate traditional definitions of weak (-50 nT), moderate (-100 nT) and strong (-150 nT) geomagnetic storms.

growth in flux during the following days for some events. When analyzed separately, events associated with a different solar wind driver, CIR or CME disturbances, exhibit very similar behaviors, suggesting that the overall, average enhancement characteristic does not depend on the type of driver as can be seen in Figure 3.5 that shows a superposed epoch analysis over the events separated by solar wind driver, (CME and CIR). The solar wind speed V_x component shows a continuous increase that reaches a maximum soon after the enhancement starts and then a plateau, with the speed not decreasing for most of the duration of events. The lower quartile has a speed > 500 km/s for the whole duration of the enhancement events.

Solar wind proton density n_{sw} and solar wind dynamic pressure p_{dyn} both show a drop right before the enhancement starts. A further relevant feature is that for the duration of the enhancement period, both solar wind proton density and dynamic pressure values remain low, and recover only when electron fluxes start to decrease. Interplanetary magnetic field B_z magnitude for pre-enhancement is larger than post-enhancement and presents strong ULF oscillations due to the compression in the solar wind stream interface (as the majority of events are associated with CIRs). The oscillations and the magnitude of B_z are much weaker during the flux enhancement period. Bz median value is slightly southward directed with $0 > B_z > -1$ nT during that same period.

For derived indices, AE index peaks around the time enhancements start at around 400 nT and remains elevated for most of the pre and post-enhancement time period. ULF power peaks around half a day before the enhancement starts and steadily decreases afterwards. The peak ULF power median value is double the average ($\sim$ 0.79 nT^2) and median ($\sim$0.82 nT^2) ULF power that characterizes the 11 year period of this study, and the power decreases until it reaches average values a few days following the enhancement Finally, the reconnection electric field calculated from the definition given by *Kan and Lee* (1979) increases and peaks in a similar way to ULF power. Considering that reconnection electric field is an indicator of magnetospheric convection it makes sense to expect an increase in electric field before the enhancement in flux begins (*Meredith*, 2002; *Lyons et al.*, 2005; *Hwang et al.*, 2007; *Lyons et al.*, 2009; *Kissinger et al.*, 2014).

Figure 3.6 shows the relativistic electron persistent depletion events following the same format as Figure 3.4. Epoch $t = 0$ is the time where the flux has dropped to its minimum (or below instrument background). Maybe the most important feature in Figure 3.6 is that for almost 4 days no recovery exists, the shortest individual event

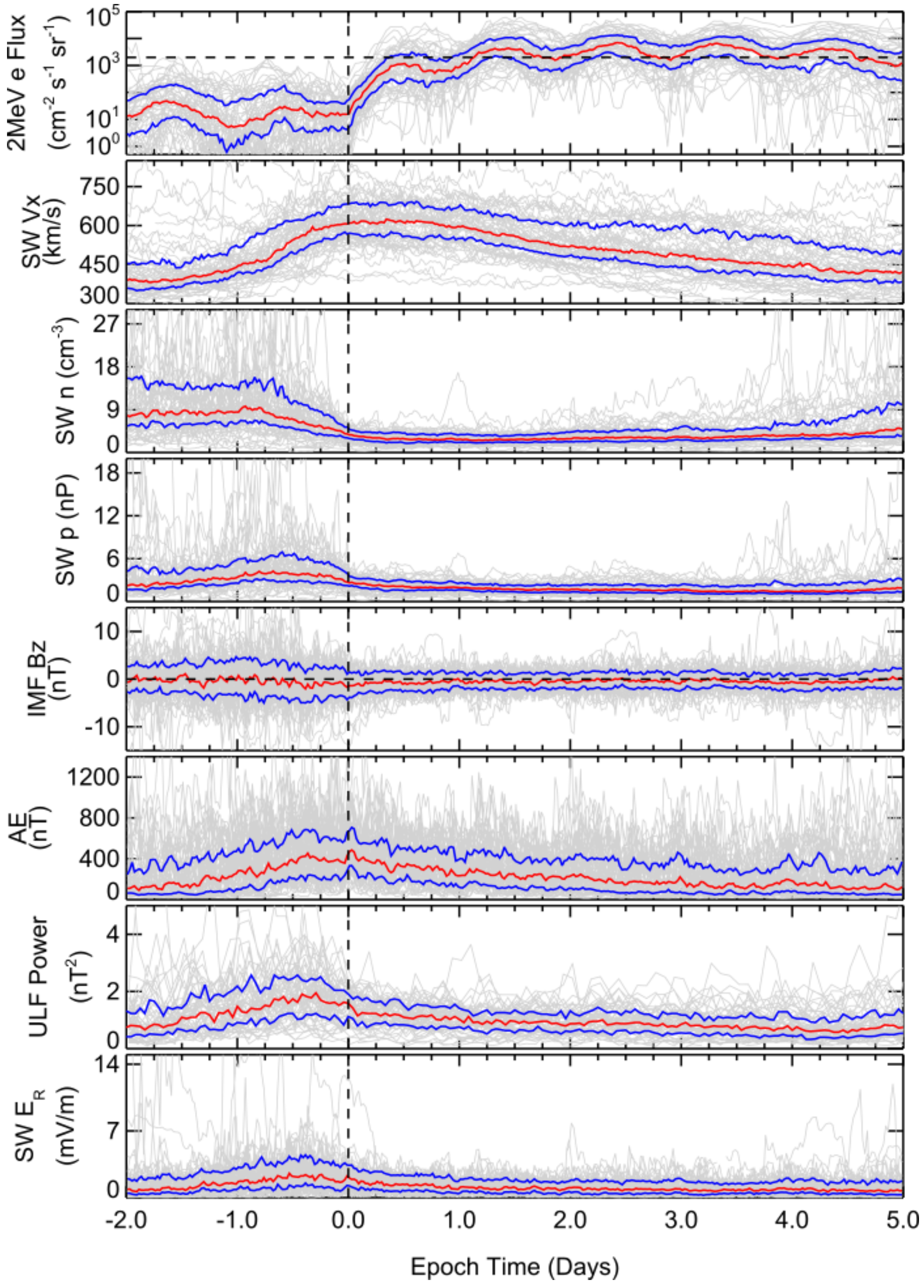

Figure 3.4: Epoch time superposition of 61 relativistic electron enhancement events. Median value of events is shown in red and upper and lower quartile values are shown in blue. Light gray background corresponds to every single superposed event. From top to bottom, panels show: $>$ 2 MeV electron flux from GOES, solar wind speed V_x, solar wind proton density, solar wind dynamic pressure, interplanetary magnetic field (IMF) B_z, AE Index, IMF ULF power and solar wind reconnection electric field.

lasting 3.7 days. Solar wind speed V_x has a median value $V_x < 400$ km/s and very few cases show speeds closer to $V_x \sim 450$ km/s. There are only 3 persistent depletion events associated with CME, and those have a higher speed $V_x \sim 500$ km/s which

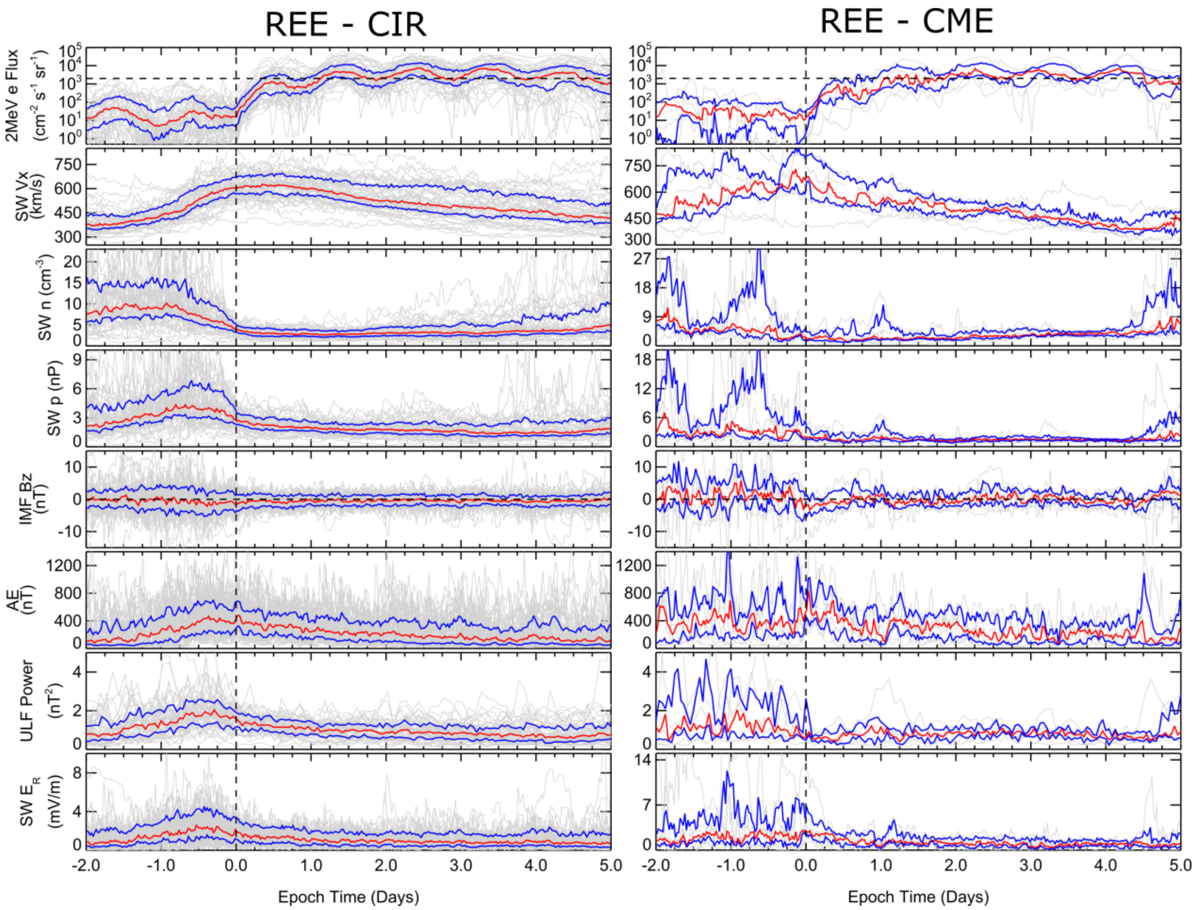

Figure 3.5: Epoch time superposition of 53 CIR associated relativistic electron enhancement events (left) and 8 CME associated events (right). Median value of events is shown in red and upper and lower quartile values are shown in blue. Light gray background corresponds to every single superposed event. From top to bottom, panels show: >2 MeV electron flux from GOES, solar wind speed Vx, solar wind proton density, solar wind dynamic pressure, interplanetary magnetic field (IMF) Bz, AE Index, IMF ULF power and solar wind reconnection electric field

suggest that for persistent depletion events, the solar wind speed might have a different impact depending on whether the event is associated with CME or CIR. Large peaks in solar wind proton density n_{sw} and solar wind dynamic pressure are observed around the time the drop in flux occurs, a result that agrees with a possible depletion through magnetopause shadowing (*Shprits et al.*, 2006; *Kim et al.*, 2010; *Turner et al.*, 2012; *Hietala et al.*, 2014). There is a drop in both dynamic pressure and proton density in the following days, but the values are still very large compared to those seen in enhancement events, suggesting that a low versus high value in dynamic pressure and/or proton density is important for the differentiation of the two types of events. IMF B_z median value is

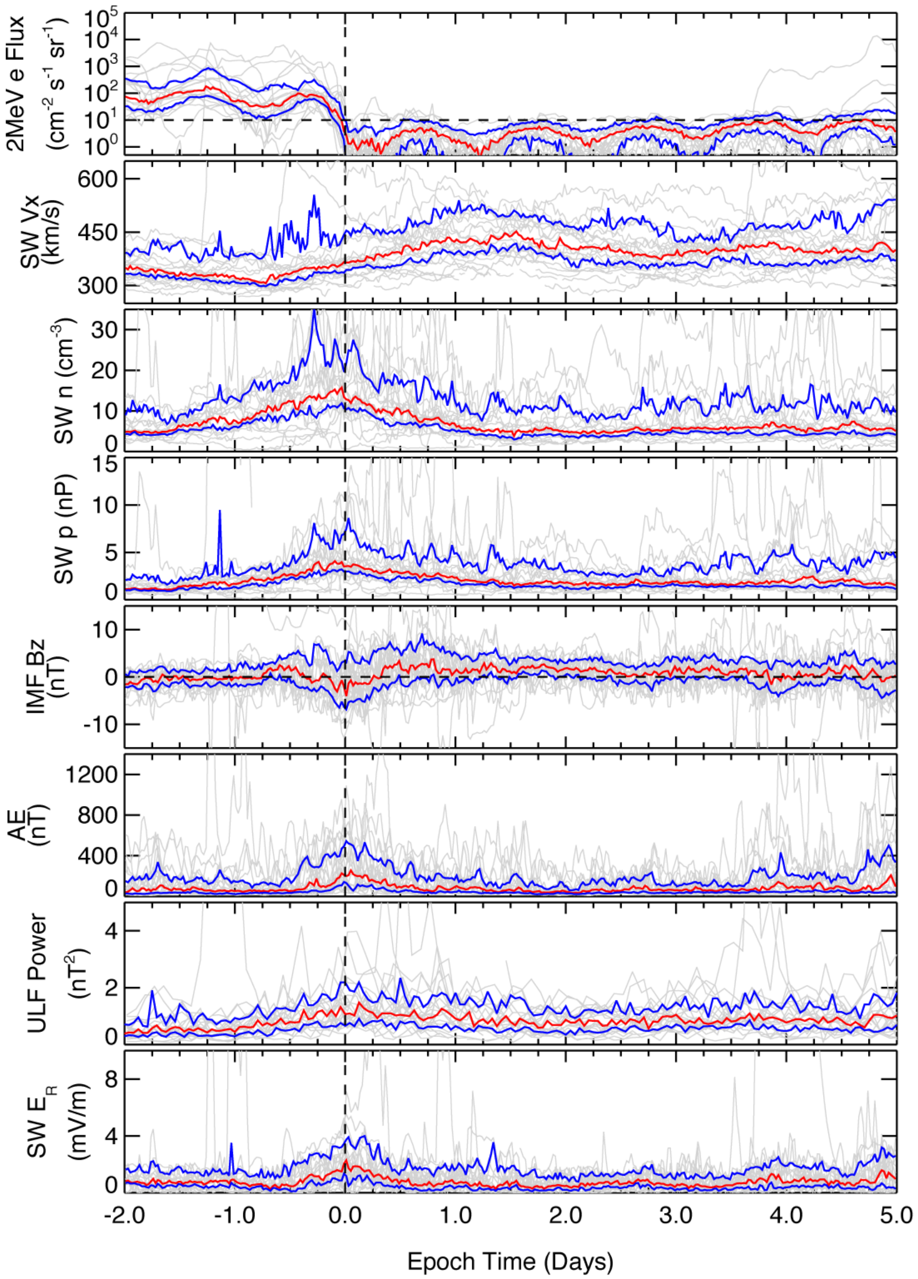

Figure 3.6: Epoch time superposition of 21 relativistic electron depletion events. Median value of events is shown in red and upper and lower quartile values are drawn in blue. Light gray background corresponds to every single superposed event. From top to bottom, panels show: >2 MeV electron flux from GOES, solar wind speed V_x, solar wind proton density, solar wind dynamic pressure, interplanetary magnetic field (IMF) B_z, AE Index, IMF ULF power and solar wind reconnection electric field

negative (southward directed) around the time flux drops and is followed by a northward B_z turning just after time $t = 0$. This northward oriented B_z median lasts for several days, and only around the fourth day after the persistent depletion event started the median value return to a near zero value. If a sudden increase in proton density and dynamic pressure might explain in part the initial drop, the combination of low solar wind speed and northward directed B_z might explain why the flux does not recover. AE index is significantly low except for a small increase around the time the drop occurs, providing another possible explanation for lack of electron flux recovery due to the lack of seed population injection to the radiation belts (e.g., *Jaynes et al.*, 2015). IMF ULF power remains relatively near its average value (~ 0.79 nT^2), the main difference with respect to enhancement events being the lack of a pre $t = 0$ increase. The reconnection electric field also is low during the time of the drop, having a small increase just at the drop time and then several days later.

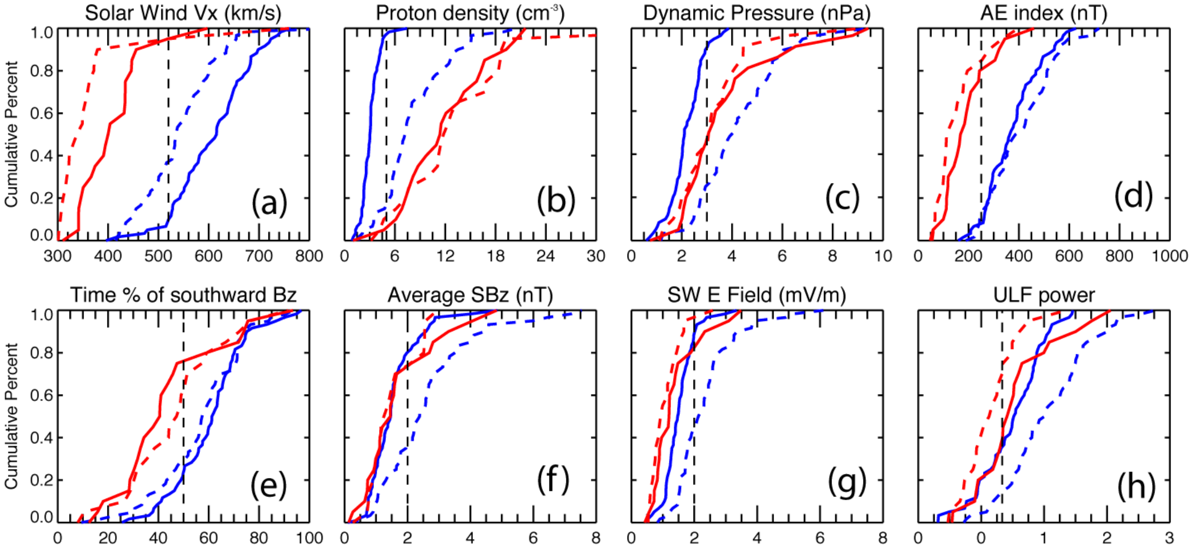

Figure 3.7: Cumulative distribution functions associated with REEs (blue) and persistent depletion events (red). Dashed lines correspond to the average of the 24-hour period before the beginning of the event at $t = 0$, and solid lines correspond to the average of the 24-hour period after $t = 0$. The 8 different panels correspond to (a) solar wind speed V_x, (b) solar wind proton density, (c) solar wind dynamic pressure, (d) AE index (e) time percent of southward directed IMF B_z, (f) average southward IMF B_z, (g) solar wind reconnection electric field and (h) IMF ULF power.

To further characterize the relationship between the solar wind (together with magnetospheric parameters), and relativistic electron enhancement and persistent depletion events, in Figure 3.7 we have calculated cumulative distributions for the parameters presented in Figure 3.4 and Figure 3.6. Figure 3.7 shows relativistic electron enhancement events (blue) and relativistic electron persistent depletion events (red) cumulative distribution of the average value for the day before the start time (dashed line) and for the day after the events started (solid line). Panel (a) shows solar wind speed, and we have drawn a dotted black line at $V_x = 520$ km/s that corresponds to the point of maximum separation between enhancement events and persistent depletion events. After time $t = 0$, 90% of events have a velocity above (enhancement) or below (persistent depletion) this chosen speed value. Both enhancement and persistent depletion events occur with an increase in solar wind speed, but the difference in values exceeding 100 km/s is a clear indication and further confirmation that a high solar wind speed characterizes all relativistic electron enhancement events and is likely necessary for relativistic electron enhancement events to occur. Solar wind proton density (panel b) presents a clear decrease in value between the pre and the post-enhancement time for enhancement events but not for persistent depletion events. We have drawn a dashed line at $n_{\text{sw}} = 4$ cm^{-3} for solar wind proton density as that value separates more than 90% of the enhancement events between a pre and post time $t = 0$. In the case of the persistent depletion events, we notice that most events are associated with large solar wind proton density values. For solar wind dynamic pressure, shown in panel (c), we can also find a similar separation value for pre and post time $t = 0$ in relativistic electron enhancement events. Choosing $p_{\text{dyn}} = 3$ nPa separates around 80% of the enhancement events indicating that a drop in p_{dyn} is a very common feature for REE. Looking at persistent depletion events, we notice that the cumulative distribution falls right in between the distributions for pre and post time $t = 0$ of relativistic electron enhancement events, and presents little change. That the cutoff value is not as clear for solar wind dynamic pressure when compared with solar wind proton density suggests that solar wind proton density is a better parameter to characterize the events than solar wind dynamic pressure and possibly has better predictive potential. The AE index (panel d) shows little variation around $t = 0$ for enhancement events, which in combination with Figure 3.4 indicates a very steady disturbance during pre-and post-enhancement, with 90% of events having AE > 250 nT. High AE index has been proposed a necessary condition for REE to occur (*Hajra* *et al.*, 2015; *Jaynes et al.*, 2015; *Kim et al.*, 2015), as it reflects energy transfer from the solar wind to the magnetosphere and can be associated with injection of seed populations to geostationary orbit. Similarly, persistent depletion events also show very little variation around $t = 0$, but around 80% of these events have AE $<$ 250 nT.

To characterize IMF B_z we have estimated the percent of the time IMF B_z is pointing southward in GSM coordinates and the hourly average value of the southward component. Panel (e) shows the percent of time that IMF B_z is pointing southward and the black dashed line is set at 50%, This roughly separates 80% of the enhancement events (more than 50% of the time pointing southward) and persistent depletion events (less than 50% of the time pointing southward) for both pre and post $t = 0$. This indicates the dominance of a southward oriented B_z during enhancement events. To determine the characteristic values associated with the predominantly southward IMF, the absolute value of the hourly averaged southward directed Bz is shown in panel (f). Dashed line has been selected at $B_z = 2$ nT. Around 80% of the events are below that number after the enhancement starts. In this case, the most intense southward IMF occurs before the enhancement time $t = 0$ and it seems to decrease afterwards. The post-enhancement southward IMF B_z values are similar to the persistent depletion southward IMF B_z values. Both panels (e) and (f) suggest that continuous occurrence of south-oriented IMF B_z, which is not necessarily large in value, is important in driving strong electron enhancement. Panel (g) shows the reconnection electric field and the cumulative plot is very similar to IMF B_z, that is for REE it decreases after $t = 0$ and reaches levels similar to those seen in persistent depletion events. ULF power also shows a decrease indicating that the fluctuations in the IMF are less intense during the period that follows the start of the enhancement. The bottom panels in Figure 3.7 seem to indicate that IMF B_z magnitude and oscillations may be important in the process that leads to enhancement, but of no significant importance in the process that leads to the persistent depletion.

3.4 Summary and Discussion

We have epoch analyzed a set of relativistic electron enhancement and persistent depletion events that occurred between the years 1996 and 2006, identified using > 2 MeV electron flux observations at geostationary orbit from GOES-8 and GOES-10 spacecraft. Our results are consistent with previous results (e.g. *Paulikas and Blake*, 1979; *Reeves et al.*, 2011), in that a large average solar wind speed ($V_x > 500$ km/s) is characteristic of enhancement events. We have also found that persistent depletion events are characterized by lower solar wind speeds ($V_x < 450$ km/s) that are still associated with some type of geomagnetic disturbance (CIR or CME). When comparing REE to REPDE, we find that a threshold velocity separates relativistic electron events from persistent depletion event. Our current estimated threshold value is $V_x = 520$ km/s for which more than 90% of events are situated above (enhancement) or below (persistent depletion). A similar result is obtained for solar wind proton density, where we identify a separation value between relativistic enhancement events and persistent depletion events. A low solar wind proton density seems to be needed for the enhancements to occur (no enhancement event occurs for $n_{\mathrm{sw}} > 4$ cm^{-3}), A value of $n_{\mathrm{sw}} = 4$ cm^{-3} around $t = 0$ is sufficient to differentiate an enhancement event from a persistent depletion event in most cases. Our results do not suggest that a low solar wind proton density is a sufficient condition to ensure that an enhancement event will occur, but strongly suggest that it is a necessary condition for one to occur. Solar wind dynamic pressure closely follows the proton density. We can also find a pressure value for characterize relativistic electron enhancement occurrence, that value being $p_{\mathrm{dyn}} = 3$ nPa. However, solar wind dynamic pressure is also tied to solar wind speed, so a low solar wind speed can also result in a low solar wind dynamic pressure, which is not favorable for REE occurrence, and therefore low p_{dyn} is not as reliable a predictor of relativistic electron enhancement events as solar wind proton density. IMF B_z is predominantly southward oriented for enhancement events and northward oriented for persistent depletion events. The strength of the magnetic field varies considerably from enhancement to persistent depletion events before time $t = 0$

but is similar after $t = 0$, therefore making a large southward oriented IMF B_z average a good indicator of a possible relativistic electron enhancement event. Reconnection electric field and AE values increase as the IMF B_z becomes more southward oriented, and peak around or right before $t = 0$. Increase in IMF fluctuations as shown in the ULF power index are characteristic of the period of pre-enhancement, and remain above their average value during the period of flux enhancement.

In general, our results agree really well with the results of previous works that have focused only on events associated with storms and with those that study long-term variations of the electrons at geostationary orbit. We have gone one step further and established a set of thresholds for some solar wind parameters that we expect will be of use to predict relativistic electron enhancement events. We note that these parameters are not the only possible predictors. AE-Index and reconnection electric fields could be used, but these relate strongly to IMF Bz and solar wind speed and thus would not add new information. SYM-H is not a reliable predictor as a decrease in SYM-H is not needed for a relativistic electron event to occur. Instead, a disturbance associated with a corotating interaction region might result in an enhancement just as during a storm recovery phase independent of whether the event led to a significant SYM-H drop (see also *Miyoshi and Kataoka*, 2008).

For a simple test of predictive power of our results we have set up a simple set of conditions, using a "threshold" mechanism. According to our results, we expect an enhancement event to occur when $V_x > 520$ km/s, $n_{\mathrm{sw}} < 4$ cm^{-3} and southward average $B_z < -2$ nT. Going through the period of our study, 1 Jan. 1996 to 31 Dec. 2006 we find that 90% (55 of 61 events) fulfill the three conditions while in the other 6 at least two are met. We have extended this testing to the out of study period of from 1 Jan. 2007 to 31 Dec. 2010 during which our identification criteria gives 18 relativistic electron enhancement events. The set of threshold conditions is able to predict 16 of those 18 events, while the two missing still fulfill at least two of the three conditions. Figure 3.8 show the predictability during the year 2010 using different combinations of "thresh-

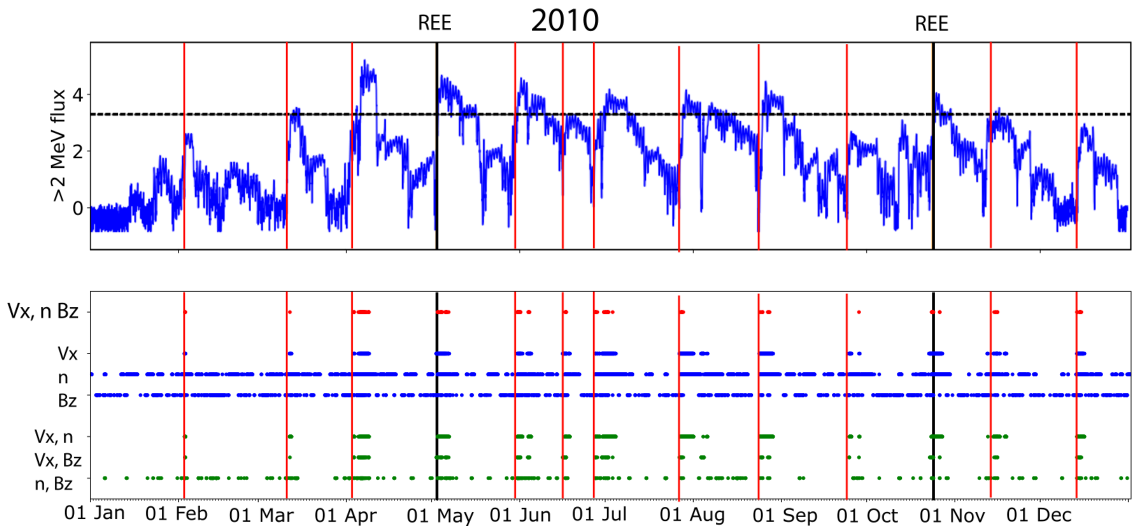

Figure 3.8: Yearly > 2 MeV flux from GOES for year 2010 (top) and different thresholds: solar wind speed $V_x > 520$ km/s, solar wind proton density $n_{\text{sw}} < 4$ cm^{-3} and IMF B_z southward component average $\langle Bz \rangle < -2$ nT. Color indicate when 3 thresholds are met (red), two different are met in different combinations (green) or one is met (blue). Black vertical lines correspond to REE and red vertical lines correspond to a period in which the three thresholds are met and an enhancement (not considered REE) occurs.

olds" as identified in the lower panel. Interestingly, in 2010 we have only two relativistic electron enhancement events based on the criteria we used to select them, yet there are plenty of increases in flux that we have not catalogued as "events" but the threshold criteria accounts for all of them. We are showing 2010 as it is a particularly inactive year, together with 2009, as they are close to solar minimum. This may present some extra challenges when it comes to prediction (*Rodger et al.*, 2016), however, visualization is easier. The identification of relativistic electron enhancement events and increases in flux not labeled as "events" still works for the years not shown on the plot. Therefore, although this is a rather simple attempt, it strongly indicates that a combination of the high solar wind speed, low solar wind proton density and southward IMF are important in the electron acceleration process regardless of the detailed physical mechanisms for acceleration.

We have also studied IMF ULF as a possible contributor to relativistic electron enhancement events, specifically when IMF B_z is not strong enough to result in enhancement as was proposed by *Kim et al.* (2006). While the cumulative distribution analysis

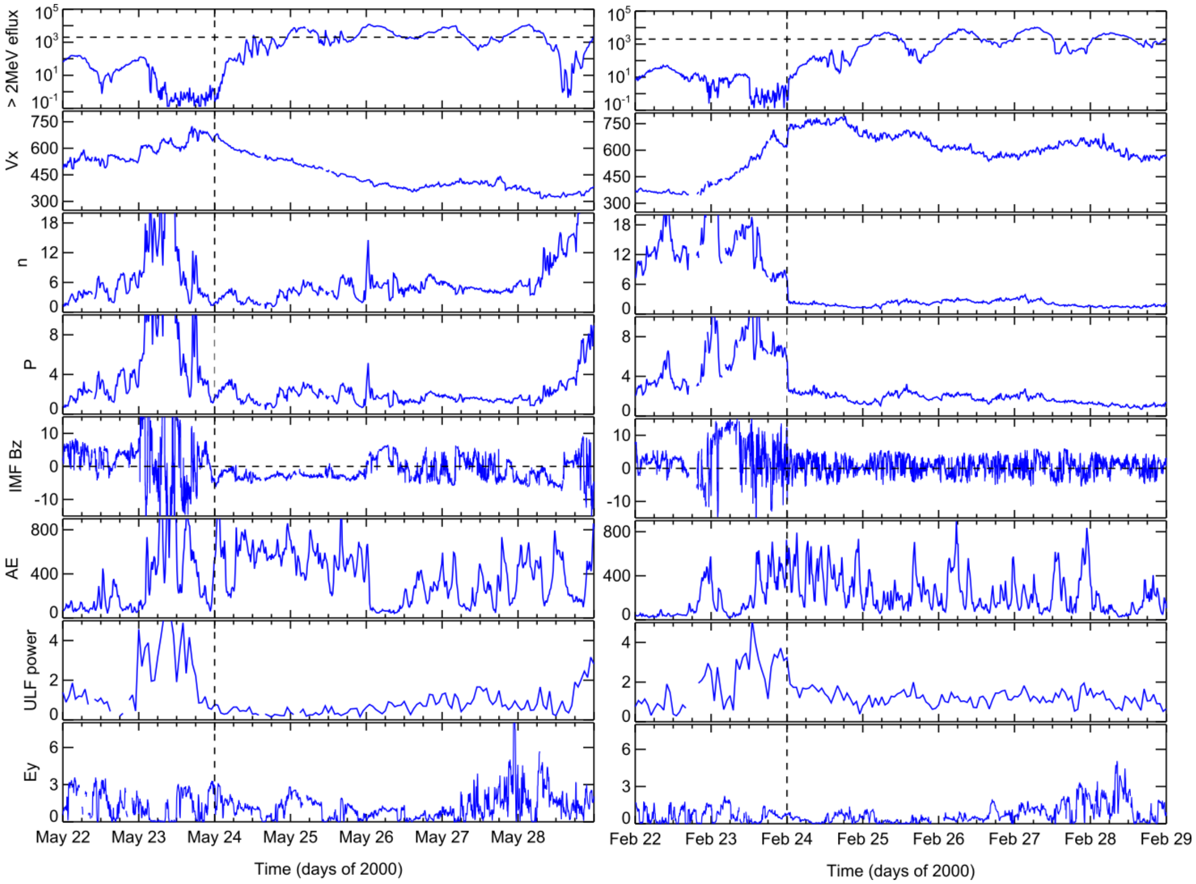

Figure 3.9: Example of a relativistic electron enhancement events occurred on 24 May 2000 with a very steady IMF B_z component during the enhancement period (left) and 24 Feb 2000 that presents a minor IMF B_z component but intensely fluctuating, as captured by ULF index (right). From top to bottom, panels show: > 2 MeV electron flux from GOES, solar wind speed V_x, solar wind proton density, solar wind dynamic pressure, interplanetary magnetic field (IMF) B_z, AE Index, solar wind ULF power and solar wind reconnection electric field. Vertical dashed line indicates the time $t = 0$; enhancement start or depletion of flux.

did not show clear statistically relevant signature in IMF ULF power other than an increase just before $t = 0$, we think that in a case by case study, IMF ULF power can provide some extra information to improve predictive capabilities. Figure 3.9 compares a relativistic electron enhancement event with steady, relatively large southward IMF B_z (left) and an event with north-south fluctuating IMF with average B_z close to 0 (right). Despite the large difference in average southward B_z, the electron intensities reach comparable peaks. This observation suggests that north-south ULF fluctuations might be as effective as steady, relatively large southward IMF in transferring solar wind energy that can drive continuous AE activity which in turn drive electron enhancement at GEO by supplying seed electrons and contributing to the growth of waves that can accelerate the seed electrons via wave-particle interactions. This is a topic that we believe warrants further elaborated study. Statistical verification of an IMF ULF power effect requires separation of its effect from the effects of other solar wind parameters, especially solar wind speed, because large IMF fluctuations usually prevail in high-speed streams and IMF ULF power effect can only be secondary to the dominant solar wind speed effect.

Table 3.1: List of the 61 relativistic electron enhancement events events used in the present study. Time corresponds to the first time of positive gradient. Driver corresponds to the type of solar wind geomagnetic driver.

Date	Time (t=0)	Driver	Date	Time (t=0)	Driver
1996-01-14	22:00	CIR	2002-08-11	15:00	CIR
1996-02-11	21:00	CIR	2002-09-10	12:00	CME
1996-03-12	06:00	CIR	2002-10-04	08:00	CIR
1996-09-12	09:00	CIR	2002-11-21	15:00	CIR
1997-02-28	10:00	CIR	2003-01-20	10:00	CIR
1997-11-23	10:00	CIR	2003-06-02	12:00	CIR
1998-03-11	09:00	CIR	2003-10-15	06:30	CIR
1998-05-05	06:18	CME	2003-11-11	12:00	CIR
1998-07-17	06:00	CIR	2004-02-12	11:30	CIR
1998-07-23	15:00	CIR	2004-02-29	11:00	CIR
1998-09-25	09:53	CME	2004-04-06	05:30	CIR
1998-10-21	03:00	CIR	2004-05-06	12:00	CIR
1999-04-30	04:00	CIR	2004-06-29	14:30	CIR
1999-08-17	07:00	CIR	2004-10-14	05:00	CIR
1999-09-13	09:00	CIR	2004-12-17	11:00	CIR
1999-11-08	21:00	CIR	2005-01-12	15:00	CIR
1999-12-04	12:00	CIR	2005-02-08	08:00	CIR
2000-01-28	12:00	CIR	2005-03-07	11:00	CIR
2000-02-24	14:30	CIR	2005-03-26	07:00	CIR
2000-04-07	18:30	CME	2005-05-01	02:00	CIR
2000-05-24	17:08	CME	2005-11-03	12:00	CIR
2000-08-29	08:00	CIR	2006-01-26	13:00	CIR
2000-09-19	21:00	CME	2006-02-20	14:00	CIR
2000-11-11	12:00	CME	2006-03-19	12:00	CIR
2001-04-13	13:00	CME	2006-04-10	00:00	CIR
2001-06-10	06:00	CIR	2006-06-07	12:00	CIR
2001-06-20	09:00	CIR	2006-07-05	06:00	CIR
2001-07-17	12:00	CIR	2006-08-07	16:00	CIR
2002-01-11	15:00	CIR	2006-09-18	11:00	CIR
2002-02-07	12:00	CIR	2006-10-14	06:00	CIR
2002-07-20	06:00	CIR			

Table 3.2: List of the 21 relativistic electron persistent depletion events used in the present study. Time corresponds to the minimum flux after dropout. Driver corresponds to the type of solar wind geomagnetic driver.

Date	Time (t=0)	Driver
1996-11-24	19:00	CIR
1997-04-10	21:00	CIR
1998-01-16	22:00	CIR
1998-04-04	02:00	CIR
1999-06-16	04:00	CIR
1999-09-22	00:00	CME
1999-12-13	07:14	CIR
1999-12-24	01:31	CIR
2000-08-23	12:00	CIR
2001-01-04	05:00	CIR
2001-02-06	04:30	CIR
2001-08-17	12:00	CME
2001-11-25	12:00	CME
2001-12-12	06:00	CIR
2002-02-01	00:00	CIR
2002-02-19	00:00	CIR
2002-07-01	03:00	CIR
2004-11-04	03:00	CIR
2006-02-11	03:00	CIR
2006-03-07	00:00	CIR
2006-05-31	02:00	CIR

CHAPTER 4

Radial Response of Outer Radiation Belt Relativistic Electrons During Enhancement Events at Geostationary Orbit

The material in this chapter has been submited for publication to the *Journal of Geophysical Research: Space Physics*. The text is presented with some minor modifications to the submitted manuscript to include the supplementary information of the original published work.

4.1 Introduction

The Earth's outer radiation belt, located approximately in the region between $3 < R_E < 7$ consists mostly of trapped electrons with energies ranging from few tens of keV up to tens of MeV. These electron populations are very dynamic and fluxes are known to vary by several orders of magnitude in periods of time ranging from hours to days (e.g. *Li et al.*, 1999; *Millan and Thorne*, 2007; *Thorne*, 2010; *Thorne et al.*, 2013a; *Jaynes et al.*, 2015). Such extreme responses are known to be associated with changes in the solar wind (*Paulikas and Blake*, 1979; *Reeves et al.*, 2011), the phase of the solar cycle (*Baker et al.*, 1986) and increased levels of geomagnetic activity (*Reeves*, 1998). Geomagnetic storms have been the centerpiece of the investigation of enhancements of relativistic electrons as they are known to provide the necessary energy input into the system to set the inner magnetosphere in motion. Yet, *Reeves et al.* (2003) found that only around 50% of geomagnetic storms result in enhancement of fluxes at geostationary orbit since loss processes are enhanced together with acceleration processes during storm periods. It has been shown that geomagnetic storms, defined by a significant drop in the D_{st} index (*Gonzalez et al.*, 1994), are not required to produce enhancement events (*Anderson et al.*, 2015; *Schiller et al.*, 2014; *Kim et al.*, 2015; *Pinto et al.*, 2018a; *Su et al.*, 2014) since energy transfer mechanisms that are not efficient at driving enhancements in the ring current, and hence the D_{st} index, can still provide the required energy for enhancement of electron fluxes (*Borovsky and Denton*, 2010; *Denton and Borovsky*, 2012).

In the past, the bulk of studies focused on enhancement of relativistic electrons at geostationary Earth orbit (GEO). Located at $R_E \sim 6.6$, the geostationary orbit is a key location for communication and meteorological satellites, and therefore has provided scientific measurements of the outer radiation belt for several decades. Due to its location in the outer part of the radiation belt, dramatic changes can occur in electron fluxes. Since relativistic (~MeV) electrons that get enhanced can cause malfunctions in satellite equipment (*Baker*, 2000; *Wrenn et al.*, 2002; *Wrenn*, 2009), many efforts have been made to understand what causes enhancements at GEO (*O'Brien et al.*, 2001; *Hajra et al.*, 2015; *Kim et al.*, 2006, 2015; *Balikhin et al.*, 2011; *Lyatsky and Khazanov*, 2008; *Iles et al.*, 2002) as well as to accurately forecast their behavior (*Baker et al.*, 1990; *Li et al.*, 2001; *Turner and Li*, 2008; *Simms et al.*, 2014, 2016; *Boynton et al.*, 2015).

The launch of the Van Allen Probes mission in 2012 provided a unique opportunity to expand studies of relativistic electron enhancements to the whole extent of the outer radiation belt (*Mauk et al.*, 2013). The response of the outer radiation belt to geomagnetic storms has been studied in detail for relativistic (e.g. *Turner et al.*, 2015) and ultrarelativistic (i.e. $\gamma > 10$) energies (e.g. *Moya et al.*, 2017; *Xiong et al.*, 2015, 2018; *Zhao et al.*, 2019; *Katsavrias et al.*, 2019; *Tang et al.*, 2017; *Murphy et al.*, 2018), and their dependence on the solar wind driver of the storms (e.g. *Pandya et al.*, 2019; *Bingham et al.*, 2018; *Yuan and Zong*, 2019; *Li et al.*, 2015b; *Shen et al.*, 2017). Recently, *Turner et al.* (2019) presented an extended overview of the state of the response of the electron radiation belt to geomagnetic storms summarizing most of the findings during the Van Allen Probes era and showing that storm-time response of the radiation belt is qualitatively predictable.

Although several models of different kinds have been developed to forecast the state of the outer radiation belt based on the real-time measurements of the Van Allen Probes, the end of the mission requires the development of forecast methods that rely on proxy measurements. Although several attempts have been made with low-orbiting satellites, in this study we take a different approach and explore the use of geostationary data from the GOES satellites as a possible proxy for the state of the outer radiation belt. Recently, *Baker et al.* (2019) has calculated the correlation between daily averaged fluxes in geostationary orbit and the Van Allen Probes mission, establishing a baseline statistics for how often we should expect to be able to use the GEO boundary as a predictor for fluxes at lower L-shells. Additionally, *Moya et al.* (2017) showed that when geomagnetic storms result in enhancement of fluxes, there is a relatively coherence response of the belt for $L > 4.5$. In this Chapter we focus on the relativistic electron enhancement events at GEO and determine under which circumstances the correlation to fluxes at lower $L-$shells, and therefore the potential for forecast across the whole outer belt, can be improved. This Chapter is presented as follows. Section 4.2 describes the data utilized and the event selection criteria. In section 4.3 we compare the response of the fluxes from GOES and Van Allen Probes for 60 events that occurred between 1 October 2012 and 31 December 2017. Section 4.4 we study the correlation between fluxes at GEO and those at different $L-$shells. In section 4.5 we study magnetospheric parameters associated with those events to estimate to what extent we can use GEO data from GOES satellites to estimate the fluxes of relativistic electrons across the outer radiation belts and what are the current limitations. Finally, in section 4.6 we summarize and discuss the findings of this study.

4.2 Data and Events

Relativistic electron enhancement (REE) events at GEO are defined as prolonged periods of time over which electron fluxes recover from a dropout and exceed a minimum threshold, for example, NOAA issues warnings when $f_{\text{GEO}} > 10^3$ cm^{-2} sr^{-1} s^{-1}. Here we follow the definition used in *Pinto et al.* (2018a) and *Kim et al.* (2006) that defines an enhancement event as an increase in electron fluxes from less than 10^2 cm^{-2} sr^{-1} s^{-1} to more than 2×10^3 cm^{-2} sr^{-1} s^{-1} in less than 2 days, and maintains an average daily flux larger than 10^3 cm^{-2} sr^{-1} s^{-1} for at least 3 days. The increase by at least an order of magnitude in fluxes, as well as the relatively long 3-day interval of elevated fluxes attempts to avoid confusion between real increases in flux, and purely adiabatic effects which are reversible and recover when D_{st} recovers (*Kim and Chan*, 1997). To identify REE events we used > 2 MeV electron fluxes obtained from the Geostationary Operational Environmental Satellite (GOES) 15 Energetic Proton, Electron and Alpha Detector (EPEAD) instrument (*Rodriguez et al.*, 2014), sampled at 5 minute temporal resolution. From 1 September 2012 to 31 December 2017 we found 60 REE events at GEO. For each event, we have determined a time $t = 0$ as the first time at which a positive gradient in the fluxes is detected after a dropout has occurred, given that the gradient continues to be positive until the enhancement flux threshold has been met. This selection of a time $t = 0$ is different from the more traditionally used time of minimum D_{st} (or SYM-H) (e.g. *O'Brien et al.*, 2001) and reflects the assumption that we do not consider geomagnetic storms to be a strict requirement in the search of REE events, but the two phenomena are both results of the same driving conditions. Indeed, a geomagnetic storm defined by a minimum $D_{\mathrm{st}} < -50$ nT (*Gonzalez et al.*, 1994) has long been shown to be not strictly required for the occurrence of REE events at GEO (*Kim et al.*, 2015; *Pinto et al.*, 2018a; *Hajra et al.*, 2015; *Anderson et al.*, 2015; *Su et al.*, 2014; *Schiller et al.*, 2014). This is explained in part by the fact that a significant number of events are associated with a high-speed stream driven Corrotational Interaction Region (CIR), which has been shown to be effective at driving REE's but can be less effective at causing D_{st} drops (*Borovsky and Denton*, 2006, 2010). A detailed list of the dates of each event with their respective solar wind driver and $SYM - H$ minimum values can be found in Table 4.2.

To study the response of the outer electron radiation belt as a function of $L-$shell during REEs at GEO, we used data from the Van Allen Probes (*Mauk et al.*, 2013) Energetic Particle, Composition and Thermal Plasma Suite (*Spence et al.*, 2013) Relativistic

Electron-Proton Telescope (*Baker et al.*, 2013b) (ECT-REPT). As we want to compare between GOES and the Van Allen Probes, we will use the $E = 2.1$ MeV differential energy channel. The data has been processed following a procedure similar to the one described in *Moya et al.* (2017), that is, we have calculated omni-directional fluxes by averaging over all pitch angles, and then we have performed a binning to $\Delta L = 0.1$. We then combined data from RBSP-A and RBSP-B and performed a new binning in both time $\Delta t = 6$ hours and space $\Delta L = 0.1$. This procedure ensures continuous coverage over all $2.5 < L < 6.0$ but reduces the temporal resolution to 4 points a day. To determine enhancements in the outer belt during each event, we follow the more traditional definition of evaluating whether the maximum fluxes in the time interval $12 < t < 96$ hours ($t = 0$ is defined by the GOES events) are at least twice the maximum fluxes during the interval $-72 < t - 12$ hours for every $L-$shell between $2.5 < L < 6.0$ (*Reeves et al.*, 2003; *Turner et al.*, 2015; *Moya et al.*, 2017). To avoid spurious results due to oscillations in low fluxes, we also require that the maximum flux after $t = 0$ for a particular $L-$shell to be larger than the 25 percentile values calculated from the entire Van Allen Probes mission (values can be found in the Table 4.3).

Figure 4.1 shows the temporal evolution of two different REE events that occurred on 08 October 2012 (left) and 13 May 2015 (right). Both events are associated with large geomagnetic storms (SYM-H min ~ -100 nT), continuously elevated AE index values for at least one day after $t = 0$, large > 500 km/s solar wind speed and a somewhat negative interplanetary magnetic field B_z. Differences do exist in maximum V_x and soutward IMF B_z intensity, but despite these differences both events result in very similar maximum flux values as observed at GEO of $\sim 2 \times 10^4$ cm^{-2} sr^{-1} s^{-1} during the recovery phase of the storm and on the following days. These similarities in flux evolution at GEO are still present down to $L = 5.5$ but do not propagate inward across the rest of the outer radiation belts. Panels (b) and (h) show the $E = 2.1$ MeV channel as a function of $L-$shell. The black lines correspond to the contours of 90% and 75% of the maximum log(flux) illustrating the differences in penetration to lower $L-$shells. It can be appreciated from the figure that the event of 08 October 2012 presents

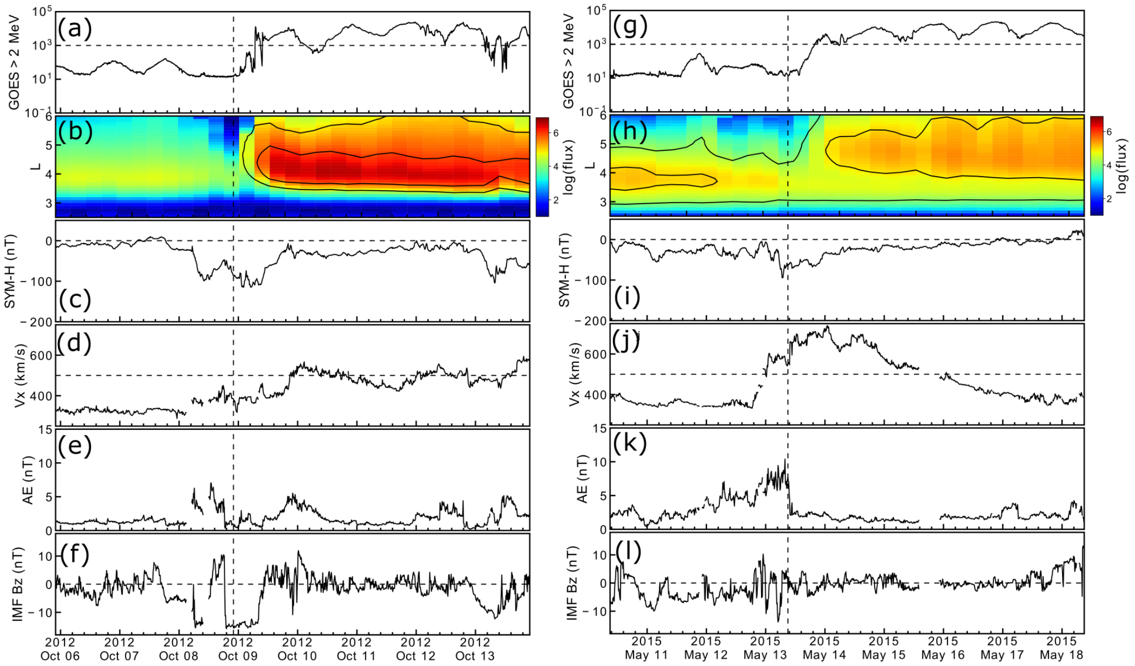

Figure 4.1: Two relativistic electron enhancement (REE) events that occurred on 08 October 2012 (left) and 13 May 2015 (right). From top to bottom: (a,g) $>$ 2 MeV electron flux from GOES 15, (b,h) Van Allen Probes REPT $E = 2.1$ MeV electron flux binned in time and space. Contours correspond to 90% and 75% of log(maximum flux) showing the different regions of maximum enhancement. Lower panels show SYM-H index (c,i), solar wind speed (d,j) , AE index (e, k) and interplanetary magnetic field B_z component (f,l).

significant enhancement down to $L \sim 3.2$ with a peak in flux at $L = 4.0$. The event of 13 May 2015 shows an enhancement down to $L \sim 4.0$ with peaks in fluxes at $L = 4.5$ More importantly, the enhancement profiles are very different, fluxes for the event of 08 October 2012 are up to an order of magnitude larger than in the event of 13 May 2015 in the region $3.5 < L < 5.0$ but are actually lower in the region $L > 3.3$. Still the high magnitude of pre-existing fluxes on the belt results in a depletion (when comparing by L) of fluxes for the 13 May 2015 events for all $L < 3.7$.

The examples in Figure 4.1 show that REE events that look similar at GEO may respond very differently at different L-shells across the outer radiation belt, and especially so at lower $L-$shells. Also, the magnitude of pre-existing fluxes on the belt may play an important role in the interpretation of any statistical analysis that uses ratios of post-to-pre enhancement fluxes and therefore must be considered. In the following sections we characterize the similarities and differences in the response of the belt as a function of

L for the 60 events we have found and quantify how the strength of some geomagnetic indices translates to predictive capabilities of the extent of the enhancements across the outer belt.

4.3 Radial response of relativistic electron enhancement events

To understand the evolution of the outer radiation belt at different $L-$shells we have estimated the ratio of change in electron fluxes for all $2.5 < L < 6.0$. Figure 4.2 shows the comparison of the maximum fluxes measured in the $-72 < t - 12$ hours prior to $t = 0$ and maximum fluxes measured in the $12 < t < 96$ hours after $t = 0$. The different panels show electron fluxes at GEO and at 7 different $L-$shells ranging from $L = 6.0$ and decreasing at intervals of $\Delta L = 0.5$ to $L = 3.0$. Blue (red) dashed lines in each panels correspond to a ratio $r = 2.0$ ($r = 0.5$), traditionally used to determine an enhancement (depletion) event (e.g. *Reeves et al.*, 2003). Individual events have been color-coded following the same definition.

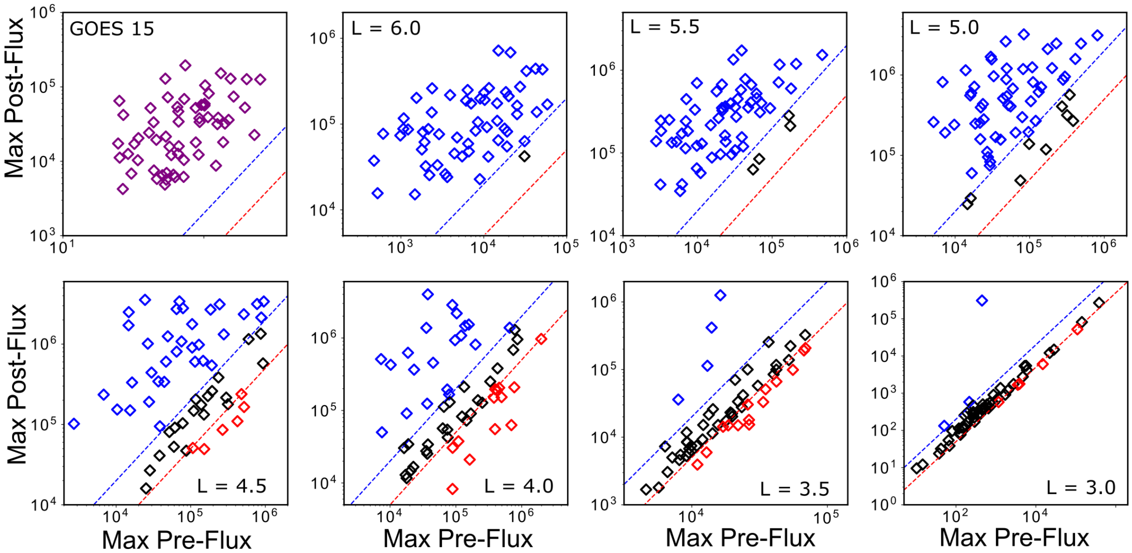

Figure 4.2: Maximum post-to-pre $t = 0$ fluxes at geostationary orbit (GOES 15) and at different $L-$shells from Van Allen Probes data. Dashed blue (red) lines mark the ratio $r = 2.0$ (r=0.5). Individual events have been color coded according to whether their ratio is indicative of an increase $r > 2.0$ (blue), a decrease $r < 0.5$ (red) or in between showing no change (black).

Figure 4.2 shows the drastic decrease in the effectiveness of the enhancement response as $L-$shell decreases. At $L = 6.0$, all but one event (98%) result in enhancements, which decreases to 85% at $L = 5.0$. However, for $L < 5.0$ the decrease in occurrence is significant, with only 36% of events resulting in enhancement of fluxes at $L = 4.0$ and only 5% at $L = 3.0$. Since Figure 4.2 also shows the changes in fluxes, we can notice that the trend is to move towards lower post-to-pre flux ratios as we move to lower $L-$shells. Several events present little to no change ($0.5 \leq r \leq 2.0$) for $L \leq 5.0$ which then becomes the majority of the events at $L = 3.0$. Additionally, a number of events correspond to depletions ($r < 0.5$) between $3.0 < L < 4.5$, with a peak in the decrease in fluxes at $L = 4.0$ where the depletions appear to be most significant suggestive of a possible local loss mechanism (e.g. *Bortnik et al.*, 2006; *Mourenas et al.*, 2016; *Blum and Breneman*, 2019).

Figure 4.3 expands the information of Figure 4.2 to all $L-$shells in the range $2.5 \leq L \leq 6.0$. Figure 4.3(a) shows the occurrence (in percentage) of enhancements, depletions and no-change of fluxes as a function of $L-$shell. Between $6.0 < L < 5.1$ the occurrence of enhancement events is $> 90\%$ as would be expected since they are selected based on REEs at GEO. However, a significant decrease in enhancement occurrence takes place between $3.5 < L < 5.1$, decreasing down to only 8% of events resulting in enhancement of fluxes at $L = 3.1$. The number of unaffected (no change) events increase from 2% at $L = 6.0$ up to 98% at $L = 2.5$, indicating the range of effectiveness of propagating an REE from GEO towards the inner magnetosphere, the exception being the 17 March 2015 storm (minimum $D\text{st} = -223$ nT) that caused an enhancement for all $L \geq 2.5$, consistent with the expected result that only extremely strong geomagnetic activity can affect the innermost part of the outer radiation belt. For $L < 4.7$ there are a number of events that present a depletion compared to pre $t = 0$ fluxes ($r < 0.5$). The peak occurrence of depletions is $\sim 25\%$ of events, which occurs at $3.4 < L < 3.8$, suggestive of a local loss mechanism.

Figure 4.3(b) shows the distribution of post-to-pre flux ratios as a function of $L-$shell for all 60 events. The black dots represent the median of the distribution at each $L-$shell; the green colored bars indicate the upper and lower quartiles of the distribution and black bars the 5th and 95 percentiles. The blue (red) dashed lines represent the enhance-

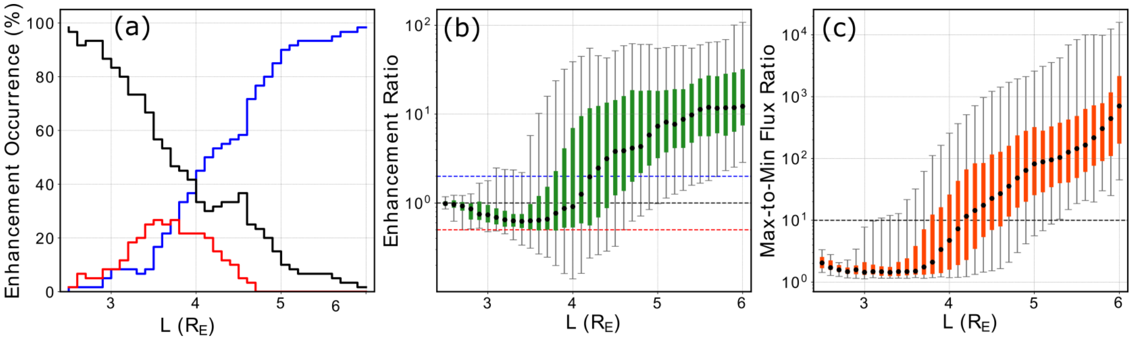

Figure 4.3: (a) Occurrence percentage as a function of L for enhancement (blue), depletion (red) and no-change (black) response of all 60 events. (b) Distribution of post-to-pre flux ratios as a function of $L-$shell. Black dots indicate median values, the colored bar corresponds to upper and lower quartile distributions and black lines indicate the 5th and 95th percentiles of the distribution of events at each $L-$shell. (c) Distribution of maximum to minimum flux ratio as a function of $L-$shell. Colored bars and black lines indicate similar percentiles as in (b).

ment (depletion) thresholds $r = 2.0$ ($r = 0.5$). The medians of the distributions show a decrease in the flux ratio as L decreases that reaches a minimum at around $L = 3.5$ and that slightly increases for $L < 3.5$ to reach a value of almost $r = 1$ at $L = 2.5$, indicating the range of penetration of a REE at GEO. By showing the 5th and 95th percentiles we can get a sense of how much spread there is in the distribution for all $L > 4.0$ with the highest variability between $4.0 \leq L \leq 4.5$. A sharp decrease in the spread for $L < 3.5$ indicates that this region is mostly unaffected by processes that affect the external part of the belt. The depletion zone $r < 0.5$ between $3.5 < L < 4.5$ indicates the region that is likely affected by the depletion processes driven by geomagnetic activity but not so much for the processes producing the enhancement of fluxes, for around 25% of the events and it shows that the peak in depletion occurrence is between $3.5 < L < 4.0$ with the strongest depletion rate at $L = 4.0$.

Figure 4.3(c) shows the distribution of the ratio of increase of the fluxes at different L with respect to the minimum fluxes measured within $-24 < t24$ hours, in the same format as Figure 4.3(b). The black dashed line is located at an increase in fluxes by a factor of 10 with respect to the minimum flux measured at that particular $L-$shell. At higher $L > 5.5$ the increase can be of 3-4 orders of magnitude with respect to the minimum measured flux but this factor also decreases as L decreases. For $L < 3.5$

the majority of the events presents no increase in fluxes with respect to the minimum value, and therefore the categorization of a depletion or a no-change event is mostly determined by the pre-existing magnitude of the fluxes and the dropout effectiveness at low $L-$shells instead of by any process occurring afterwards. Figure 4.3(b,c) also indicates that enhancements are less extreme as L decreases, although the maximum fluxes can be 1-2 orders of magnitude higher than at GEO.

4.4 Correlation of fluxes as a function of L

We have discussed the general response of the outer radiation belt during REE events at GEO. To get a better idea of the coherence of the response across the belt for all events, we have calculated the correlation coefficient between the fluxes at GEO and at different $L-$shells for three quantities of interest: the maximum flux post enhancement ($t > 0$), the maximum flux pre enhancement ($t < 0$)and the pre-to-post flux ratio. Figure 4.4 shows the correlation coefficient between the maximum fluxes post $t > 0$ at GEO and maximum fluxes at different $L-$shells every $\Delta L = 0.5$. The correlation coefficient is very high $R > 0.8$ for $L > 4.5$, indicating that the response of the outer belt at $L > 4.5$ is in general similar to the response that the geostationary orbit is experiencing. The correlation coefficient quickly decreases in the region $L < 4.5$ and becomes very low ($R < 0.2$) for $L < 3.0$ showing that in this region the response is independent to what occurs at higher altitude. Similar figures for the correlation coefficients of maximum flux pre enhancement and ratios can be found at the end of the Chapter in Figures 4.8 and 4.9. Although they have a similar trend, they also show some significant differences.

Figure 4.5 shows the correlation coefficients obtained in Figure 4.4 as a function of $L-$shell, plus correlation coefficients calculated for maximum pre fluxes and for the ratio of change. The correlation coefficient is expected to increase and approach $R = 1$ as the measurements get closer together. Of course, the spatial gap between the Van Allen Probes and the GOES satellites ($\Delta L \geq 0.6$) plus the differences in the actual instruments (integrated channels in GOES versus differential energy channels in the Van

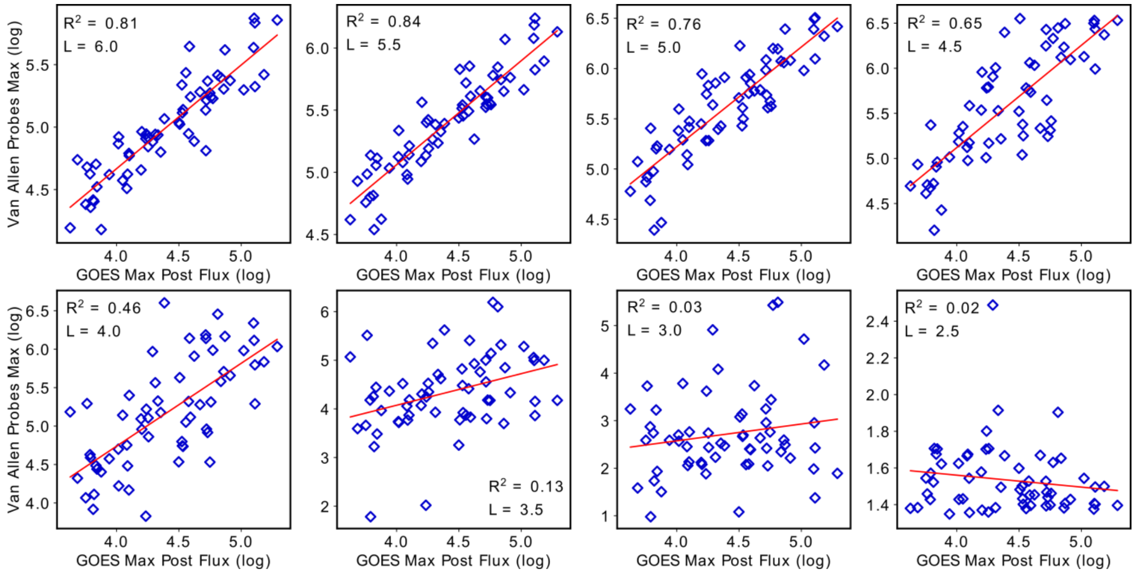

Figure 4.4: Maximum fluxes measured by GOES after $t = 0$ versus maximum fluxes measured by the Van Allen Probes at different $L-$shells. The red line indicates the best linear fit of the fluxes from which a correlation coefficient has been calculated, showing the general decrease in coherence as $L-$shell decreases.

Allen Probes), and calibrations can result in differences such that a perfect correlation is unlikely to be achieved. Still, for fluxes post enhancement the correlation coefficient is very high, peaking at $R = 0.94$ for $L = 5.8$. The slightly lower correlation coefficient at $L = 6.0$ is probably related to the lack of coverage from the Van Allen Probes during certain events since this L is larger than the radial distance of the spacecraft apogee, and thus requires data from off the equatorial plane, thus reducing accuracy relative to more equatorial measurements. The strong correlation for $L > 4.5$ and in particular for $L > 5.5$ confirms that by simply predicting the same flux evolution in this region as in GEO should have a very high accuracy.

Examining the correlation of post-to-pre flux ratios we observe a peak of $R = 0.8$ at $L = 5.8$ and a continuous near-linear decrease down to $R = 0.4$ at $L = 4.5$. Then, the correlation continues decreasing but at a slower rate down to $L = 3.5$ where it significantly drops again. The increase in correlation for $L < 3.1$ is yet another indication of how unaffected that part of the outer belt is for most of the enhancement events studied. Of course, correlation of fluxes for $t < 0$ does not depend on the geomagnetic driver resulting in relativistic enhancement event and it probably indicates a natural tendency

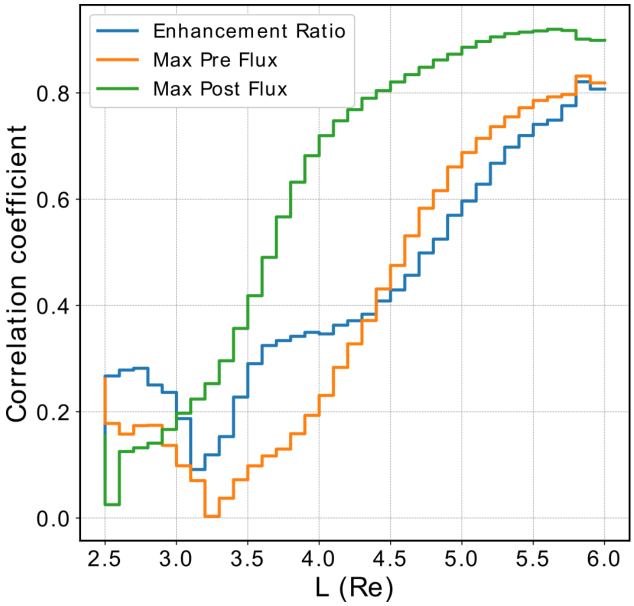

Figure 4.5: Correlation coefficients of GOES fluxes versus Van Allen Probes at different $L-$shells for flux ratio (blue line), maximum flux for post-event $t > 0$ (green line) and maximum flux for pre-event $t < 0$.

of the outer radiation belt to remain somewhat coherent in its evolution (*Kanekal et al.*, 2001). Still, a difference in correlation of up to ~ 0.25 in pre or post fluxes shows that geomagnetic activity results in a heavily organized outer belt. Recently *Baker et al.* (2019) calculated correlations coefficients of daily average fluxes between the Van Allen Probes and GOES data for most of the mission lifetime and found that fluxes are generally correlated to a high degree the closer they are. Still, it is noteworthy that there is a significant difference in the correlation between fluxes for $t < 0$ and for $t > 0$ that indicate that it is more likely to have better predictions capabilities for the outer belt if data from GOES satellites is used as a proxy once a REE is initiated.

By studying the occurrence rate of enhancement events as a function of $L-$shell and by calculating the flux correlations between GEO and different $L-$shells, we show that prediction of events should be possible and relatively simple for $L > 5.0$, and most likely remain very accurate for $L > 4.5$. We also know that relativistic electron events at GEO can be predicted with a fairly high degree of confidence when solar wind and magnetospheric conditions are known by using simple models (*O'Brien et al.*, 2001; *Lyons et al.*, 2009; *Lyatsky and Khazanov*, 2008; *Kim et al.*, 2015; *Pinto et al.*, 2018a) to indicate that an enhancement is likely to occur or with more complex models that will predict the maximum flux levels (*Baker et al.*, 1990; *Li et al.*, 2001; *Simms et al.*, 2014, 2016) facilitating a simple prediction mechanism for fluxes across the outer belt for $L > 4.5$. For lower $L-$shells, it may be possible to improve the correlations and, possibly, our degree of predictability if we improve our understanding of the response and occurrence of enhancements by accounting for geomagnetic activity or solar wind parameters.

4.5 Response to geomagnetic indices

It is well known that geomagnetic indices are useful at characterizing and sometimes predicting the response of the outer radiation belt, and so the most commonly used indices, SYM-H, Kp and AE are studied to determine if they improve the potential for prediction of the response of the belt during REE events at GEO. SYM-H minimum index (or D_{st}) is reflective of the ring current strength and is known to determine fairly well the location of peak electron fluxes in the outer radiation belt following geomagnetic storms (*Zhao and Li*, 2013; *Tverskaya et al.*, 2003; *Moya et al.*, 2017). The AE index is indicative of substorm particle injections into the inner magnetosphere and is considered relevant for the occurrence of REE events at GEO (*Kim et al.*, 2015; *Pinto et al.*, 2018a; *Hajra et al.*, 2015; *Antonova et al.*, 2018; *Li et al.*, 2009; *Borovsky*, 2017) and Kp index indicative of general magnetospheric convection and is regularly used in different forecasting models (e.g. NOAA).

To understand the response of the outer radiation belt to geomagnetic activity as reflected in different geomagnetic indices, we separate the events into 3 groups according to their intensity and describe how those groups of events differentiate from each other. For SYM-H index, we have separated our 60 events into three different groups of roughly the same size according to their minimum SYM-H value within $-24 < t < 24$ hrs. This separation results in thresholds of min(SYM-H) > -48 nT for weak or no storms (20 events), min(SYM-H) < -70 nT for strong storms (18 events). The group of min(SYM-H) in between those two quantities is referred to as the moderate storm group (18 events).

For the AE index, we have selected the three groups using thresholds of daily averaged AE index (for the first day of enhancement) of AE $<$ 325 nT (18 events) which will be named "low AE", 325 $\leq$ AE $\leq$ 430 nT (20 events) which we will refer to as "moderate AE" and AE $>$ 430 nT (22 events) "strong AE". It is important to mention that compared to quiet times, all these events are actually "strong AE" and our sub-division only makes sense with that understanding in mind. For the Kp index the separation is considered weak for Kp $\leq$ 4.7, moderate for 5.0 $\leq$ Kp $<$ 5.7 and strong for Kp$\geq$ 5.7.

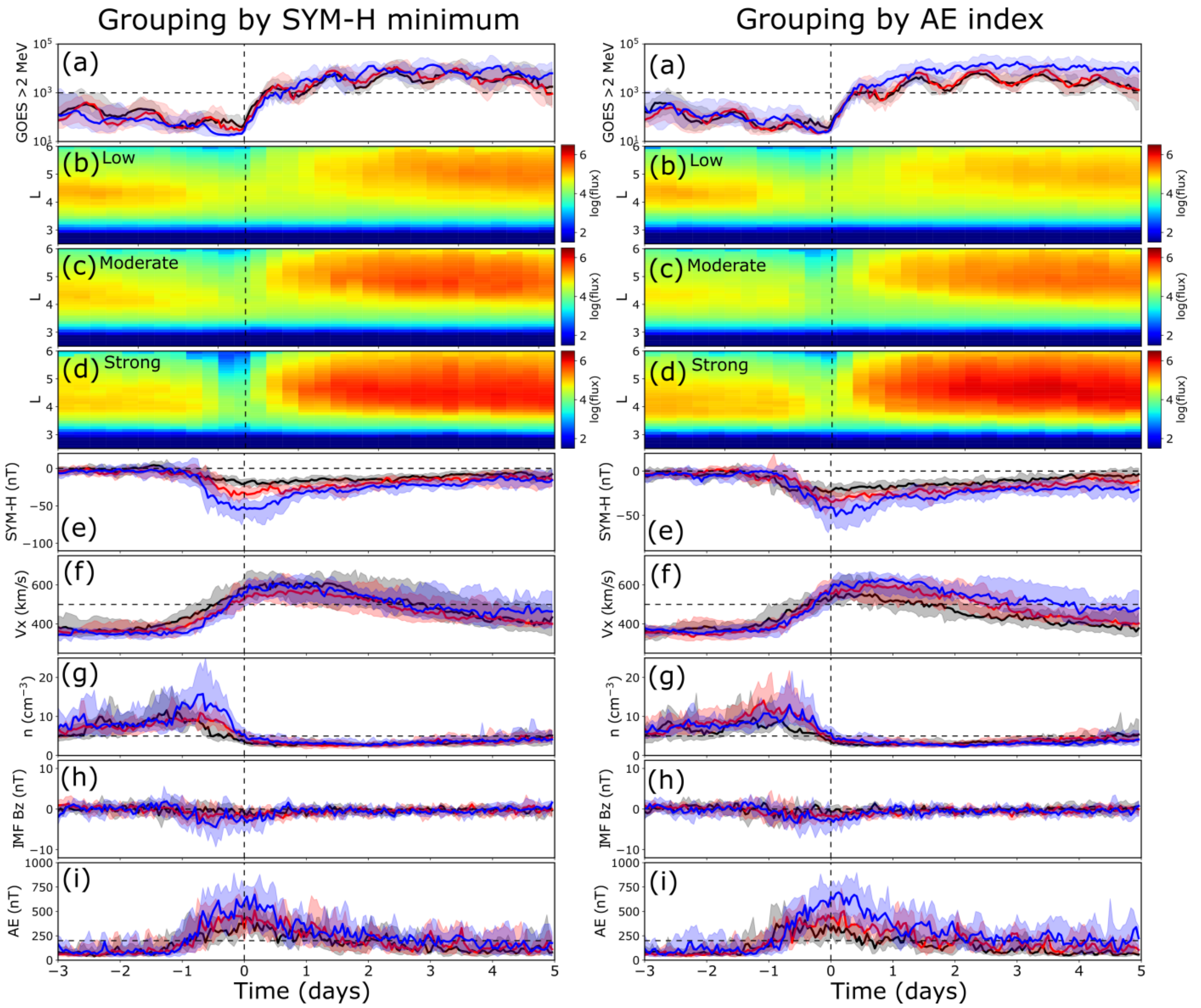

Figure 4.6: Superposed Epoch Analysis of all events separated according to their SYM-H minimum values (left) and to their averaged AE index (right). From top to bottom (a) GOES $>$ 2 MeV fluxes (e) SYM-H index (f) Solar Wind Speed (g) Solar wind proton density (h) IMF Bz (h) AE index. Solid lines represent median values and the envelopes represent the quartile distributions. Black color is used for weak index group, red for the moderate index group and blue for the strong index group. Van Allen probes$E = 2.1$ MeV flux distribution (median) are shown in panels (b) weak (c) moderate and (d) strong.

Figure 4.6 shows a superposed epoch analysis of all events when divided according to their SYM-H minimum value within a day of $t = 0$ (left) or according to their daily average AE index strength for the first day of enhancement $0 < t < 24$ hrs. (right). Similar figures for Kp index and for all events combined are available at the end of the chapter in Figures 4.10 and 4.11. Separation according to a particular geomagnetic results in partial separation of other indices as they present some degree of correlation. For example when separating according to min(SYM-H), the events with the strongest drops also have the highest AE indices during the period of enhancement. Similarly, when sorting by the AE indices, increasing AE intensity also results in more pronounced decreases in SYM-H. Nevertheless, we can still get relevant information from this sorting for singular parameters. Possibly the most relevant information is that minimum SYM-H does not discriminate the statistical evolution of fluxes at geostationary orbit. It can be seen in panel 4.6(a) that all groups present a very similar temporal evolution at GEO with very similar median values, regardless of that group they are in. In contrast, AE index does a somewhat better job at discriminating the final flux values at GEO based on this group separation. Of course, both minimum SYM-H and AE index separation are significantly better in describing the outer belt response at lower $L-$shell as seen from the Van Allen Probes perspective. Fluxes with a low minimum SYM-H index drop or the lowest AE index take more time reaching enhanced levels and they develop predominantly at high L-shells (panel 4.6(b). Strong SYM-H drops and the strongest AE index groups develop enhancement across the belt significantly faster and over a wider range of L-shells, with peaks in flux being higher in value and developed at lower $L-$shells compared to the other groups. The top 4 panels in each column of Figure 4.6 show the essential point of this study, namely that similar enhancements of relativistic electron fluxes at GEO can result in vastly different responses at lower $L-$shells, including the heart of the radiation belts. As a result, studies that only focus on electron fluxes at GEO as a proxy for the entire outer radiation belt and draw conclusions about the radiation belt dynamics from just this one location can be misleading or sometimes simply wrong, as evidenced by the range of responses shown in panels 2-4 from the top. Fortunately, it appears that even a single geomagnetic index combined with fluxes at GEO can significantly improve the predictability of the outer radiation belt at regions interior to GEO.

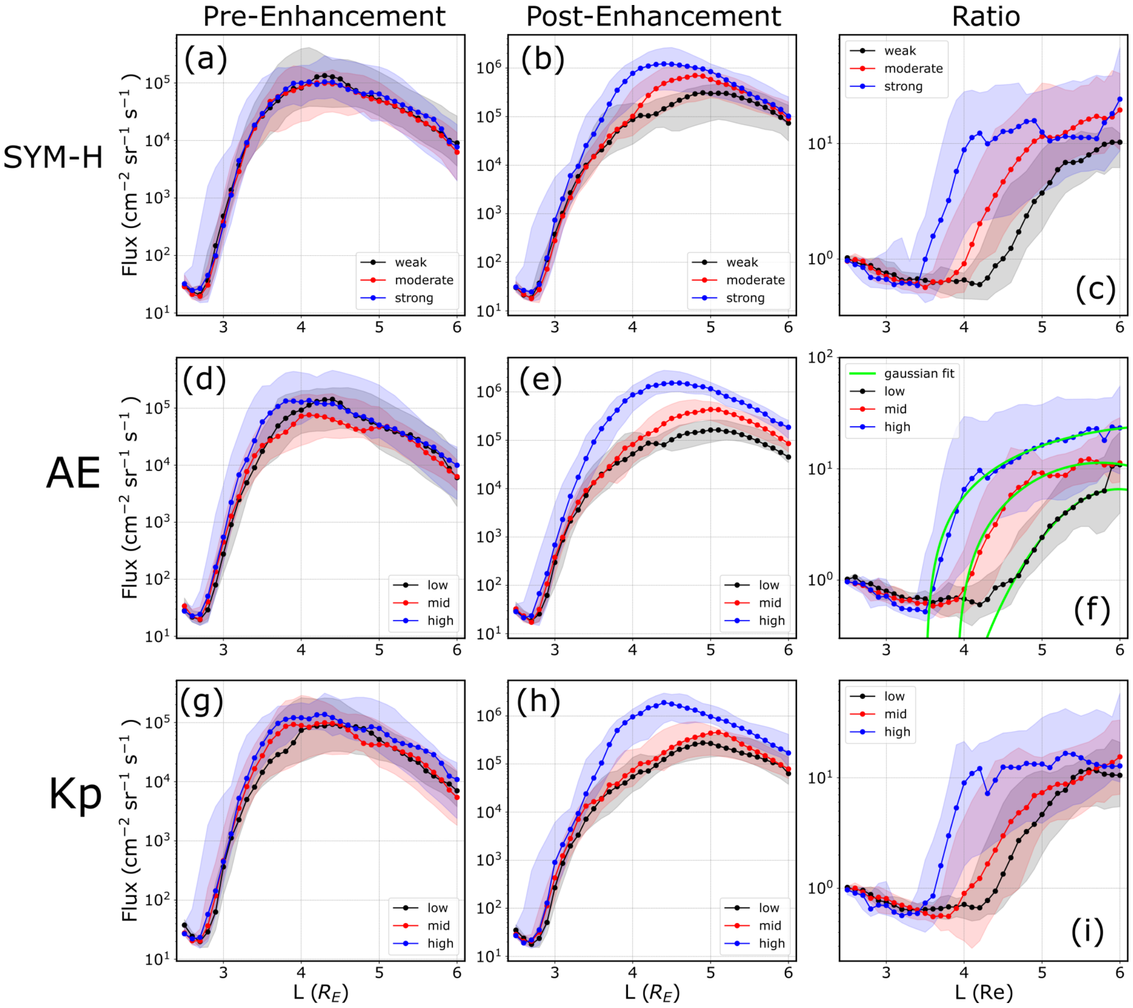

Figure 4.7: (a) Distribution of maximum fluxes for $t < 0$ when separated in three different groups according to their SYM-H minimum values. Black corresponds to weak (or no) storm, red corresponds to moderate storms and blue corresponds to strong storms. Dotted lines corresponds to the median of each distribution and the colored envelopes to the upper and lower quartiles. (b) Same as in (a) but showing maximum fluxes for $t > 0$. (c) Same as in (a) but for the ratio of change in fluxes. (d-f) Same as in (a-c) but when separating by daily average AE index during the first day after $t = 0$. (g-i) Same as in (a-c) but when separating by maximum Kp index. Green lines in panel (f) correspond to the best Gaussian fit for each of the median curves.

Figure 4.7 shows the distribution of maximum electron fluxes before $t = 0$ (a) post $t = 0$ (b) and the post-to-pre flux ratios (c) for all three different groups. Colored dots represent each group; black for the lowest values group, red for the moderate values group and blue for the strong values group. Colored envelopes represent their respective quartile distributions. Figure 4.7(a) indicates a lack of intense pre-event fluxes on the belt favoring a particular group of SYM-H minimum, and that therefore post flux and ratio should offer some valuable information. Figure 4.7(b) quantifies what Figure 4.6 clearly shows, that being for $L > 5.5$ the SYM-H minimum has little impact of the resulting maximum fluxes whereas it plays a very important role in the region $3.5 < L < 5$. It can also be appreciated how even statistically the peaks in flux move inward as the SYM-H minimum decreases. Figure 4.7(c) also offers some of that information as it is clear that the ratio has a very strong dependence with SYM-H in the region $3.5 < L < 5.0$.

Figure 4.7(d-i) present the corresponding distributions when events are separated by the magnitude of the daily averaged AE index (d-f) calculated for the first day after $t = 0$. Figure 4.7(d) shows that although the distributions seem to be relatively similar to each other, they are not identical and the moderate AE group has a slightly lower median in the region $3.7 < L < 5$. We do not anticipate that a pre-conditioning exists here, but the difference may need to be considered when discussing ratios. Figure 4.7(e) shows extremely clearly separated distributions for all $L > 3$ when daily average AE is larger than 430 nT and for all $L > 4$ for all three groups. Although it is known that AE plays an important role in enhancement events at GEO, it is remarkably how well it differentiate post enhancement fluxes at low L-shells. Figure 4.7(f) shows the ratio of change between maximum post-to-pre fluxes and again the separation is very clear from one group to the other. Given that AE index presents the most clear separation, we fit each distribution to a Gaussian of the form

$$R = A \exp\left(\frac{(L - L_0)^2}{\sigma}\right) + c$$

where the parameters A, L_0, σ and c have been determined numerically by minimizing the sum of the squared residuals. Table 4.1 shows the values that provide the best Gaussian fits for all three groups. Although far from perfect, as a first approach to the problem it at least indicates that the response of the radiation belt presents a coherent response that increases, widens in L-shell extent, and moves inward as AE index increases.

Table 4.1: Gaussian fit coefficients for post-to-pre flux ratios as a function of AE intensity

	A	L_0	σ	c
Lowest AE	6.62	5.98	0.98	-0.05
Mid AE	16.8	5.75	3.08	-5.50
Largest AE	55.9	6.70	17.66	-31.2

Figure 4.7(g-i) show the distributions for Kp index. Interestingly, Kp index shows little differences in the two lowest groups, which behave similarly in terms of maximum post-fluxes and ratio of enhancement, but for events with $Kp > 5.7$ there is a huge difference in their response through the outer belt. Kp at GEO does show some minor differences across the groups, with the highest Kp events exhibiting a slightly larger statistical increase relative to the other two groups (see Figure 4.11), and that difference can be appreciated down to $L = 5$. However, events with high Kp show a significant difference in the region $3.5 < L < 5.0$ compared to the other two groups, again showing that this particular parameter can be of utility when trying to estimate the fluxes across the radiation belt based on information from GEO. Since Kp and Ap are related to each other, this result is consistent with the findings of *Mourenas et al.* (2019) who showed that elevated integrated Ap results in high peaks of $E = 2.1$ MeV across the outer belt.

4.6 Discussion and Conclusions

In our study, we identified 60 relativistic electron enhancement events that were observed at geostationary orbit between 01 September of 2012 and 31 December 2017 using data available from GOES 15 > 2 MeV electrons and the criteria previously established in *Pinto et al.* (2018a). By comparing against simultaneous data available from the Van Allen Probes ECT-REPT (*Baker et al.*, 2013b) instrument we studied the response of the $E = 2.1$ MeV electron channel during those 60 REE events.

We have found that despite all events starting off as enhancements in the external part of the outer belt (by definition), the occurrence rate (that is the percentage of events that results in enhancement) decreases significantly for $L < 5.0$ and that some enhancement events can actually result in a depletion of fluxes for $L < 4.6$. Those depletion rates are generally slow and they tend to peak at $L = 4.0$ which may be an indication of a local loss mechanism. The most general behavior is that as L decreases further, the post-to-pre flux ratio gets closer to unity, indicating that the penetration of the enhancement event is always limited to some extent, such that almost no enhancement occurs below $L = 3.0$.

By studying the correlation between flux enhancements at geostationary orbit with contemporaneous fluxes provided by the Van Allen Probes as a function of L, we find that maximum post event fluxes present a very strong correlation between these two regions. Recently, *Baker et al.* (2019) showed that the correlation coefficient between GEO and different $L-$shells is generally high for any day, and that can be seen by the fact that even pre-enhancement fluxes are relatively well correlated for $L > 4.5$. However, post-enhancement event fluxes present a much larger correlation down to $L = 4.0$ indicating that predictions of the response of the belt up to that point should be relatively accurate, but only at post-enhancement times.

We have also studied the response of the outer radiation belt when we separate the events according to the strength of certain geomagnetic indices, in particular SYM-H, AE and Kp, since they are all known to be effective at modulating the response of the outer belt. We have found so far that all three studied parameters are useful in describing part of the response of the outer belt in terms of ratio of enhancement, peak of the fluxes and maximum post flux values and location. We also examined several solar wind parameters (solar wind speed, solar wind proton density, solar wind dynamic pressure, IMF southward directed B_z and time of southward directed B_z) attempting to separate them in three groups as we did with geomagnetic indices. We have included those results in Figure 4.12, because the solar wind parameters leading to enhancement events are strongly correlated with geomagnetic indices. Thus, the results are somewhat redundant with what we have discussed already.

This study has attempted to quantify what other studies have suggested, that fluxes at GEO can be used as a proxy for the fluxes throughout the whole outer radiation belt. In a first step, we have demonstrated that it is possible to use GEO for the occurrence of enhancement events and enhanced fluxes with high accuracy for $L > 5$ and with moderate accuracy for $L > 4$. While reconstructing the fluxes of the radiation belt in real time using proxy data seems unlikely, and it is necessary to have real time in-situ measurements for increased prediction potential, the use of GEO. Although not discussed here, it is possible that by adding GPS and low altitude measurements results in an improved description of the system, in particular at lower ($L < 4$) radial distances and therefore improved predictions of fluxes throughout the outer radiation belt.

Table 4.2: List of relativistic electron enhancement events used for this study. Dates correspond to the first positive gradient in fluxes leading to an enhancement detected by GOES satellites (rounded to the nearest hour). Table also shows minimum SYM-H index associated with each event and the solar wind driver

Event Date	SYM-H min	Driver	Event Date	SYM-H min	Driver
2012-10-08/22:00	-116	CME	2016-05-08/13:00	-105	CIR
2013-03-01/18:00	-76	CIR	2016-06-25/00:00	-40	CIR
2013-04-25/12:00	-52	CIR	2016-07-08/09:00	-36	CIR
2013-06-22/08:00	-27	CIR	2016-08-03/12:00	-63	CIR
2013-07-10/08:00	-57	CME	2016-08-24/12:00	-83	CIR
2013-08-05/00:00	-56	CIR	2016-09-01/14:00	-74	CIR
2013-08-16/04:00	-54	CIR	2016-09-27/06:00	-51	CIR
2013-09-01/04:00	-42	CIR	2016-10-13/19:00	-114	CME
2013-09-19/08:00	-31	CIR	2016-10-25/12:00	-81	CIR
2013-10-15/11:00	-52	CIR	2016-11-12/13:00	-55	CME
2014-04-24/15:00	-28	-	2016-11-25/01:00	-53	CIR
2014-08-29/09:00	-90	CME	2016-12-08/14:00	-33	CIR
2014-10-21/12:00	-57	CIR	2016-12-22/06:00	-52	CIR
2014-11-15/12:00	-51	CIR	2017-01-05/12:00	-47	CIR
2014-12-07/12:00	-34	CIR	2017-01-31/21:00	-48	CIR
2015-02-02/12:00	-52	CIR	2017-03-01/18:00	-74	CIR
2015-03-18/04:00	-234	CME	2017-03-22/09:00	-46	CIR
2015-04-16/12:00	-88	CIR	2017-04-20/18:00	-48	CME + CIR
2015-05-13/09:00	-98	CIR	2017-05-20/09:00	-44	CIR
2015-06-08/17:00	-105	CIR	2017-06-17/12:00	-38	CIR
2015-08-16/00:00	-94	CME	2017-07-16/17:00	-67	CME
2015-11-03/18:00	-67	CIR	2017-08-05/06:00	-35	CIR
2015-12-01/14:00	-45	-	2017-08-18/08:00	-36	CIR
2016-01-21/15:00	-95	CIR	2017-09-01/08:00	-64	CIR
2016-02-16/17:00	-58	CIR	2017-09-15/04:00	-44	CME
2016-03-07/09:00	-110	CME	2017-09-28/00:00	-74	CIR
2016-03-15/08:00	-62	CIR	2017-10-12/09:00	-49	CIR
2016-04-03/09:00	-66	CIR	2017-11-07/23:00	-89	CIR
2016-04-13/10:00	-70	CME	2017-12-05/14:00	-47	CIR
2016-05-02/12:00	-56	CIR	2017-12-17/15:00	-34	CIR

Table 4.3: Quartile distribution of Van Allen Probes fluxes (cm^{-2} sr^{-1} s^{-1}) for $E = 2.1$ MeV, calculated during the Whole mission (September 2012 – September 2019) as a function of $L-$shell. Events were required to have fluxes larger than the lower quartile to be considered enhancements

$L-$shell	25 %	Median	75 %
2.5	15.53	22.40	32.55
2.6	11.63	15.99	23.17
2.7	10.39	14.07	23.23
2.8	10.55	19.39	64.73
2.9	14.28	49.58	240.22
3.0	33.43	156.44	819.66
3.1	85.06	426.90	2364.13
3.2	190.63	1114.88	6443.03
3.3	409.32	2524.59	14221.93
3.4	757.59	4874.42	26063.81
3.5	1286.06	8504.76	43179.70
3.6	1993.50	13666.83	66083.67
3.7	3068.88	20163.92	94317.29
3.8	4399.40	28050.31	120537.17
3.9	5965.74	35663.38	143403.92
4.0	7217.88	43177.72	165639.49
4.1	8399.07	50238.59	186396.22
4.2	9989.00	56793.11	204958.64
4.3	11123.76	61578.79	216056.93
4.4	11903.25	64920.84	223780.01
4.5	12143.37	66530.72	226083.62
4.6	12027.03	65497.66	222541.06
4.7	11663.24	62136.76	213123.06
4.8	11193.28	58103.48	200848.46
4.9	10389.19	53294.99	185670.35
5.0	9522.71	47903.37	166824.56
5.1	8383.06	41427.08	146981.88
5.2	7233.23	35500.18	128069.96
5.3	6033.02	30436.64	109564.06
5.4	4974.95	25838.21	92397.94
5.5	4053.53	21760.50	76863.51
5.6	3226.00	18003.02	63494.91
5.7	2565.33	14682.10	51968.19
5.8	2165.55	12356.97	43385.67
5.9	1833.21	10480.01	36794.99
6.0	1411.35	8266.98	30555.86

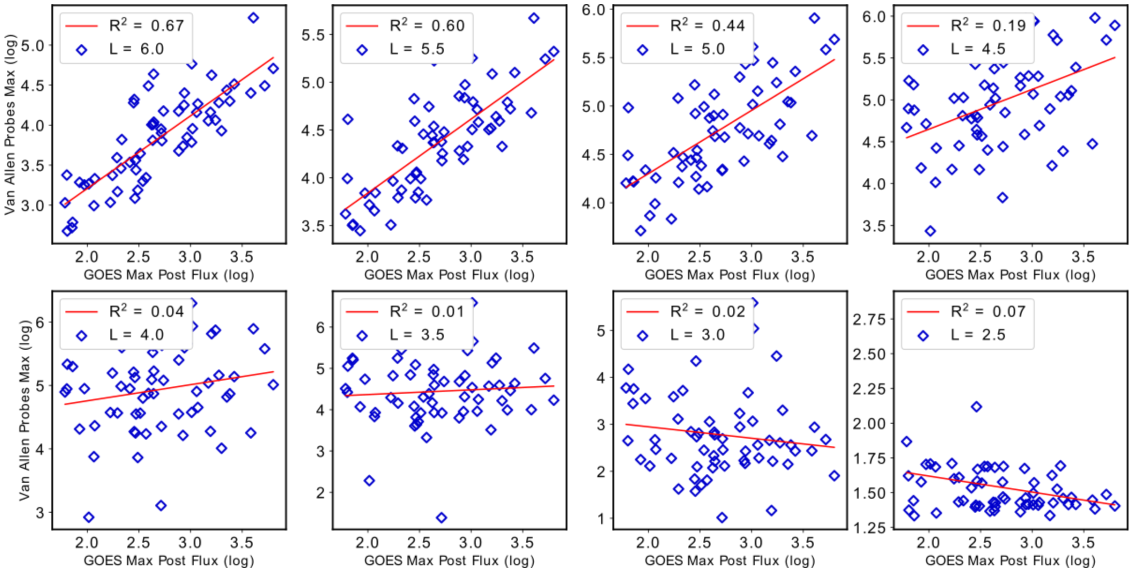

Figure 4.8: Maximum fluxes measured by GOES for t<0 versus maximum fluxes measured by the Van Allen Probes. The red line indicates the best linear fit of the fluxes from which a correlation coefficient has been calculated, showing the general decrease in coherence as L-shell decreases

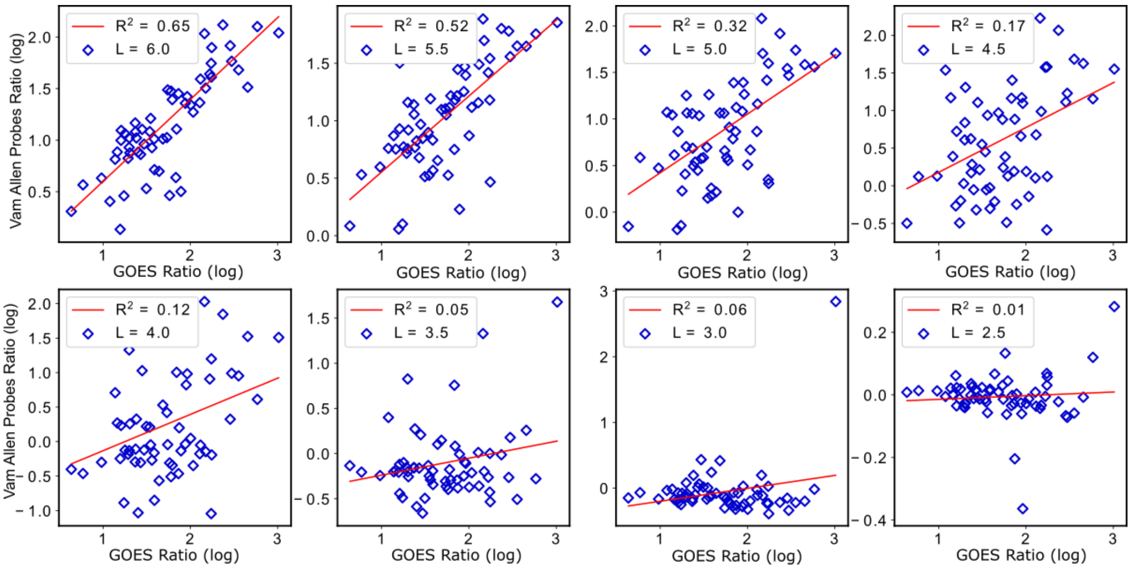

Figure 4.9: Ratio of post-to-pre fluxes measured by GOES versus ratio of fluxes measured by the Van Allen Probes. The red line indicates the best linear fit of the fluxes from which a correlation coefficient has been calculated, showing the general decrease in coherence as L-shell decreases

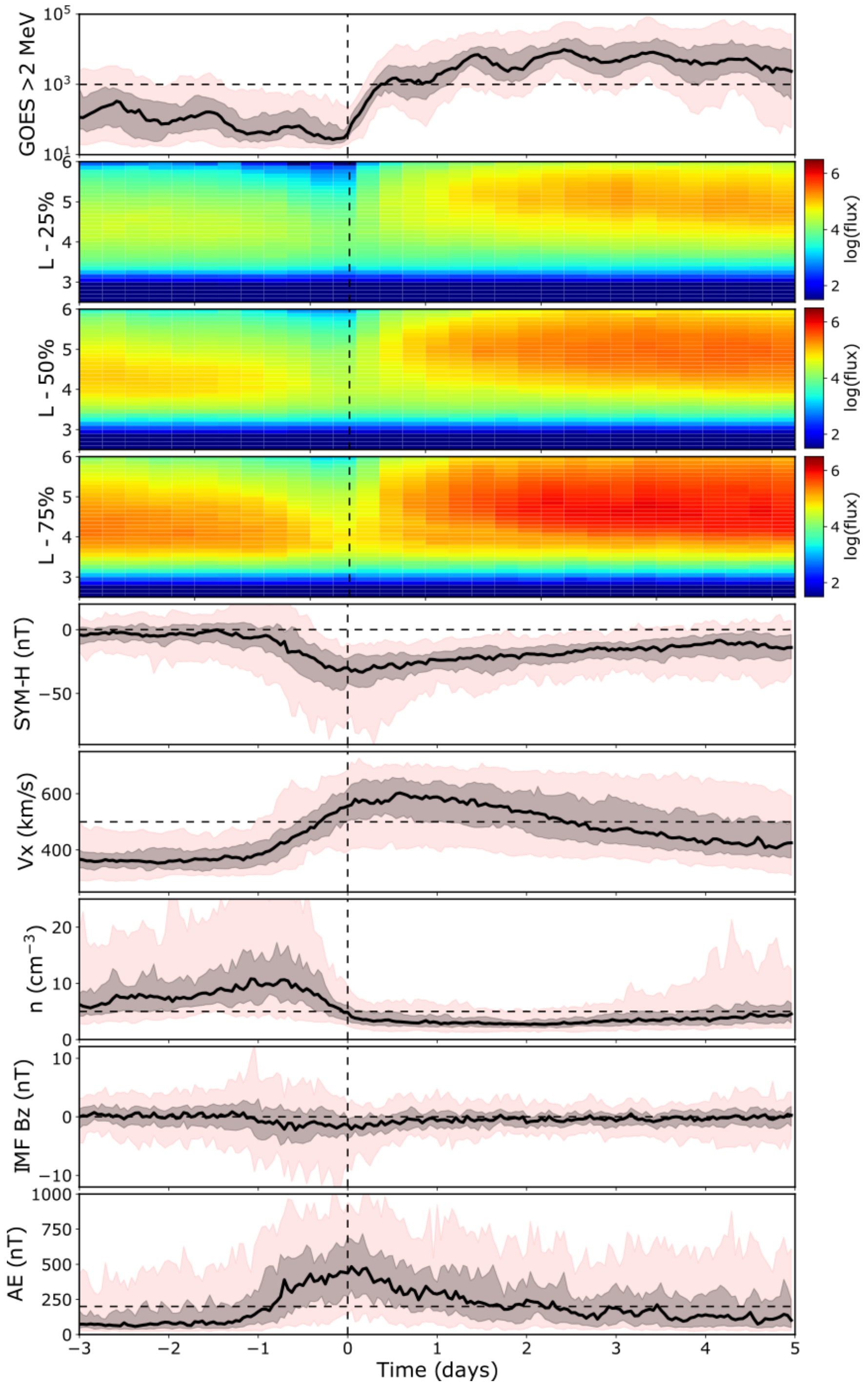

Figure 4.10: Superposed Epoch Analysis of all events. From top to bottom (a) GOES $>$ 2 MeV fluxes (e) SYM-H index (f) Solar Wind Speed (g) Solar wind proton density (h) IMF B_z (h) AE index. Solid lines represent median values, black envelopes represent the quartile distributions and pink envelopes represent the 5th and 95th percentiles. Panels (b), (c), (d) shows the quartile distributions of Van Allen Probes $E = 2.1$ MeV fluxes.

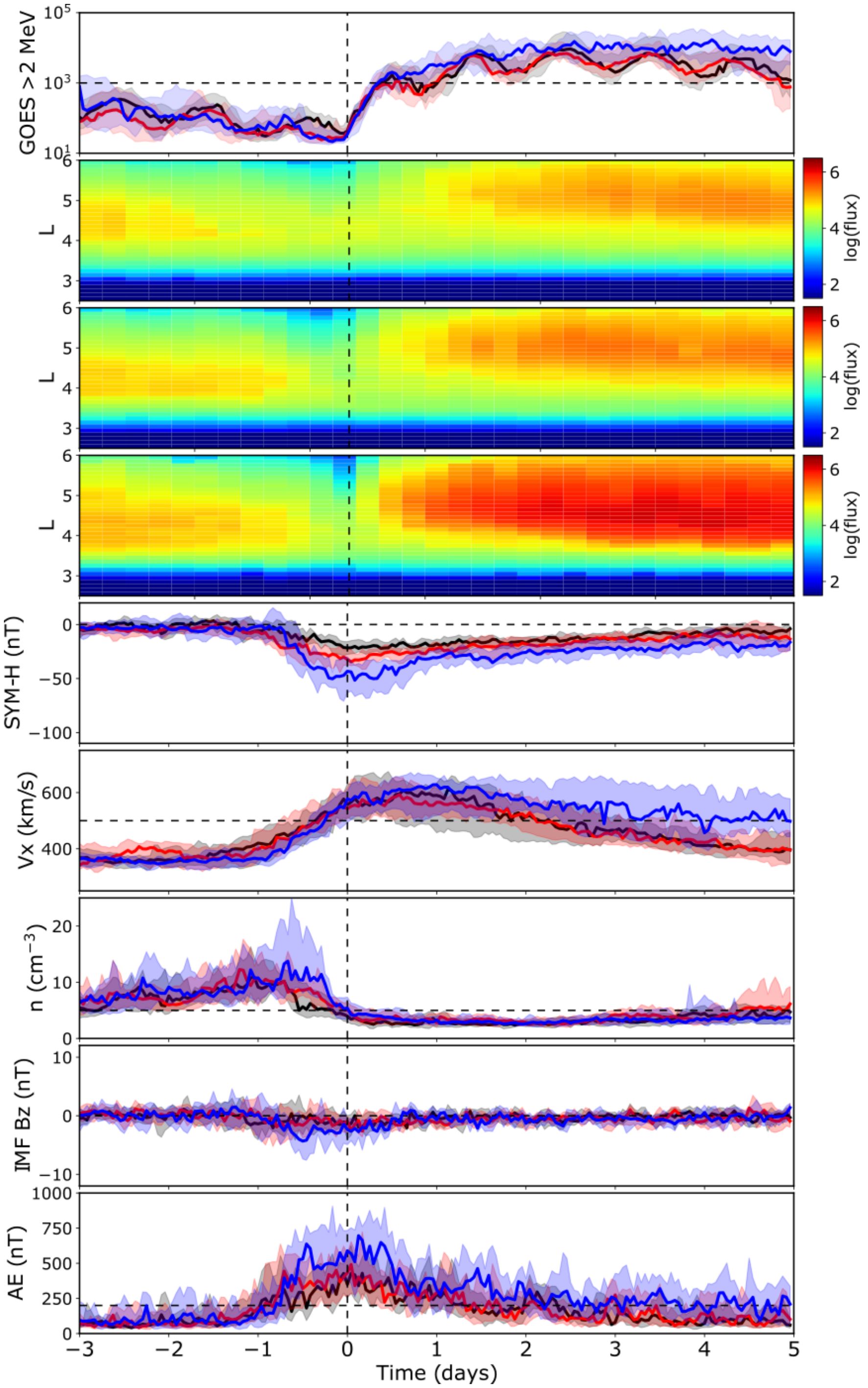

Figure 4.11: Superposed Epoch Analysis of all events separated according to their Kp maximum values. From top to bottom (a) GOES > 2 MeV fluxes (e) SYM-H index (f) Solar Wind Speed (g) Solar wind proton density (h) IMF B_z (h) AE index. Solid lines represent median values and the envelopes represent the quartile distributions. Black color is used for weak index group, red for the moderate index group and blue for the strong index group. Van Allen probes $E = 2.1$ MeV flux distribution (median) are shown in panels (b) weak (c) moderate and (d) strong

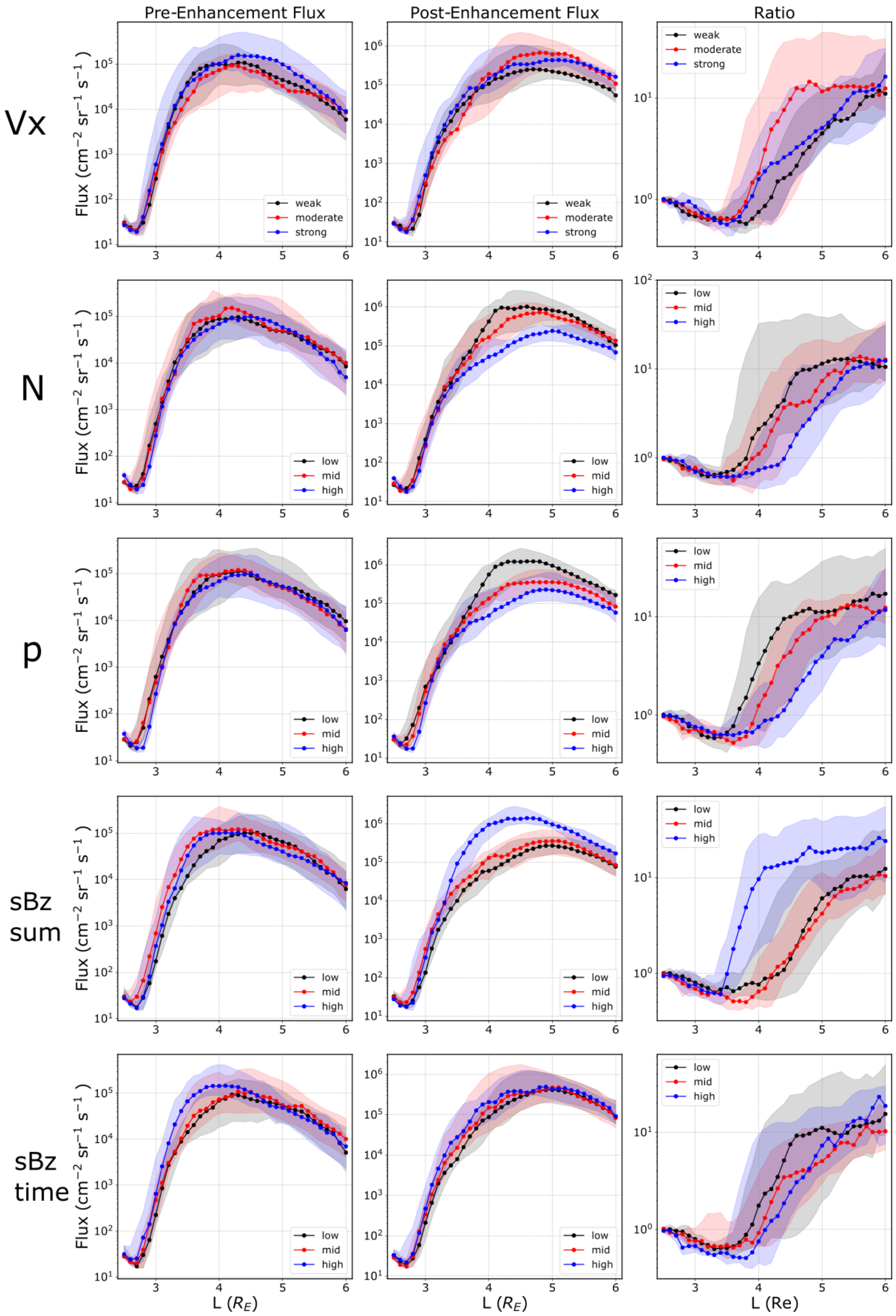

Figure 4.12: Distribution of maximum fluxes for t<0 (left) when separated in three different groups according to their solar wind speed average value (top) for $0 < t < 1$ day. Black corresponds to lowest speed; red corresponds to mid speeds and blue corresponds to highest speeds. Dotted lines correspond to the median of each distribution and the colored envelopes to the upper and lower quartiles. Middle panel show maximum fluxes for t>0. Right panel shows the ratio of change in fluxes. Bottom panels show the same but for separation of minimum solar wind proton density (N), dynamic pressure (p), cumulative southward B_z and average time of southward directed B_z

CHAPTER 5

Characteristics, Occurrence and Decay Rates of Remnant Belts associated with Three-Belt events in the Earth's Radiation Belts

The material in this chapter has already been published in *Geophysical Research Letters* (*Pinto et al.*, 2018b). The text is presented with some minor modifications from the originally published version to include the supporting material.

5.1 Introduction

The Earth's electron radiation belts (*Van Allen and Frank*, 1959), located approximately between $1.2 < L < 7$, consist of a very stable inner zone, a "slot" region (*Lyons and Thorne*, 1973), and a very dynamic outer zone in which electron populations of energies from keV to MeV can vary by several orders of magnitude in periods ranging from hours to a few days (e.g. *Thorne*, 2010; *Reeves et al.*, 2016; *Baker et al.*, 2018). The outer zone extreme dynamics are ultimately driven by the solar wind interacting with the magnetosphere, therefore the relation between geomagnetic storms (*Gonzalez et al.*, 1994), and flux variations in the outer radiation belt has been extensively studied. It has been consistently found that, while geomagnetic storms favor enhancements of electrons fluxes, they can also result in depletions, or cause little variation to the outer belt electron populations (*Reeves et al.*, 2003; *Kataoka and Miyoshi*, 2006; *Yuan and Zong*, 2012; *Zhao and Li*, 2013; *Turner et al.*, 2015; *Moya et al.*, 2017).

The Van Allen Probes mission was designed to study the radiation belts and to answer some of the many unknowns regarding their internal dynamics (*Mauk et al.*, 2013). One of the first results of the mission was the discovery of a temporary third belt at high energies that lasted a month (*Baker et al.*, 2013a). The creation of this three-belt configuration was a product of a partial depletion of the outer belt that left a remnant belt at $2.8 < L < 3.5$, and that was followed by a recovery of electron fluxes at $L > 4$ for energies > 3.4 MeV. To explain the formation of the remnant belt, *Shprits et al.* (2013, 2018) argued that simulation of losses by scattering of electrons with electromagnetic ion-cyclotron (EMIC) waves can replicate the remnant belt formation, while *Mann et al.* (2016, 2018) has argued that EMIC wave scattering is not needed as losses to the magnetopause by a combination of inward motion of the magnetopause and fast outward diffusion driven by ULF waves was sufficient to replicate the observations. The decay of the remnant belt has been studied by *Thorne et al.* (2013b) who argued that that a remnant belt trapped in the plasmasphere by a rapid expansion of the plasmapause will only present a slow decay, due to interactions with hiss waves.

To date, only few remnant belt events have been reported during the Van Allen Probes era, (e.g. *Kellerman et al.*, 2014; *Baker et al.*, 2016) and no statistical analysis has been performed to characterize them. The most comprehensive studies come from *Turner et al.* (2013) who reported 13 double peak occurrences in phase space density of equatorially mirroring electrons between the years 2007 and 2011 using data from the Time History of Events and Macroscale Interactions during Substorms (THEMIS) spacecraft and from *Yuan and Zong* (2013a) who reported 8 three-belt events between the years 1994 to 2003 using data from the low altitude Solar Anomalous and Magnetospheric Particle Explorer (SAMPEX) spacecraft. However, the different techniques, instruments and measurements used both in *Turner et al.* (2013) and *Yuan and Zong* (2013a) make it difficult to compare with Van Allen Probes era events. Additionally, the original September 2012 event reported is still the subject of disagreement with respect to the dominant process responsible for the formation of the remnant belt. In this work, for the first time we catalog three-belt events that occurred during the Van Allen Probes era, from September 2012 to November 2017. We report on the main characteristics of the events and discuss the process of decay of the remnant belt.

5.2 Data and Events

The Van Allen Probes have a highly elliptical (apogee ~ 5.8 R$_E$), near-equatorial (inclination $\sim 10°$) orbit with period ~ 9 hours. The satellites follow each other with separations that vary from $\sim$ 1 hour to half-orbit, therefore any particular radial distance gets is surveyed every few hours. To identify three-belt events we have used spin-averaged electron flux data obtained from the Energetic Particle Composition and Thermal Plasma Suite (*Spence et al.*, 2013) Relativistic Electron Proton Telescope (ECT-REPT) (*Baker et al.*, 2013b) on board the Van Allen Probes. We have combined the data from both satellites into a single grid of data points binned in space $\Delta L = 0.1$) and time ($\Delta t = 6$ hours) by averaging all data points available inside each bin, during the time period from 01 September 2012 to 30 November 2017. Here L corresponds to the dipole L (the radial distance at which a magnetic line would cross the equator). Solar wind data and magnetospheric indices have been obtained from the OMNI database. Magnetopause standoff location was calculated using the corrected Shue model (*Shue et al.*, 1998).

Figure 5.1 (left) shows a three-belt event that started on 27 September 2017 following a high-speed stream (HSS) arrival that resulted in a moderate geomagnetic storm (SYM-H minimum -74 nT). Panels (a) to (d) show the evolution of electron fluxes for energies between 2.6 MeV and 5.2 MeV in the region 2.5$< L <$6. Electron fluxes at $L >$3.5 were depleted around the time a sharp increase in solar wind dynamic pressure arrived (panel i). As a result, a remnant belt stayed in place in 2.8$< L <$3.2. The partial depletion was followed by an enhancement of the outer belt at higher L-shells during the recovery phase of the storm that resulted in a stable three-belt configuration (inner belt is not shown). Panel (e) shows that with the arrival of the high-speed stream the magnetopause standoff location briefly moved down to $L =$6.0 (2017-09-27/07:30 UT), which match with the time of the partial depletion. The three-belt configuration lasted until 11 October 2017 when another high-speed stream driven storm completely depleted the

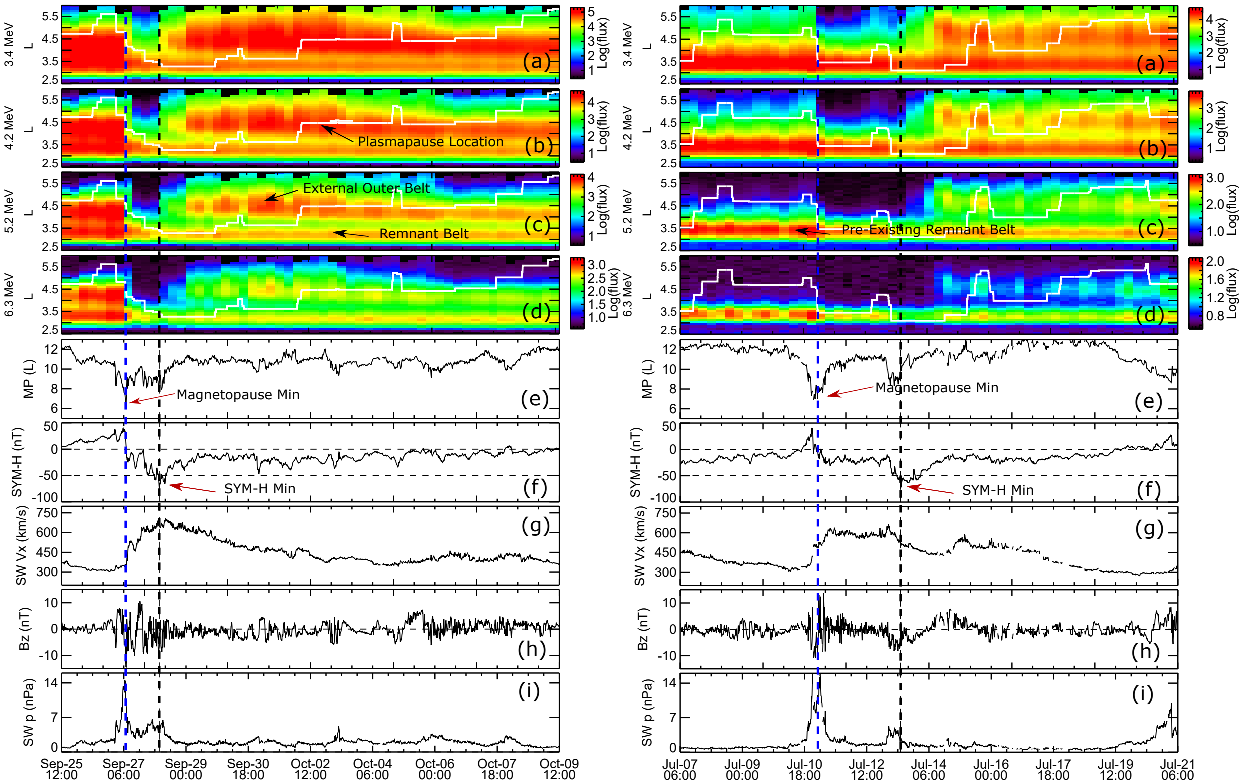

Figure 5.1: Example of a three-belt event that started 27 September 2017 (left) and a second event that started on 13 July 2015 (right). From top to bottom: spin-averaged combined electron fluxes from Van Allen Probes as a function of L for energy channels (a) 2.6 MeV, (b) 3.4 MeV, (c) 4.2 MeV, (d) 5.2 MeV. Panel (e) corresponds to the estimated magnetopause standoff location, panel (f) to the SYM-H index. Bottom three panels show solar wind parameters such as speed V_x (g), IMF B_z (h) and dynamic pressure P_{dyn} (i). The blue dashed line corresponds to the time of magnetopause minimum. The black dashed line corresponds to SYM-H minimum.

outer belt (not shown). Plasmapause location calculated by the AE-dependent *O'Brien and Moldwin* (2003) empirical model (shown in panels (a) to (d) as a white line) defines with relative accuracy the penetration and the initial depletion after the arrival of the high-speed stream, suggesting that a plasmapause effect may prevent a complete disappearance of the outer belt and therefore help the “formation" of a remnant belt. The plasmapause location moves outward in the following days, consistent with the idea that the remnant belt can remain in place if it’s shielded from loss and acceleration processes outside the plasmapause that result in the creation of the new external outer belt. Figure 5.1 (right) shows another three-belt event that started around 13 July 2015 also in association with a moderate storm resulting of the arrival of a high-speed stream on 10 July

2015 and a small CME on 13 July 2015 (SYM-H minimum -71). In this case the magnetopause was also pushed inward down to L =6.3 in association with a sharp increase in solar wind dynamic pressure. In this event, a pre-existing remnant belt was already in place and was affected only moderately by the pressure shock arrival, and only after a few days the formation of the new outer belt lead to a three-belt event.

For the period between September 2012 and November 2017, we found 30 events that present a three-belt structure, defined as an extended period of time ($>$ 1 day or about 3 satellites orbits) in which a double peak in flux versus L is observed beyond the slot region at L =3, in at least one energy channel in the range 1.8$\leq E \leq$7.6 MeV. We checked all energy channels individually to determine if there is a triple belt or a remnant belt only. Table 5.2 presents a list of all the event dates, SYM-H minimum for each event, the interplanetary driver associated with each event, magnetopause minimum location, the range of energies at which each event presents a three-belt structure and whether there was a pre-existing remnant belt or not.

5.3 General characteristics of three-belt events

Three-belt events occur under a variety of geomagnetic conditions, associated with high-speed streams (HSS) that either result in geomagnetic storms (13 events or 43%) or do not (10 events or 33%) while other events are associated with CME-driven storms (5 events or 17%) and finally some occur in association with geomagnetic storms that resulted from the combination of CME and HSS (2 events or 7%). If we consider all geomagnetic storms that occurred between September 2012 and November 2017, the fraction that resulted in three-belt events were 13 of 46 (28%) for high-speed streams, 5 of 48 (10%) for CMEs and 2/15 (13%) for CME + HSS storms. These numbers, when combined indicate that 18% of all geomagnetic storms lead to three-belt events. We have not calculated the occurrence rate for high-speed streams not resulting in geomagnetic storms, but these do occur, a result that is consistent with the current notion that a traditional geomagnetic storm is not needed to drive an enhancement of electrons in the radiation belts (e.g. *Schiller et al.*, 2014; *Kim et al.*, 2015; *Pinto et al.*, 2018a).

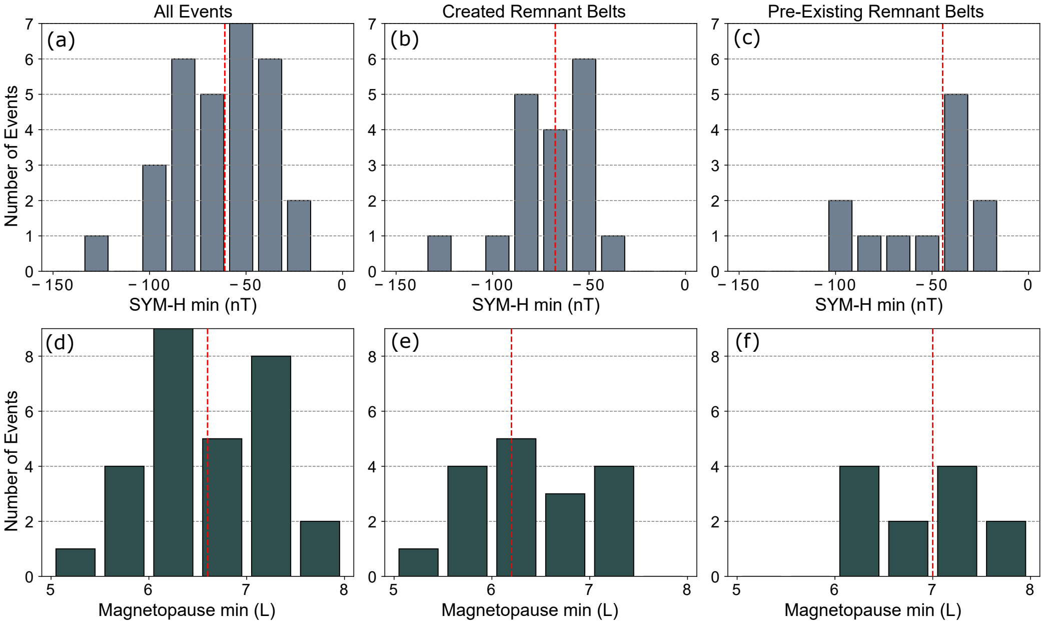

Figure 5.2: SYM-H minimum (top) and Magnetopause standoff minimum L value (bottom) calculated during 48 hours before and after of each event at time t=0 for all events (a,d), events in which the remnant belt is created (b,e) and events with a pre-existing remnant belt (c,f). Red dashed lines correspond to the median value of the distributions.

For the outer radiation belts to enter a three-belt configuration, a combination of two different and in principle independent processes must occur. First, a remnant belt should be created, either abruptly as the result of a fast depletion of the fluxes at high L-shells, or through a slower process of erosion of the existing outer belt, that can occur in days to months. Second, a new “external outer" belt must form at higher L-shells following the depletion, but occurring in a region that does not overlap or significantly affect the dynamics of the already established remnant belt, so that the two populations can coexist. Oftentimes both processes occur as a consequence of a single geomagnetic disturbance, but it is also possible to have large time delays between the creation of the remnant belt and the appearance of the new outer belt. We are interested in the consequences of the process of formation of the remnant belt, as it has been proposed that the magnetopause location may play a role in the formation of remnant belts (*Mann et al.*, 2016, 2018). To do this, we have separated the events by the change in the location of the peak of the radiation belt fluxes. Events with a partial depletion leave behind a remnant belt that experiences a quick inward motion of the peak in flux, while events with a pre-existing remnant belt see no change (or minimal change) in the location of the peak in flux after the commencement of the relevant geomagnetic disturbance has occurred. We have chosen a threshold of $\Delta = 0.3L$ to determine if an event corresponds to the group of "pre-existing" remnant belt or "created" remnant belt as that particular number describe with relative accuracy what we visually observe in the data. Figure 5.2 presents a histogram of the magnetopause standoff minimum L values calculated within 48 hours of the start of each event and SYM-H minimum in the same time window. The left panels correspond to the distribution of values for all events, while the center and right panels correspond to the separation between events in which the remnant belt was created versus events in which the remnant belt can be considered pre-existing.

The SYM-H minimum distribution in Figure 5.2 (a) shows that three-belt events occur in a variety of weak to moderate geomagnetic storms, with a median value of the distribution of -61 nT. Here only one event occurs for SYM-H minimum significantly lower than -100 nT. If we separate the events we find that cases in which the remnant belt is created (b) present a higher SYM-H drop with a median value of -68 nT while pre-existing remnant belt cases tend to develop under weak (or no) storms, with a median value of -45 nT (c). This may reflect weak storms not being able to produce depletion of fluxes down to very low L shells, but still resulting in enhancements at higher L-shells. The estimated minimum location of the magnetopause results in a broad distribution (d) covering $5.0 < L < 8.1$ (median $L = 6.6$), the subset of events during which the remnant belts is created (e) can be generally associated with lower magnetopause standoff locations (median $L = 6.2$) than events with a pre-existing (f) remnant belt ($L = 7.0$), which is consistent with the idea of a magnetopause influence on the formation of the remnant belts.

Remnant belts tend to be observed in more energy channels than three-belts. One possible explanation is that since remnant belt creation and enhancement of the outer belt are different processes, it may be easier for a disturbance to remove those particles at high energies than it is to repopulate them in the outer region. Figure 5.3 (a) shows the observed occurrence of three-belt events as a function of the energy of the electrons. The occurrence rate increases with energy, peaks at E = 5.2 MeV, and then greatly decreases at higher energies. Figure 5.3 (b) shows the occurrence of remnant belts. Similar to the events with a three-belt structure, remnant belt occurrence also peaks at E = 5.2 MeV, however, remnant belt occurrence tends to remain higher at high energies when comparing to three-belt events. Figure 5.3 (c) shows the median location of the peak of the remnant belt (blue) for all events, as well as the upper and lower quartiles (red). The location of the remnant belt shows dependence on the energy of the particles, the median location decreasing in L-shell as the energy increases from L =3.9 for E =1.8 MeV to L =2.9 at E =7.6 MeV.

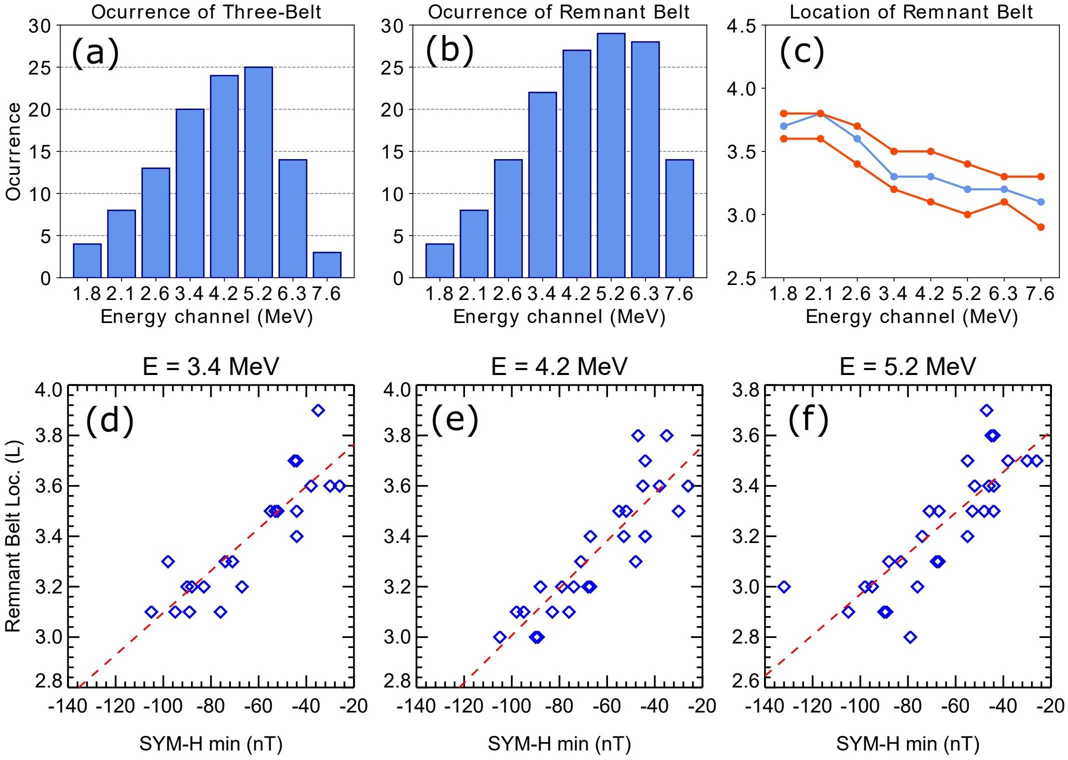

Figure 5.3: Top: observed occurrence frequency of three-belt events (a) and remnant belts (b) and peak location of remnant belts as a function of energy (c) with blue line corresponding to median value and red corresponding to quartiles. Bottom: relationship between SYM-H minimum and remnant belt peak location (L) for energy channels 3.4 MeV (d), 4.2 MeV (e) and 5.2 MeV (f). Red dashed line corresponds to the best linear fit for the trend.

We have also explored the dependence of the remnant belt location with respect to geomagnetic indices and found that SYM-H shows the best correlation with the location of remnant belts. Figure 5.3 (d-f) shows the SYM-H minimum versus the location of the remnant belt for all events for three different energy channels. The linear trend has been marked as a red dashed line, and the correlation coefficient of the linear trend has been calculated as 0.87 for E =3.4 MeV (d), 0.87 for $E = 4.2$ MeV (e) and 0.81 for $E = 5.2$ MeV (f). The location of the peak flux in the outer radiation belt after a storm is known to correlate with the SYM-H index (*Tverskaya et al.*, 2003; *Moya et al.*, 2017), but the correlation for the remnant belt is probably associated with the partial depletion of the belt at the beginning of the events.

5.4 On the persistence and decay of the remnant belt

Remnant belts can be very persistent. A strong geomagnetic storm could certainly destroy the remnant belt, but otherwise they naturally decay slowly as they appear to be relatively shielded from loss processes during moderate geomagnetic activity, in particular at high energies, therefore, the duration of a three-belt event depends principally on the ability of the external outer radiation belt to survive, which tends to decay relatively quickly. The duration of three-belt events in our list ranges from 5 to 17 days with an average duration of 11 days at E =4.2 MeV, while the duration of the remnant belts can be occasionally measured in months An example of a long-lasting remnant belt is shown in Figure 5.4. To estimate the lifetime of the remnant belts, we have calculated the decay rate assuming the electrons follow an exponential decay given by

$$f(t) = Ae^{-Bt},$$

where f corresponds to the electron flux measured in cm^{-2}sr^{-1}s^{-1} and A, B are the parameters to fit. To find the best fit, we first identified the peak flux location of every remnant belt for every energy channel and then performed a linear fit to the natural logarithm of the peak fluxes of the remnant belt. We have chosen the start time of the event at the vertical dashed line in Figures 5.1 and 5.5, which corresponds to the

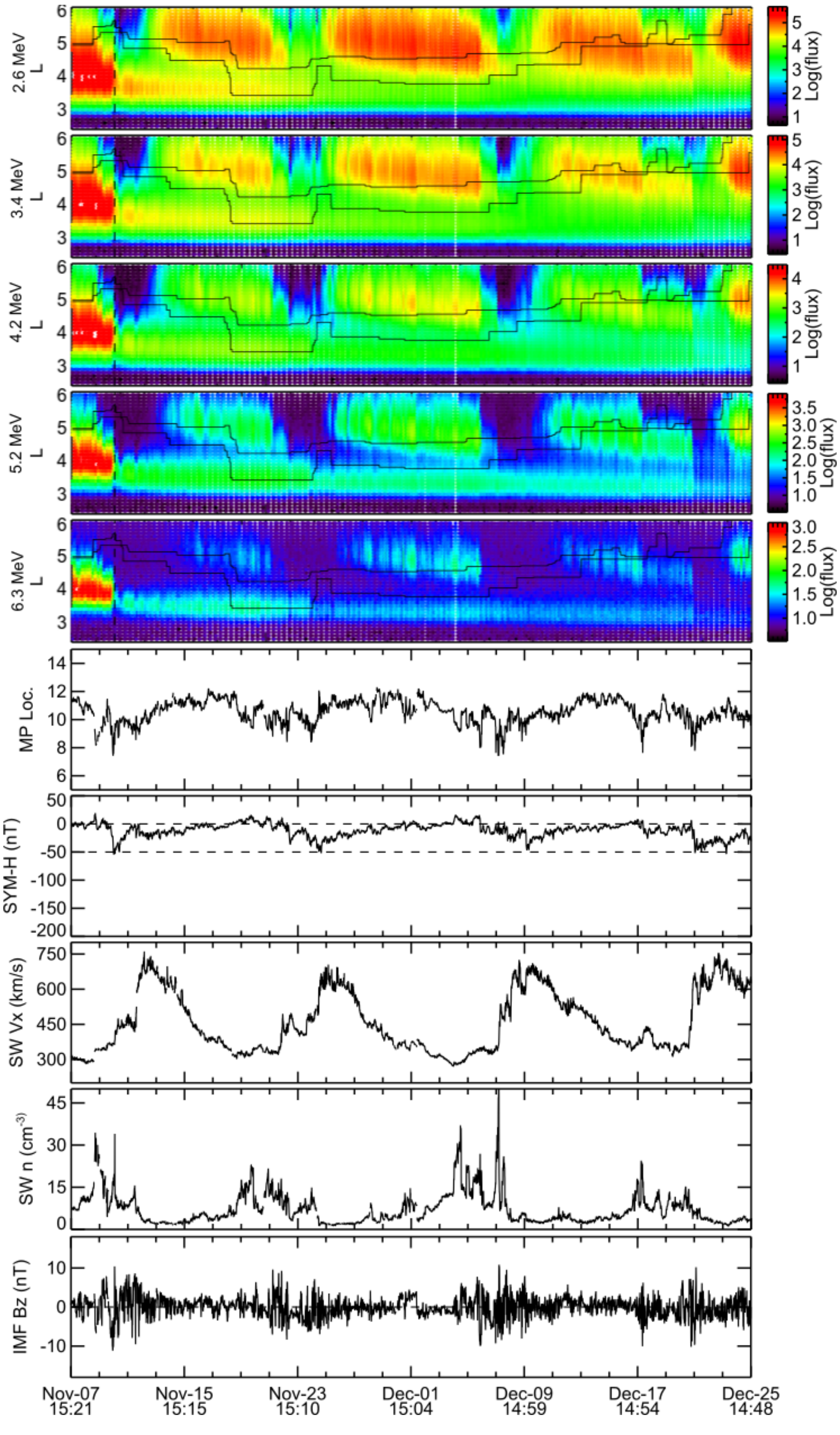

Figure 5.4: Example of a series of three-belt event associated with a persistent remnant belt that occurred between November and December 2016. From top to bottom: spin-averaged combined electron fluxes from Van Allen Probes as a function of L for energy channels 2.6 MeV, 3.4 MeV, 4.2 MeV, 5.2 MeV and 6.3 MeV. Bottom panels correspond to the estimated magnetopause standoff location, SYM-H index, solar wind speed V_x, solar wind proton density n, and IMF B_z.

minimum SYM-H value of the associated geomagnetic disturbance. Because we are interested in the natural decay rate of the remnant belt, we have excluded from the calculation the depletion associated with the start of the event, therefore the fitting must start after $t = 0$ (vertical dashed line). Figure 5.5 shows an example of the peak location of the remnant belt and the decay rate for two energy channels for the event shown in Figure 5.1 and for a second event that occurred on 10 November 2016. The upper panels show fluxes for two energies as a function of L and we have overplotted the remnant belt peak (black), the minimum of the external "slot" (white) region and the new external outer belt peak flux (blue). The peak electron fluxes of the remnant belt for the shown energy channels are shown below each plot along with the linear fit of the data (shown in red).

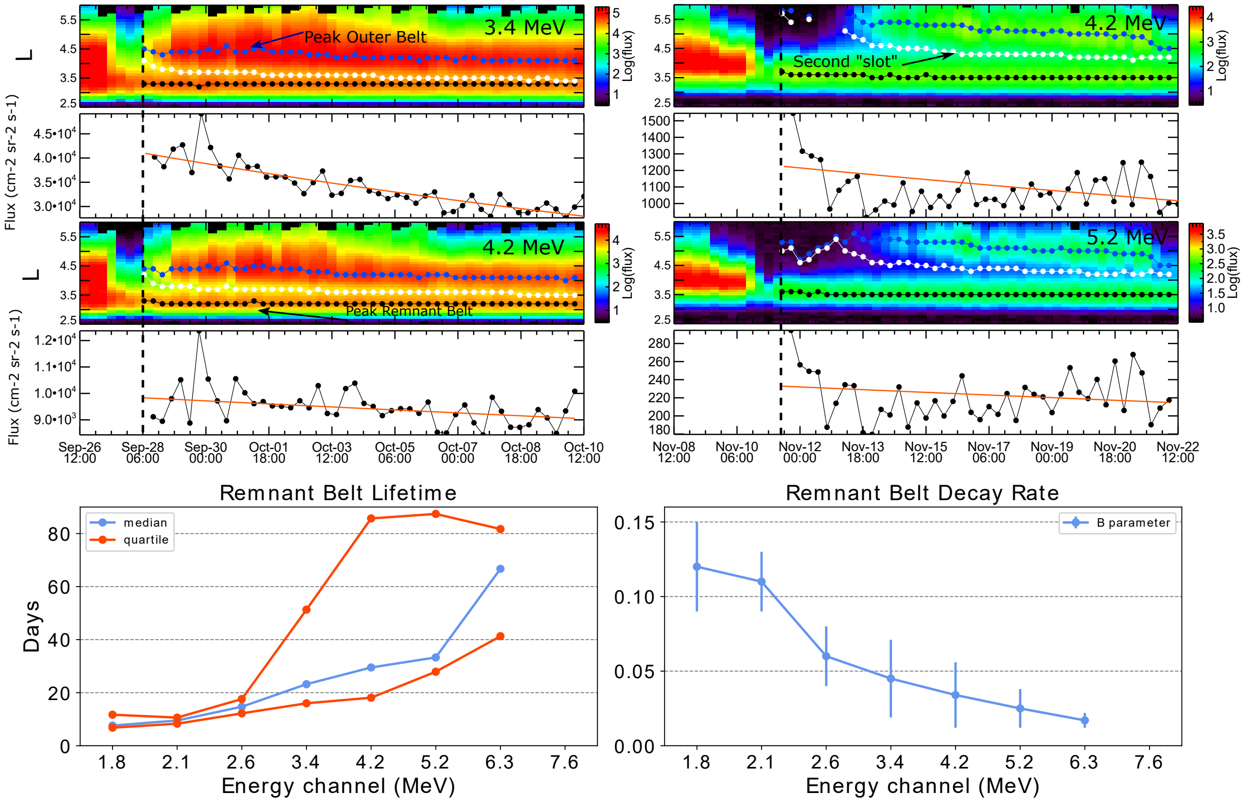

Figure 5.5: Location of the remnant belt (black dots), external slot (white dots) and outer belt peak flux (blue dots) for two events that occurred on 26 September 2017 (left) and 10 November 2016 (right) for two different energy channels. Below each plot there is a time series that show the flux values for the remnant belt peak and the best fit of the decay rate. Bottom panels correspond to the lifetime of the remnant belt as a function of energy for all events (left) and *B* parameter (right).

Table 5.1: Decay rates and lifetime of remnant belts as well as the number of events used for each energy channel to calculate the values

Energy	Events	B (days^{-1})	Lifetime (days)
E = 1.8 MeV	4	-0.12 ± 0.03	7.6
E = 2.1 MeV	8	-0.11 ± 0.02	9.5
E = 2.6 MeV	13	-0.06 ± 0.02	14.6
E = 3.4 MeV	20	-0.045 ± 0.026	23
E = 4.2 MeV	20	-0.034 ± 0.022	29
E = 5.2 MeV	14	-0.025 ± 0.013	33
E = 6.3 MeV	11	-0.017 ± 0.005	66
E = 7.6 MeV	0	-	-

To calculate the lifetime of the remnant belt, we have excluded fluxes that are too low $f < 25\,\mathrm{cm}^{-2}\mathrm{sr}^{-1}\mathrm{s}^{-1}$ as they approach the background noise level of the REPT instrument (*Claudepierre et al.*, 2015). We have also ignored those events that do not present a decay but rather a growth in flux. Events with growth rates in flux instead of decay tend to present very small growth, and can be due to fluctuations on the data associated with the location of the spacecraft, or acceleration processes that in fact supply particles to the remnant belt region, but these cases are beyond the scope of the present study. The values of the remnant belt lifetime and the parameters A and B for every energy channel are shown in Table 5.1. Individual fit parameters for every events are shown in Table 5.3. Figure 5.5 (bottom-left) shows the lifetime (in days) of the remnant belt calculated for different energy channels and the value of the fit parameter B (bottom-right). It can be seen that the lifetime of the remnant belt increases as a function of the energy, yet while the lower quartile and median values tend to present only moderate variation, there are a number of events in which the lifetime is very high especially at energies of 4.2 MeV and higher, indicating that in general, remnant belts are indeed very stable. We consider those values to be in agreement with previous studies that have evaluated the decay rates of the outer radiation belt (e.g. *Thorne et al.*, 2013b; *Drozdov et al.*, 2015).

5.5 Summary, discussion and conclusions

The discovery of the third radiation belt (*Baker et al.*, 2013a) has generated much interesting discussion about the possible causes leading to such a configuration, however, to date, there have been a limited number of events reported and no extensive statistical examination of such events. Here, we have identified 30 three-belt events, between September 2012 and November 2017. We have shown that around 18% of all geomagnetic storms during that period of time led to a remnant belt or three-belt structure, usually at energies between 3.4 MeV and 5.2 MeV making this a relatively common phenomena that can be statistically studied. The variety of geomagnetic conditions under which three-belt events can occur suggests that there may be more than one process responsible for the formation and evolution of three-belt events. In particular, the magnetopause location might have a stronger role in events that are "created" while pre-existing events may be the result of more natural long-term decay process occurring in the outer radiation belt. Although the same can be said about SYM-H minimum which more strongly correlates with the location of the remnant belts, the SYM-H effect seems to be general to all events, and therefore should be explored further. Although three-belt events occur more often during weak to moderate storms, they can also occur in association with high-speed streams that cause no storm.

As there is still relatively little known about three-belt events, we have tried to characterize them based on a number of parameters: the energy at which they appear, the conditions that lead to their formation and the boundaries that are thought to be important in their dynamics, such as the magnetopause location, in part motivated by early studies that present those parameter as being of possible importance. By calculating the decay rate of the remnant belt after it is formed we can conclude that while a three-belt event can vary between a few days to a few weeks depending on the particularities of each event and the energy of the electrons, remnant belts can exist in the radiation belts for months and possibly years given that no other strong storm removes them from existence. This is in agreement with *Thorne et al.* (2013b) suggestion that pitch-angle scattering with hiss waves is the responsible for decay of remnant belts. Of course, this assumes that the remnant belt is located inside the plasmasphere, and therefore shielded from other interactions, but an extensive study of the effects of the plasmapause in three-belt events is yet to be performed. Three belt events and remnant belts preferentially occur at energies between 3.4 MeV and 5.2 MeV, but there are a significant number of events outside that energy range, and therefore it seems to be an important topic for discussion if the mechanisms that favor formation of remnant belts at 1.8 MeV are the same that are dominating at 7.6 MeV.

Three-belt structures represent a unique configuration of the radiation belts which comes about as a consequence of a number of factors that deplete and enhance fluxes of energetic electrons in the radiation belts. The processes are in general energy-dependent and location specific, and as such, an important challenge is to understand and untangle the effects of the contributing mechanisms. This work is the first attempt to understand the characteristics of the events. For example, instead of using phase space density (to separate adiabatic from non adiabatic effects) we have chosen to use fluxes so our results can be more directly comparable to previous studies that also dealt with fluxes (e.g. *Baker et al.*, 2013a), and because our objective was to characterize and study the statistical behavior of the remnant belts. Phase space density studies will be required in order to unravel the relevant physical processes responsible for acceleration and losses leading to this particular configuration. Our results provide valuable insights about the characteristics of three-belt events, their relationship with geomagnetic boundaries and indices and contribute to the understanding of the response of the radiation belts to the effects of the solar wind.

Table 5.2: List of Three-Belt Events and their main characteristics: SYM-H minimum, the interplanetary driver, magnetopause minimum location, the range of energies and whether there was a pre-existing remnant belt or not

Date	SYM-H min. (nT)	Driver	MP loc. (L)	min E (MeV)	max E (MeV)	Pre-Existing
2012-09-05/07:43:00	-83	CME	5.7	3.4	5.2	No
2013-03-01/10:12:00	-76	HSS	6.8	3.4	5.2	No
2013-03-17/20:28:00	-132	CME	5.5	5.2	6.3	No
2013-04-24/18:11:00	-52	HSS	5.9	2.1	5.2	No
2013-05-01/19:10:00	-67	CME	8.1	4.2	6.3	No
2013-10-02/06:19:00	-90	CME	5.0	2.6	5.2	No
2013-11-09/08:14:00	-79	HSS	6.5	4.2	5.2	Yes
2015-04-16/23:29:00	-88	HSS	6.9	2.6	5.2	Yes
2015-05-13/06:59:00	-98	CME	6.1	2.6	4.2	Yes
2015-06-08/07:45:00	-105	HSS	7.2	3.4	5.2	No
2015-07-13/10:54:00	-71	CME	6.3	1.8	6.3	No
2015-11-30/11:32:00	-45	HSS*	6.7	1.8	2.1	Yes
2015-12-06/13:04:00	-26	HSS*	7.6	2.1	5.2	Yes
2016-01-20/16:42:00	-95	HSS	6.1	3.4	5.2	No
2016-06-06/06:47:00	-55	HSS	5.8	2.6	5.2	No
2016-07-12/10:11:00	-44	HSS*	7.2	3.4	6.3	Yes
2016-11-13/02:32:00	-30	HSS*	7.3	1.8	6.3	Yes
2016-11-25/06:38:00	-53	HSS	7.4	3.4	6.3	Yes
2016-12-09/19:09:00	-48	HSS*	6.9	4.2	6.3	No
2016-12-23/21:07:00	-55	HSS	7.2	5.2	6.3	No
2017-01-05/23:23:00	-47	HSS*	7.5	3.4	6.3	Yes
2017-05-20/08:11:00	-44	HSS*	7.1	2.1	3.4	Yes
2017-06-17/00:00:00	-38	HSS*	6.2	1.8	2.6	Yes
2017-07-16/15:51:00	-67	CME	6	2.6	6.3	No
2017-08-04/14:44:00	-35	HSS*	6.3	2.6	4.2	No
2017-08-20/03:35:00	-46	HSS*	7.1	5.2	6.3	Yes
2017-09-15/00:23:00	-44	HSS	6.0	1.8	7.6	Yes
2017-09-28/05:55:00	-74	HSS	6.0	2.6	6.3	No
2017-10-14/05:36:00	-68	HSS	7.0	4.2	7.6	No
2017-11-08/04:04:00	-89	HSS	6.1	3.4	7.6	No

*High speed streams that did not resulted in a SYM-H min lower than -50 nT

Table 5.3: List of single decay rates (*b* parameter) for all remnant belts according to the energy channel at which they appear. We have excluded from this list events whose parameter b is < 0 and flux $< 25\ \mathrm{cm}^{-}2\ \mathrm{s}^{-}1\ \mathrm{sr}^{-}1$

Event Date	1.8 MeV	2.1 MeV	2.6 MeV	3.4 MeV	4.2 MeV	5.2 MeV	6.3 MeV
2012-09-05/07:43:00				-0.0646	-0.0400	-0.0185	
2013-03-01/10:12:00				-0.031	-0.0234	-0.0115	
2013-03-17/20:28:00						-0.0318	
2013-04-24/18:11:00		-0.135	-0.0949	-0.0619	-0.0313		
2013-05-01/19:10:00					-0.0022		
2013-10-02/06:19:00							
2013-11-09/08:14:00							
2015-04-16/23:29:00			-0.0426	-0.0171			
2015-05-13/06:59:00			-0.0588	-0.012			
2015-06-08/07:45:00				-0.0951	-0.0678	-0.0442	
2015-07-13/10:54:00	-0.1295	-0.095	-0.056	-0.0202	-0.0034	-0.0046	
2015-11-30/11:32:00	-0.1510	-0.1239					
2015-12-06/13:04:00		-0.0936	-0.119	-0.0901	-0.058	-0.0332	
2016-01-20/16:42:00							
2016-06-06/06:47:00			-0.0698	-0.0435	-0.0283	-0.0112	
2016-07-12/10:11:00				-0.0593	-0.0504	-0.0302	-0.0149
2016-11-13/02:32:00	-0.0707	-0.056	-0.0315	-0.0051			
2016-11-25/06:38:00				-0.0114			
2016-12-09/19:09:00					-0.0137		
2016-12-23/21:07:00						-0.0002	
2017-01-05/23:23:00							
2017-05-20/08:11:00		-0.1053	-0.0834	-0.0481			
2017-06-17/00:00:00	-0.1321	-0.1041	-0.075914				
2017-07-16/15:51:00				-0.0796	-0.056919	-0.0386	-0.0122
2017-08-04/14:44:00			-0.0665	-0.0406	-0.010963		
2017-08-20/03:35:00						-0.0299	
2017-09-15/00:23:00		-0.1075	-0.0771	-0.0428	-0.0364	-0.0349	-0.0241
2017-09-28/05:55:00			-0.0601	-0.0323	-0.0069		
2017-10-14/05:36:00				-0.072	-0.0402		
2017-11-08/04:04:00			-0.0596	-0.0418	-0.0227		

CHAPTER 6

Decay of Ultrarelativistic Remnant Belt Electrons Through Scattering by Plasmaspheric Hiss

The material in this chapter has already been published in the *Journal of Geophysical Research: Space Physics* (*Pinto et al.*, 2019). Although the text it is presented in a similar form to the published work, my contribution is limited to the data analysis of ultrarelativistic electron remnant belts. The theoretical background to perform comparisons has been developed by Dr. Didier Mourenas, and the calculations of phase space density and wave intensity by Dr. Xiaojia Zhang and Dr. Anton Artemyev.

6.1 Introduction

One of the first results reported from the Van Allen Probes mission (*Mauk et al.*, 2013) was the appearance of a previously unreported triple-belt configuration of the Earth's radiation belt that included a storage ring of multi-MeV electrons located at $3.0 < L < 3.5$ in-between the inner belt and the re-populated outermost part of the outer belt (*Baker et al.*, 2013a). This configuration was very stable, as it lasted for a month before being wiped out by a new geomagnetic storm. In parallel to this first report, *Turner et al.* (2013) while studying the phase space density (PSD) evolution of equatorially mirroring electrons during storms using data from the THEMIS mission, encountered several of these transient three-belt configurations at relativistic energies. They suggested that this likely results from a partial depletion of the outer radiation belt at high L that leaves behind a remnant belt clearly separated from the re-forming outermost radiation belt, and that this phenomenon is relatively common. The processes potentially leading to the formation of a remnant belt have been discussed in various works (*Shprits et al.*, 2013, 2018; *Turner et al.*, 2013; *Thorne et al.*, 2013b; *Mann et al.*, 2016, 2018; *Yuan and Zong*, 2013b,a), but it still remains largely an open problem. Remnant belts can exist from hundreds of keV to multi-MeVs energies but they do not last a long time at lower energies, probably due to stronger hiss-induced scattering (*Thorne et al.*, 2013b; *Turner et al.*, 2013). Since they are formed at low $L < 3.5 - 4$, remnant belts of multi-MeV electrons should more likely appear very quickly following coronal mass ejection driven-storms than after disturbances associated with co-rotating interaction regions (e.g., *Yuan and Zong*, 2012). Recently, *Pinto et al.* (2018b) found that three-belt events, including a middle remnant belt of multi-MeV electrons are a relatively common occurrence with 30 such events occurring between 2012 and 2017, 25 of them showing a clear exponential decay of remnant belt electron fluxes. Such finding allowed a statistical characterization of remnant belts of multi-MeV electrons, demonstrating that they are more likely to occur at ultra-relativistic energies (3 to 5 MeV) but can sometimes be observed over the whole 1.8 MeV-7.6 MeV range, and that they are generally located in the region $3 < L < 4$. Their lifetime was found to increase as the energy of the electrons increase, from a few days at 1.8 MeV up to several months at energies of 6.3 MeV.

This increase in lifetime with energy raises the important question of what is the dominant mechanism of multi-MeV electron losses causing the decay of remnant belt electrons. The decay of one remnant belt formed at $L = 3.2$ following the September 2012 geomagnetic storm was studied by *Thorne et al.* (2013b) using two-dimensional Fokker-Planck simulations, showing that hiss waves were mainly controlling electron losses during this event. Plasmaspheric hiss waves are whistler-mode waves that typically occur in the 50 Hz to 2 kHz range, become more intense during active periods and have larger power on the dayside compared to the nightside (e.g., see *Li et al.*, 2015a; *Lyons and Thorne*, 1973; *Meredith et al.*, 2007; *Spasojevic et al.*, 2015, and references therein). They are thought to be partly generated locally by substorm-injected electrons (e.g.,see *Li et al.*, 2013; *Nakamura et al.*, 2016; *Su et al.*, 2018, and references therein) and partly amplified locally from a seed made of chorus waves initially generated outside the plasmasphere and having propagated inside it after reflection at high latitude (*Bortnik et al.*, 2008, 2009; *Meredith et al.*, 2013; *Agapitov et al.*, 2018). For electron energies smaller than ~ 2 MeV located at $L < 5$ inside the plasmasphere, the inner structure in energy and space of the radiation belts has been shown to be mainly controlled by electron loss due to cyclotron-resonant interaction with hiss waves and inward radial diffusion by ultra-low frequency (ULF) waves (or injections) from a source located in the outer belt or in the plasma sheet (e.g., see *Lyons and Thorne*, 1973; *Ma et al.*, 2015; *Mourenas et al.*, 2017; *Schulz and Lanzerotti*, 1974; *Thorne et al.*, 2013b), however, several recent studies have demonstrated that combined and synergistic electron scattering by hiss and electromagnetic ion cyclotron (EMIC) waves can often strongly increase ultra-relativistic (> 2 MeV) electron losses as compared with hiss waves alone around $L \sim 4 - 5$ within the plasmasphere (*Ma et al.*, 2015; *Mourenas et al.*, 2016, 2017; *Zhang et al.*, 2017). EMIC waves generated by anisotropic hot ion populations have indeed been observed in this region with significant occurrences and amplitudes, sometimes simultaneously with hiss waves at similar or different local times (*Meredith et al.*, 2014; *Zhang et al.*, 2016, 2017).

The relative importance of hiss and EMIC waves in controlling the observed decay rates of remnant belt ultra-relativistic electrons needs to be assessed statistically. The recent statistics of remnant belt events obtained by *Pinto et al.* (2018b) based on Van Allen Probes data represents an opportunity to address this problem in detail. In this study, we will use spin-averaged electron flux measurements from the Energetic Particle Composition and Thermal Plasma Suite (*Spence et al.*, 2013) Relativistic Electron Proton Telescope (ECT-REPT) (*Baker et al.*, 2013b) *on-board* the Van Allen Probes between 1.8 MeV and 6.3 MeV. The data from Van Allen Probes A and B were combined into a single grid of data points binned in space ($\delta L = 0.1$) and time ($\delta t = 6$ hours) by averaging all available data in each bin between 1 September 2012 and 30 November 2017. The processed data was then used to identify remnant belts and estimate their decay rates when fluxes were well above the background limit of the instrument ($f > 25$ cm^{-2} sr^{-1} s^{-1}) and the fluxes showed clear exponential decay (for more details, see *Moya et al.*, 2017; *Pinto et al.*, 2018b). In the next sections, we compare observed lifetimes of remnant belt ultra-relativistic electrons and analytical lifetime estimates (*Mourenas and Ripoll*, 2012; *Mourenas et al.*, 2017; *Zhang et al.*, 2017) for quasi-linear electron scattering by hiss waves (*Mourenas and Ripoll*, 2012; *Mourenas et al.*, 2017), or by hiss and EMIC waves (*Mourenas et al.*, 2016, 2017; *Zhang et al.*, 2017) based on recent wave statistics (*Li et al.*, 2015a; *Meredith et al.*, 2014; *Spasojevic et al.*, 2015; *Zhang et al.*, 2016). During some peculiar events, we examine electron phase space density (PSD) and simultaneous EMIC wave observations (*Kletzing et al.*, 2013) on board the Van Allen probes to estimate the relative importance of inward radial diffusion and EMIC waves on decay rates.

6.2 Comparisons between observed electron decay and theoretical estimates for hiss-induced loss

Repeated interactions between radiation belt electrons and broadband whistler-mode hiss waves of moderate average amplitudes $B_w < 50 - 100$ pT via cyclotron or Landau resonance usually produce a quasi-linear diffusion of the particles towards the region of smaller phase space density located in the loss-cone, leading to their precipitation into the atmosphere (e.g., see *Lyons and Thorne*, 1973; *Meredith et al.*, 2007; *Mourenas and Ripoll*, 2012). Combining analytical expressions of electron lifetimes τ inside the plasmasphere (*Mourenas and Ripoll*, 2012; *Artemyev et al.*, 2013; *Mourenas et al.*, 2016) with the most recent statistical models of plasmaspheric electron density (*Ozhogin et al.*, 2012) and the most recent statistical models hiss time-averaged intensity and frequency spectra (*Li et al.*, 2015a; *Agapitov et al.*, 2014; *Meredith et al.*, 2014; *Spasojevic et al.*, 2015), we can get a simple estimate of electron lifetimes in the presence of scattering by hiss only:

$$\tau \sim \frac{p^{3/2}\gamma L^2 \eta^{7/9}}{40\,\mathrm{Kp}\,\exp\left(-(L-3.2)^2/2\right)} \text{ [days]} \tag{6.1}$$

at sufficiently high electron energy

$$E > \left[\frac{\sqrt{1+10^3/(\eta L^5)}-1}{2}\right] \text{ [MeV]}$$

(*Mourenas et al.*, 2017) where p is the electron momentum normalized to $m_e c$ (with m_e the electron mass and c the velocity of light), γ the Lorentz factor, and η the actual plasmaspheric density normalized to the model density from *Ozhogin et al.* (2012). This analytical estimate of τ gives the physical scaling of τ with E, L, Kp, and normalized plasma density η. When Kp$\sim 1-2$, this analytical estimate of τ was checked to remain within a factor ~ 1.5 of full numerical lifetimes from 1 MeV up to at least 5 MeV(*Mourenas et al.*, 2017). The recent statistical hiss model from *Li et al.* (2015a) shows that peak hiss wave power occurs at relatively low frequencies $\sim 180-260$ Hz at $L = 3-4$, corresponding to a higher upper limit ~ 6.5 MeV of validity of the above analytical lifetime estimates than when considering older and more approximate hiss models that assumed a peak wave power frequency ~ 550 Hz (see *Mourenas and Ripoll*, 2012). In this simplified expression for τ, the MLT-averaged hiss intensity is assumed to vary approximately like $B_w^2 \sim$ Kp $\exp(-(L-3.2)^2/2)$ over $1.5 < L < 4.5$ and $0.5 <$ Kp < 5 based on hiss statistics (*Spasojevic et al.*, 2015; *Meredith et al.*, 2007; *Agapitov et al.*, 2014), with almost no variation with latitude up to 35° in agreement with satellite observations (*Artemyev et al.*, 2013).

The above theoretical lifetime estimates have already been well validated by comparisons with observations at energies $E < 1.8$ MeV over $1.5 < L < 5$ (*Mourenas et al.*, 2017). However, almost no comparison with measured lifetimes have been performed at higher electron energies $E > 1.8$ MeV for $L < 4.0$, due to the generally very low and noisy multi-MeV electron fluxes in that region (*Mourenas et al.*, 2017). The lifetimes recently obtained by *Pinto et al.* (2018b) in this low $L < 4$ region during remnant belt events provide a unique opportunity to check whether hiss waves alone are generally controlling the loss rate of ultra-relativistic electrons in that zone, or if other mechanisms also affect electron losses.

The presence of electromagnetic ion cyclotron (EMIC) waves (*Summers*, 2003; *Thorne and Kennel*, 1971) in addition to hiss waves may amplify electron losses at energies $E \geq 2$ MeV (e.g., see *Blum et al.*, 2015; *Li et al.*, 2007; *Mourenas et al.*, 2016; *Sandanger et al.*, 2007; *Usanova et al.*, 2014). Since helium-band EMIC waves with a frequency very close to the helium gyrofrequency are less frequent at $L < 4$ (*Zhang et al.*, 2016; *Kersten et al.*, 2014) and hot plasma effects limit their effectiveness for scattering ~MeV electrons (*Cao et al.*, 2017; *Chen et al.*, 2011; *Ni et al.*, 2018), one can only consider the hydrogen-band EMIC waves. Recent satellite statistics (*Zhang et al.*, 2016; *Kersten et al.*, 2014) show a statistical mean frequency ~ 0.4 times the proton gyrofrequency f_{cH}, a spectrum half-width $\sim 0.05 f_{cH}$, and MLT-averaged and time-averaged RMS amplitudes ~ 15 pT at $L = 3 - 4$ in a plasma with $\sim 90\%$ protons. Cyclotron resonance with EMIC waves is then available up to a maximum equatorial pitch-angle $\alpha_{\max} \sim \arccos(\min[1, 8/(\eta^{1/2}(L/2)^{1.4}E)])$ at energies $E > E_0 = 8/[\eta^{1/2}(L/2)^{1.4}]$ MeV. In this high energy and low pitch-angle domain, EMIC wave-induced pitch-angle diffusion is much faster than hiss diffusion (*Mourenas et al.*, 2016), representing an increased *effective* loss-cone and leading to a reduction of electron lifetimes that can be approximately modeled as $\tau_{(\text{with EMIC})} \sim \tau R_{\text{EMIC}}$, with $R_{\text{EMIC}} = (\cos^2\alpha^* + 2\ln(\sin\alpha^*))/[\cos^2\alpha_{\text{LC}} + 2\ln(\sin\alpha_{\text{LC}})]$ where $\alpha^* = \min[\max(\alpha_{\text{LC}}, \alpha_{\max}), 50^\circ]$ and α_{LC} is the drift loss-cone angle. As a result, there is usually a sudden decrease of lifetimes as energy increases above E_0, then an approximate plateau, before lifetimes resume their increase with E at higher energy (*Mourenas et al.*, 2016; *Zhang et al.*, 2016).

Figure 6.1 shows comparisons between observed lifetimes of decaying remnant belts (*Pinto et al.*, 2018b) and analytical electron lifetimes (*Mourenas et al.*, 2017) due to electron scattering by plasmaspheric hiss and by combined hiss and EMIC wave scattering (*Mourenas and Ripoll*, 2012; *Artemyev et al.*, 2013; *Mourenas et al.*, 2016), based on statistical models of plasmaspheric density (*Ozhogin et al.*, 2012), hiss intensity (*Spasojevic et al.*, 2015), and hiss frequency spectra (*Li et al.*, 2015a; *Agapitov et al.*, 2014; *Meredith et al.*, 2007). Four different relatively narrow (L, Kp) ranges are considered, such that the maximum error made in analytical lifetime estimates when using the mean L and Kp value in each range is at most ± 30%-40%. Since the standard deviation of plasmaspheric density in the statistical model from *Ozhogin et al.* (2012) is a factor ~ 1.5 about the nominal model density, the standard deviation of analytical lifetime estimates in Figure 6.1 is roughly a factor ~ 2 about the mean lifetime shown by a solid blue line. The corresponding minimum and maximum analytical lifetimes are marked by dotted blue lines in Figure 6.1.

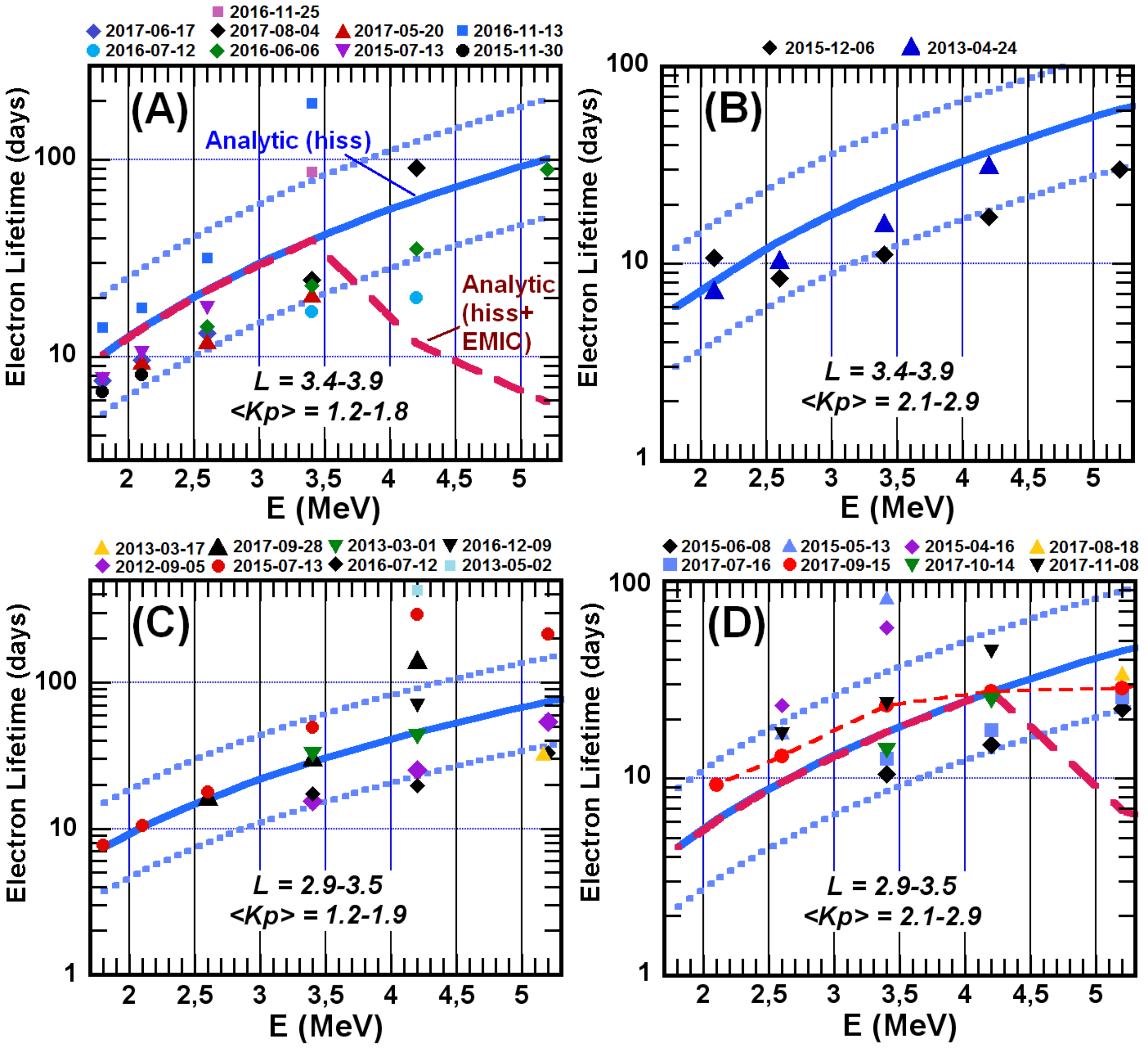

Figure 6.1: Lifetimes of remnant belt multi-MeV electron as a function of electron energy observed by the Van Allen Probes between 2012 and 2017. Estimated lifetimes during each remnant belt event correspond to a unique symbol-color combination (events starting dates are indicated at the top of each panel). The theoretical electron lifetime (*Mourenas et al.*, 2017) corresponding to electron scattering by plasmaspheric hiss alone is shown by a solid blue curve, with dotted blue curves indicating the standard deviation. The theoretical lifetime corresponding to combined scattering by hiss and typical hydrogen-band EMIC waves is shown by a red dashed curve. Panels show different L and time-averaged Kp ranges; (a) $3.4 \leq L \leq 3.9$ and $1.2 \leq \text{Kp} \leq 1.9$. (b) $3.4 \leq L \leq 3.9$ and $2.1 \leq \text{Kp} \leq 2.9$. (c) $2.9 \leq L \leq 3.5$ and $1.2 < \text{Kp} < 1.9$. (d) $2.9 \leq L \leq 3.5$ and $2.1 \leq \text{Kp} \leq 2.9$. The thin dashed red line in panel (d) corresponds to a single event that started on 2017-09-15.

Although the MLT-averaged hiss intensity can easily vary by a factor ~ 2 about its time-averaged modeled level at any given time (e.g., *Spasojevic et al.*, 2015; *Malaspina et al.*, 2016), it is worth noting that observed electron lifetimes are evaluated over $\sim 7-15$ days, which should generally correspond to time-averaged hiss intensity levels close to the time-averaged intensity of the statistical hiss model (which is based on several years of satellite measurements, but where each measurement is confined to a narrow MLT sector at any given time). Uncertainties of observed lifetimes inferred from measured electron flux decay over $\sim$ 10-day periods can be estimated as a factor $\sim$ 1.5 at most about the calculated value for relatively short lifetimes $<$ 40 days, with larger uncertainties for longer lifetimes.

The good agreement between observed and theoretical lifetimes τ in Figure 6.1 at all (L,Kp) ranges and at all electron energies from 1.8 MeV to 5.2 MeV demonstrates that the decay of remnant belts at $2.9 \leq L \leq 4.0$ within the plasmasphere is dominantly due to electron scattering by hiss waves (*Lyons and Thorne*, 1973; *Mourenas and Ripoll*, 2012; *Mourenas et al.*, 2017). Observed lifetimes are within a factor $\sim$ 1.5 of analytical estimates on average, and almost always within a factor of $\sim$ 2 – well within combined model and empirical uncertainties. This suggests that time-averaged hiss wave models (*Li et al.*, 2015a; *Spasojevic et al.*, 2015), the statistical plasmasphere density model from *Ozhogin et al.* (2012), and analytical lifetime estimates based on them can be used with relative confidence over timescales larger than 5-7 days, at least during not too disturbed periods when mean Kp$<$ 3 and the remnant belt remains well inside the plasmasphere. Comparisons with the analytical lifetime estimate $\tau_{\text{(with EMIC)}}$ (*Mourenas et al.*, 2016, 2017) taking into account the combined effects of EMIC and hiss wave scattering (see thick red dashed curves in Figure 6.1) suggest that EMIC waves probably do not play a role as important at energies 2 MeV $< E <$ 5 MeV and $L < 4$ during remnant belt events as they do at higher $L \geq 4$ for $E >$ 2.5 MeV (*Ma et al.*, 2015; *Mourenas et al.*, 2017; *Zhang et al.*, 2017). This is probably due to the lower statistical occurrence of hydrogen band EMIC waves at $L < 4$ (*Zhang et al.*, 2016).

Figure 6.2 further shows the measured electron lifetimes (normalized to their value at the minimum energy where lifetimes are available) versus $\gamma p^{3/2}$ normalized to its value at $E = 1.8$ MeV. Here, we only kept the 16 events with lifetimes available in at least 3 successive REPT energy channels starting at $E \leq 3.4$ MeV. Such events are expected to provide more accurate information on the scaling of lifetimes with energy than events for which lifetimes are available in only two energy channels, allowing for instance to detect an inflexion in the variation of lifetimes with energy. Also, when only two lifetimes are available, the lifetime at the highest energy is more likely to be over-estimated (since in the next, higher energy channel, the lifetime was too long to be measured or the electron flux was near noise level). The measured electron lifetimes were obtained at the L-shell of peak electron flux at each energy channel during a given remnant belt event, corresponding to a very slight decrease of L by $\Delta L \simeq 0.1$ to 0.3 as energy increases. Now, if observed lifetimes only result from quasi-linear electron pitch-angle scattering by the sole hiss waves, they should increase monotonously with electron energy like the theoretical scaling $\tau \sim \gamma p^{3/2}$ (dotted black line) at energies above 1.8 MeV (*Mourenas and Ripoll*, 2012; *Artemyev et al.*, 2013; *Mourenas et al.*, 2017). In contrast, if other physical mechanisms such as EMIC wave-induced scattering or inward radial diffusion are sometimes affecting the decay of the remnant belts, a significant deviation from the theoretical hiss scaling should appear in Figure 6.2, in the form of a localized decrease or plateau of lifetimes as $\gamma p^{3/2}$ increases during a given event (*Mourenas et al.*, 2016, 2017; *Zhang et al.*, 2017).

For the 13 events displayed in Figure 6.2(a) there is a close agreement between the scaling of measured lifetimes with energy and the theoretical scaling $\tau \sim \gamma p^{3/2}$ (dotted black line). The very slight decrease of many observed lifetimes below the theoretical scaling at higher $\gamma p^{3/2}$ (i.e., higher energy) may be partly due to a slight reduction of the measurement L-shell by $\Delta L \simeq 0.1 - 0.3$ as energy increases (unaccounted for in the theoretical scaling) that can sometimes decrease the theoretical τ by 10%-30%. Still, discrepancies between theoretical and observed scaling remain within empirical lifetime uncertainties of about ±30%-40%. Occasionally, the measured lifetime at the highest energy can be sensibly larger than theoretical expectations, as seen during one event (2016-11-13) at 3.4 MeV – but this is probably due to a too low and noisy electron flux at

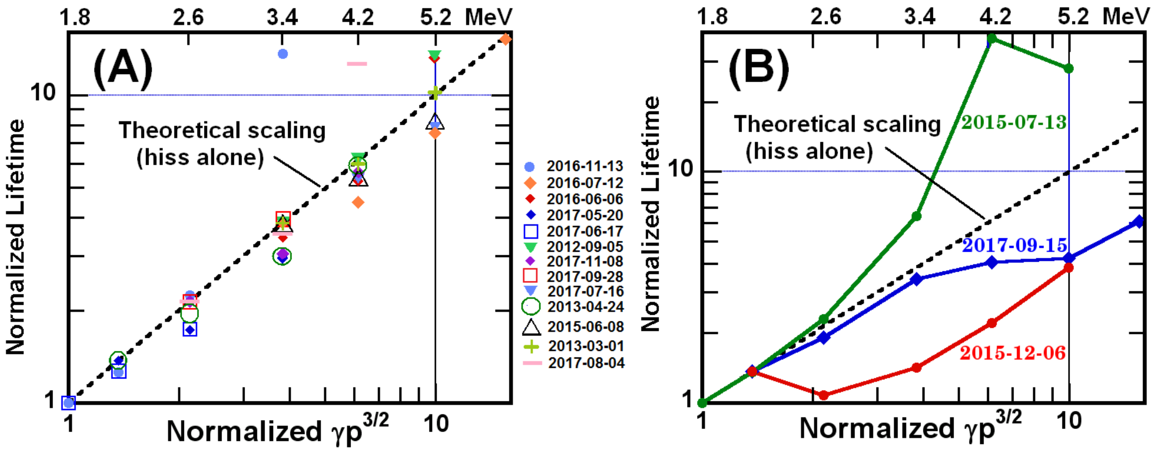

Figure 6.2: Normalized lifetimes of remnant multi-MeV electron belts observed by the Van Allen Probes between 2012 and 2017 as a function of the theoretical energy scaling $\gamma p^{3/2}$ normalized to its value at 1.8 MeV. Measured lifetimes during each remnant belt event correspond to a unique symbol-color combination. The theoretical scaling for scattering by hiss alone is denoted by a dotted black line. Only events having at least 3 lifetimes in consecutive REPT energy channels available are displayed: (a) the most usual behavior, such that lifetimes monotonically increase with energy (events starting dates are indicated on the right-hand-side of the panel); (b) Three anomalous events with some significant lifetime decrease or plateau, starting on 2015-12-06 (red curve), 2017-09-15 (blue curve), and 2015-07-13 (green curve).

high energies during such events: the uncertainty on such long > 100 days lifetimes can become larger than a factor 2.

In contrast with events in Figure 6.2(a), a significant departure of the observed lifetimes from the theoretical scaling for hiss scattering alone (dotted black line) is found during 3 events at $3.2 < L < 3.8$ as shown in Figure 6.2(b). During the 13 July 2015 event, measured lifetimes are higher than hiss-only lifetimes and the reduction only occurs for very long lifetimes $\sim 200-300$ days (see corresponding red circles in Figure 6.1(c)) that already lie above the theoretical scaling that was well followed at lower energy < 3 MeV. In such a case, the uncertainty on measured lifetimes is larger than a factor 2, sufficient to account for the apparent lifetime increase at $E = 4.3$ MeV and then reduction at $E = 5.2$ MeV. During the two other events, however, the measured reduced lifetimes are shorter (< 28 days and < 11 days, respectively – see thin red dashed curve in Figure 6.1(d) for the 2017-09-15 event and black diamonds in Figure 6.1(b) for the 2015-12-06 event) and therefore accurate within $\sim \pm 30\%$. The plateau in lifetimes found during these two events therefore signals the likely presence of some additional effect. It may consist of either an additional electron loss mechanism reducing lifetimes at higher energy, such as scattering by EMIC waves in combination with hiss waves (*Li et al.*, 2007; *Mourenas et al.*, 2016), or in an additional electron replenishment mechanism increasing lifetimes at lower energies, such as inward radial diffusion by ULF waves at fixed first adiabatic invariant $\mu = p_{\perp}^2/2m_e B$, with m_e the electron mass and B the geomagnetic field strength.

During the 6 December 2015 event, geomagnetic activity was significant, $\langle \mathrm{Kp} \rangle \sim 2.7$ and the remnant belt at $E = 2.1$ MeV was at a relatively high $L = 3.8$. In such circumstances, the plateau in lifetimes at 2.1 MeV $\leq E \leq$ 3.4 MeV could have resulted from a strong inward radial diffusion of electrons, that could partly compensate for losses due to hiss waves (e.g., *Mourenas et al.*, 2017; *Schulz and Lanzerotti*, 1974). Such a strong inward radial diffusion would require the presence of a significant positive outward gradient of electron phase space density (PSD) just above $L^* = 3.8$ at constant first adiabatic invariant μ and $E \sim 2.1 - 2.5$ MeV. However, Figures 6.3(a),(b) show that there is no such monotonic outward increase of the electron PSD over $3.8 \leq L^* \leq 4.1$ at the corresponding $\mu \approx 1000 - 2000$ MeV/G during the start of this event on 6 December 2015 – instead, there is a small PSD peak at invariant drift shell $L^* \simeq 3.8$ (corresponding to the remnant belt position) followed by a relative minimum at $L^* \simeq 4.0 - 4.2$, or simply a plateau over $3.8 \leq L^* \leq 4.1$. The strong PSD peak present at higher L^*-shells corresponds to the outer belt.

During the 15 September 2017 event, geomagnetic activity was moderate $\langle \mathrm{Kp} \rangle \sim 2.1$ and the remnant belt peak flux was at lower $L \simeq 3.4$. A plateau in lifetimes occurred at 3.4-5.2 MeV. A partial replenishment of electron flux at $\sim 2 - 4$ MeV by radial diffusion might be able to explain such a plateau. However, this would require a net positive outward gradient of the electron PSD at constant first adiabatic invariant over $L = 3.5 - 3.8$ at $2 - 4$ MeV as well as a significantly stronger ULF wave intensity than statistical averages at such low L-shells and low Kp (*Ozeke et al.*, 2014; *Mourenas et al.*, 2017). Actually, Figures 6.3(c),(d) show that there is no monotonous outward increase of the PSD at the corresponding $\mu \sim 1000 - 3000$ MeV/G over $L^* = 3.5 - 3.8$, but rather a minimum at $L^* \simeq 3.8$ for electrons with pitch-angle $\sim 45°$ ($K = 0.2$) and a PSD plateau over $L^* \sim 3.5 - 3.8$ for nearly equatorially mirroring electrons ($K = 0.03$).

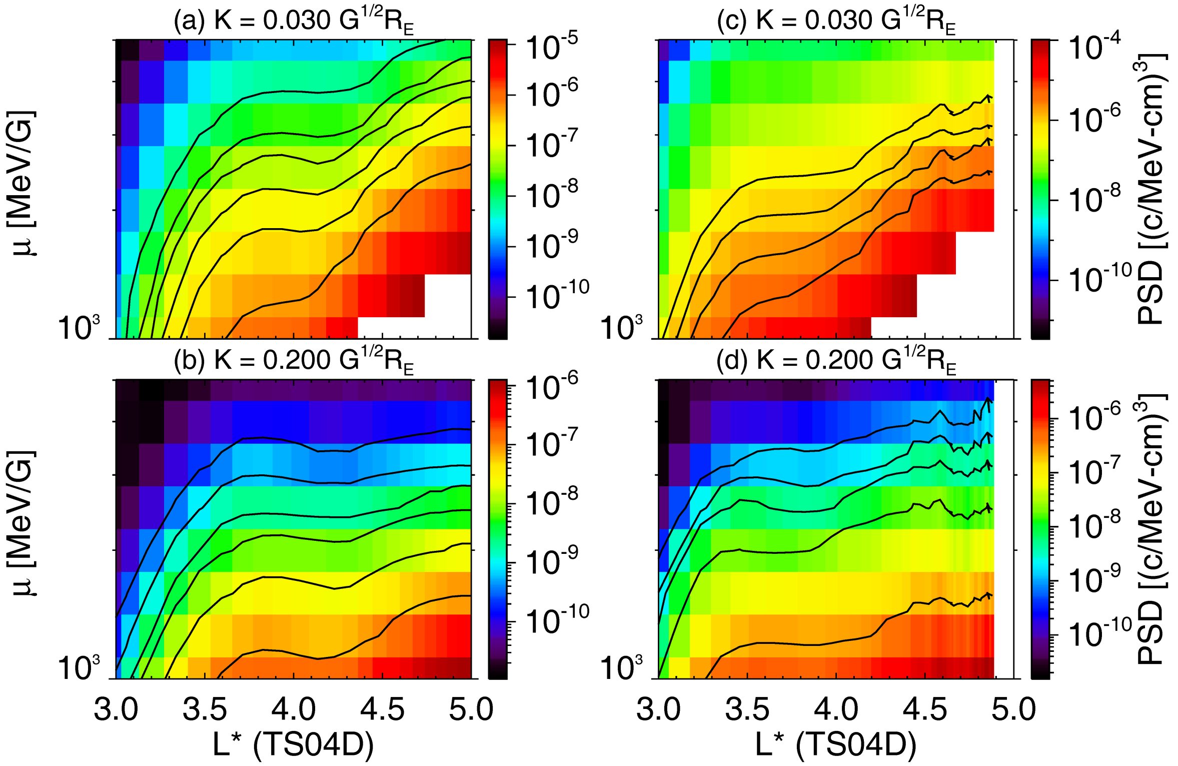

Figure 6.3: Electron phase space density (PSD) from the REPT instrument onboard the Van Allen Probes as a function of first adiabatic invariant μ and L^*. (a,b) Electron PSD for second adiabatic invariant $K = 0.03\,G^{1/2}R_E$ and $K = 0.2\,G^{1/2}R_E$ electrons on 2015-12-06 over 16:50-20:40 UT from RBSP-A. (c,d) Electron PSD for $K = 0.03\,G^{1/2}R_E$ and $K = 0.2\,G^{1/2}R_E$ electrons on 2017-09-15 over 6:25 to 10:20 UT from RBSP-B. Contour lines at the same PSD level are shown in black.

The above results suggest the absence of significant inward radial diffusion in the two events of 06 December 2015 and 15 September 2017. The plasmapause location L_{pp} has been calculated from the formula $N_e(L_{pp}) = \max(50, 10(6.6/L_{pp})^4)$ cm^{-3} (e.g., see *Li et al.*, 2015a) over the two corresponding intervals of electron flux decay, based on plasma density N_e measurements from the Van Allen Probes. During the flux decay period with $\langle \mathrm{Kp} \rangle \sim 2.1$ starting on 15 September 2017, the plasmapause remained at $L > 3.6$ nearly all the time (mostly at $L > 4.5$), that is, well above the remnant belt location at $L = 3.4$. During the especially disturbed period with $\langle \mathrm{Kp} \rangle \sim 2.7$ starting on 06 December 2015, the plasmapause still remained above the remnant belt location (at $L = 3.8$) approximately $\sim 75\%$ of the time. Although the plasmapause sometimes decreased in this case to $L \sim 3.2$ near 12 MLT, it is generally $\sim 0.5 - 1$ Earth radii higher from 15 MLT through midnight to 9 MLT than near 12 MLT (*O'Brien and Moldwin*, 2003). Accordingly, the remnant belt was probably inside the plasmasphere during most of this 06 December 2015 event as well. This leaves only the additional presence of EMIC waves as a possible explanation for the creation of a plateau in lifetimes as a function of E during two of the three events in Figure 6.2(b). EMIC waves may therefore contribute with hiss waves to multi-MeV electron loss at $3.0 \leq L < 3.9$ in about 10-15% of remnant belt events.

6.3 Combined effects of hiss and EMIC waves on multi-MeV electrons during the 15 September 2017 remnant belt decay event

We now investigate in more detail the peculiar decay of the 15 September 2017 remnant belt event discussed in the previous section. The profile of electron lifetimes measured during this event at $L \simeq 3.4$, displayed in Figure 6.2(b) (blue curve), shows an initial increase of lifetimes with energy in agreement with hiss-induced loss, then a plateau between 3.4 and 5.2 MeV, before lifetimes increase again above 5.2 MeV. The comparison in Figure 6.1(d) of measured lifetimes (thin red dashed curve) with theoretical lifetimes in the presence of hiss waves alone (blue curve) and with hiss waves plus a statistical model of hydrogen band EMIC waves (thick dashed red curve) shows lifetimes in-between the hiss-alone and hiss-plus-EMIC theoretical lifetimes. This suggests that EMIC waves were probably present but with a lower occurrence rate or time-averaged intensity than in the assumed model. Indeed, the plateau in measured lifetimes starts at roughly the same energy ($\sim$ 4 MeV) where the hiss-plus-EMIC theoretical lifetimes start to depart from hiss-only lifetimes. The hydrogen band EMIC wave model used in Figure 6.1(d) assumed approximate MLT-averaged and time-averaged RMS amplitudes $\sim$ 15 pT and a upper frequency cutoff at $\sim 0.45 f_{cH}$, based on years of wave statistics over $3 < L < 4$ (*Mourenas et al.*, 2017; *Zhang et al.*, 2016).

We have examined Van Allen Probes observations of EMIC waves between 15 and 25 September 2017 to check whether measured EMIC waves actually possessed the characteristics (hydrogen band waves, relatively high upper frequency cutoff, weak time-averaged amplitudes) that could explain the peculiar profile of electron lifetimes during this specific event. We have found that intense EMIC waves were recorded on two occasions at $L \simeq 3.4$ by the Van Allen Probes, both times in the hydrogen band. The strongest hydrogen band EMIC waves had a time-averaged RMS amplitude $B_w = 350$ pT over nearly 5 minutes on 18 September, with mean and upper-cutoff frequencies ~ 0.73 and 0.77 f_{cH} as shown in Figure 6.4(a) (black line). There was a second observation of hydrogen band EMIC waves over 25 minutes on 20 September, with RMS amplitudes $B_w = 120$ pT, mean and upper-cutoff frequencies ~ 0.37 and 0.42 f_{cH} (see Figure 6.4(a) red line). Both EMIC waves had small wave-normal angles $< 10^\circ$ and were observed at geomagnetic latitudes $\sim 4^\circ$ and 14° near 9-10 MLT. In addition, a weak burst of helium band EMIC waves with RMS amplitude $B_w \sim 150$ pT was observed, but these waves had a too low upper frequency cutoff (about 0.77 times the helium gyrofrequency) to interact via cyclotron resonance with electrons of energy < 6 MeV at $L = 3.4$ (*Kersten et al.*, 2014; *Summers*, 2003).

Therefore, it appears that EMIC waves measured during this event possess at least two of the needed characteristics to account for the observed lifetimes: they were observed in the hydrogen band and had a relatively high upper frequency cutoff $> 0.4 f_{cH}$. It is impossible, however, to infer their MLT-averaged and time-averaged amplitudes from available measurements during this event due to the limitation of the orbital coverage of the Van Allen Probes to narrow local time domains near 9 MLT and 16 MLT at $L = 3.4$ for the duration of the event. Consequently, we had to rely on past statistics of hydrogen band EMIC wave occurrence and intensity as a function of AE or AL indices near $L = 3.4$. Between 16 and 24 September 2017 (included), the daily AE and AL had mean values of 240 nT and -170 nT, respectively. For such moderate geomagnetic activity, CRRES statistics of hydrogen band EMIC waves at $L \sim 3.5$ show occurrence rates of about 1% confined to two MLT regions at 9-10 MLT and 21-22 MLT, with time-averaged

RMS amplitudes of roughly 20 pT inside these zones (see Figures 7 and 10 from *Meredith et al.*, 2014), while Van Allen Probes statistics show $\approx 0.5\%$ occurrence rates at 10-11 MLT and 15-16 MLT, with (non-time-averaged) RMS amplitudes of measured waves of about 450 pT in these zones (see Figure 2 from *Zhang et al.*, 2016).

Interestingly, both CRRES and Van Allen Probes statistics show that the 10 MLT region is one of the few narrow MLT regions of significant occurrences of hydrogen band EMIC wave at $L \sim 3.4$. Since this MLT zone was relatively well-covered by the Van Allen Probes during the considered event, the observed EMIC wave spectra are likely representative of actual wave spectra over the duration of this event. However, other bursts of hydrogen band EMIC waves were probably present near 10 MLT or 15 MLT at other universal times, when the Van Allen Probes were not crossing the $L \sim 3.4$ region to measure them. In the following, we therefore assume that the total MLT- and time-averaged intensity of EMIC waves was close to their statistical level, corresponding to a RMS amplitude ~ 9 pT (*Zhang et al.*, 2016), using time-averaged spectra obtained from the Van Allen Probes during the considered event (see Figure 6.4a) – that is, we consider EMIC waves with upper frequency cutoff $\sim 0.77 f_{cH}$ and RMS amplitude 7 pT together with waves with upper frequency cutoff $\sim 0.42 f_{cH}$ and RMS amplitude of 6 pT.

In addition, over the 9-10 days of the event duration, it is reasonable to assume that the MLT-averaged and time-averaged hiss waves can be well represented by their statistical spectra (*Li et al.*, 2015a; *Spasojevic et al.*, 2015) at $L = 3.4$ when Kp$\sim$ 2.1, with a peak of magnetic power of about 1300 pT^2 at a mean frequency of 200 Hz. During this event, the time-averaged plasma density inferred from upper-hybrid line measurements on-board the Van Allen Probes was $\langle N_e \rangle \sim 700 \pm 160$ cm^{-3} at $L = 3.4$. The corresponding measured electron plasma frequency to gyrofrequency ratio $F_{pe}/F_{ce} \simeq 10.8$ is therefore very close to the ratio $F_{pe}/F_{ce} \simeq 5(L/2)^{1.4} \sim 10.51$ expected from the statistical plasmaspheric density model of *Ozhogin et al.* (2012) used in analytical lifetime estimates (*Mourenas et al.*, 2017, Figures 1-2).

Figure 6.4(b) shows the measured lifetimes during this event, compared with numerically calculated lifetimes corresponding to quasi-linear diffusion by combined hiss

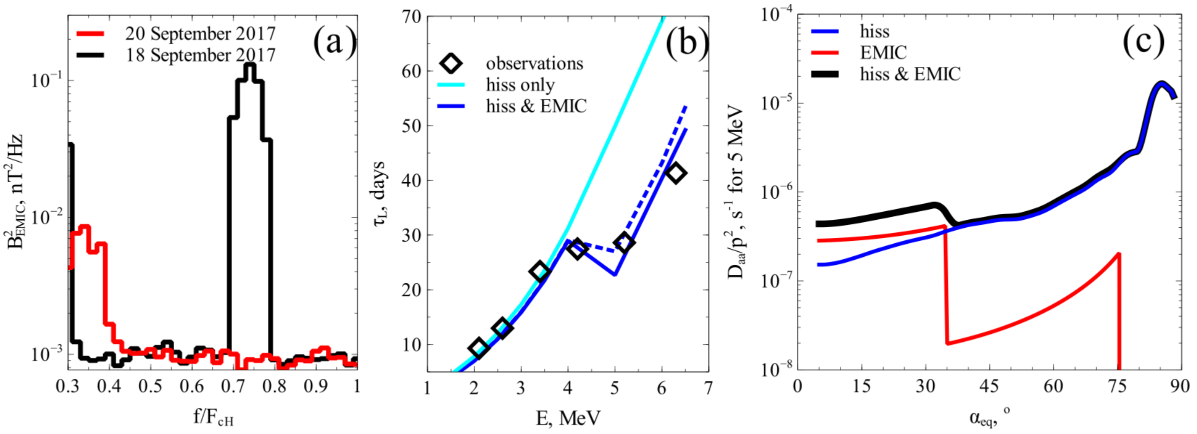

Figure 6.4: (a) EMIC wave spectra in the hydrogen band observed by the Van Allen Probes on 18 and 20 September 2017 at $L \sim 3.4$. (b) Observed lifetimes as a function of electron energy E at $L \simeq 3.4$ during the 15-25 September 2017 event (black diamonds), together with corresponding numerically calculated lifetimes based on quasi-linear pitch-angle scattering by hiss waves alone (cyan) or hiss and EMIC waves (blue), considering a statistical model of hiss intensity and spectrum (*Li et al.*, 2015a; *Spasojevic et al.*, 2015), a statistical model of EMIC wave intensity (*Zhang et al.*, 2016), measured EMIC wave frequency spectra during this event, and a plasma consisting of ~85% protons (solid blue curve) or 90% protons (dashed blue curve) during this disturbed period (*Kersten et al.*, 2014; *Summers*, 2003). (c) Electron quasi-linear pitch-angle diffusion rates by hiss (blue) and EMIC (red) waves at 5 MeV and $L = 3.4$ in a plasma consisting of ~85% protons. The total diffusion rate obtained by summing hiss and EMIC wave-induced diffusion rates is shown in black.

and EMIC waves. Numerical calculations were needed here, because the simple analytical lifetime estimates used in the previous section assume that, when EMIC waves are present, pitch-angle diffusion due to hiss waves is negligible as compared with diffusion due to EMIC waves at small equatorial pitch-angles, which is not anymore justified for the very low amplitude EMIC waves considered in the present case. Accordingly, lifetimes were evaluated as the integral over α between the drift loss-cone angle α_{LC} and 85° of $1/[2\tan(\alpha)\,D_{\alpha\alpha}(\alpha)]$ with $D_{\alpha\alpha}$ the total quasi-linear pitch-angle diffusion rate (*Albert and Shprits*, 2009; *Mourenas et al.*, 2016). The good agreement between measured and numerical lifetimes in Figure 6.4(b) shows that adding the observed EMIC waves together with hiss waves can indeed accurately reproduce the observed plateau in lifetimes between $3.5 < E < 5$ MeV, which would have been absent without them (compare blue and cyan curves in Figure 6.4(b)). The numerically calculated quasi-linear pitch-angle diffusion rates, displayed in Figure 6.4(c) further demonstrate that the additional EMIC waves, despite their weak time-averaged intensity, remain sufficiently strong to visibly increase 5 MeV electron diffusion at small equatorial pitch-angles, where the effect on lifetimes is maximal (*Albert and Shprits*, 2009; *Mourenas et al.*, 2016).

During this disturbed period, the plasma is assumed in Figures 6.4(b,c) to consist of approximately $\sim$85% protons based on previous estimates during observations of hydrogen band EMIC waves (*Kersten et al.*, 2014; *Summers*, 2003). Varying the proton fraction between 85% and 90% only slightly modifies electron lifetimes below 6 MeV (compare solid and dashed blue curves in Figure 6.4(b); see also analytical estimates from *Mourenas et al.* (2016)).

It is worth noting that ultra-relativistic electron lifetimes remain large during each EMIC wave burst period due to the strong localization in MLT of these waves, their moderate time-averaged intensity, and the fact that only small pitch-angle electrons are scattered by them – letting hiss waves alone first scatter higher pitch-angle electrons toward this region of small pitch-angles where, in turn, EMIC waves can ultimately precipitate them into the atmosphere. As a result, the effect of EMIC wave bursts on lifetimes measured by the Van Allen Probes with a roughly 6-hour time step is only gradual, and it becomes smoothed out over several days of measurements, explaining the absence of flux decreases (or dropouts) localized in time in the present observations.

6.4 Conclusions

Radiation belt electron remnant belts are often observed at $3 < L < 4$ in the aftermath of geomagnetic disturbances, located in-between the relatively steady inner belt and a freshly re-forming outer belt. In the present Chapter, we statistically investigated the role played by plasmaspheric hiss and EMIC waves in controlling the observed decay rates of remnant belt ultra-relativistic electrons inside the plasmasphere during 25 remnant belt events that occurred between September 2012 and November 2017. The absolute value of the observed decay rates, as well as their scaling with electron energy, were shown to be in good agreement (within uncertainty ranges) with analytical expressions of ultra-relativistic electron lifetimes, calculated for hiss-induced loss based on statistical models of hiss and plasmaspheric density.

During a few particular events, however, a deviation of measured electron lifetimes from the theoretical scaling became apparent over a certain energy range. A close examination of electron PSD maps at $3 < L < 5$ has shown that such a behavior apparently cannot be related to inward radial diffusion. During at least one of these particular events, we found that simultaneously observed EMIC waves in the hydrogen band could sufficiently increase the rate of electron scattering at low pitch-angles as compared with hiss alone, to account for the observations despite their very small MLT-averaged and time-averaged intensity of only ≈ 9 pT. The effect of EMIC waves was only to decrease lifetimes by a factor ~ 2. Such an effect is, therefore, difficult to identify with confidence at a given electron energy, due to the uncertainty inherent in measuring actual hiss intensity and plasma density levels at a given time. However, the effect of EMIC waves of such very weak time-averaged intensity can be much more easily discerned in lifetime profiles as a function of energy, because this effect should be localized in energy just above the minimum energy threshold for cyclotron resonance with multi-MeV electrons. Our limited statistics of events suggests that only about 10-15% of remnant belt events at $L < 4$ are probably affected by such EMIC wave-driven precipitation losses.

Several studies have indicated that the most intense plasmaspheric hiss can sometimes be composed of short ($\sim 3 - 5$ wave periods) quasi-coherent wave-packets that may lead to non-linear effects in addition to the quasi-linear diffusion by relatively incoherent hiss considered here (e.g., *Nakamura et al.*, 2016; *Tsurutani et al.*, 2018). In reality, however, non-linear electron interactions with such short hiss packets can still lead to loss rates similar to quasi-linear diffusion, provided that such intense but short wave-packets are sufficiently rare or spread in time over periods of weeks when $Kp < 3$ (e.g., *Mourenas et al.*, 2018), and hence most probably do not affect the findings of the present study.

CHAPTER 7

Summary, Conclusions and Future Work

This dissertation explored various aspects of the relationship between the solar wind and the dynamics of the Earth's Van Allen radiation belts. We first studied the response of relativistic and ultra-relativistic electrons to solar wind and geomagnetic disturbances, in particular those that resulted in enhancement or depletion of fluxes throughout the outer radiation belt, but starting from events occurring at geostationary orbit. We investigated the solar wind parameters that were good candidates to explain the response of the outer belt relativistic electrons and attempted a simple prediction of relativistic electron enhancement events. We also quantified the penetration of enhancements to lower altitudes and the degree of correlation of outer radiation belt fluxes at different $L-$shells with fluxes at geostationary orbit to understand the limits and characteristics of the outer belt cohesive response. In the second part of the dissertation, we explored the newly discovered phenomenon of remnant belts associated with a triple-belt configuration of the Earth's radiation belt with the idea of determining their occurrence rate, and under which conditions they are likely to be formed, at what energies they occur, where are they generally located, how long they last and what their most likely formation mechanisms might be.

In Chapter 3, we identified relativistic electron enhancement events and persistent depletion events during a complete solar cycle, from 1996 to 2006 and performed a superposed epoch analysis to characterize the solar wind parameters necessary and/or favorable to their occurrence. We did this by searching for events regardless of whether they were storm-time events or not. By doing this we found that, despite the fact that most events were associated with some type of geomagnetic disturbance, (CME or CIR) around 30% of them were considered non storm time (i.e. minimum SYM-H > -50), which reinforces the idea that storms are not necessary for enhancement events or persistent depletions to occur (e.g. *Kim et al.*, 2015). We found that a sustained and elevated AE index is fundamental for enhancements to occur, consistent with previous studies (e.g *Kim et al.*, 2015; *Hajra et al.*, 2015) but that significant differences in the solar wind profiles between enhancement and persistent depletion events allowed us to establish a set of threshold values for enhancement events that were favorable for their occurrence. In particular, most enhancement events occur with solar wind speeds $V_x > 520$ km/s and cumulative southward directed IMF $B_z > 120$ nT·hour (on a 1 minute time resolution). Most importantly, solar wind proton density needs to fall below $n_{\mathrm{sw}} < 4\ \mathrm{cm}^{-3}$ for enhancement events to occur, as no increase in fluxes is seen for higher proton densities. The use of these threshold values for solar wind parameters, provide a good simple forecasting method for relativistic electron enhancement events occurrence that was able to predict 90% of events on an out-sample dataset (2007-2010).

In Chapter 4 we studied the radial response of the outer radiation belt during relativistic electron enhancements at geostationary orbit by comparing data from the Van Allen Probes mission across the entire outer radiation belt, with the data from the GOES satellites. Using the knowledge developed in Chapter 3 about the solar wind parameters favorable for enhancements at geostationary orbit, we wanted to investigate how the rest of the outer belt might respond to the same external driver. The purpose was both scientific and technical, as following the end of the Van Allen Probes mission, direct measurements of outer belt fluxes is restricted to either low altitude satellites or geostationary orbit, and therefore understanding the coherence in the response of the belt is crucial for forecast purposes. We calculated the occurrence rates as function of L-shell and the correlation of fluxes between geostationary orbit and the rest of the outer belt and analyzed the response of the outer radiation belt according to the intensity of geomagnetic activity, in particular, SYM-H index, daily averaged AE index and Kp index. We found that in general the response of the radiation belt during enhancement events is cohesive for $L > 5.0$, and highly correlated for all $L > 4.5$. While the radiation belt seems to be in a state of low correlation just before enhancement events, in particular for $L < 5.0$, post enhancement maximum fluxes show a remarkable correlation for all $L > 4.0$, indicating a strong re-ordering of the outer belt following geomagnetic disturbances. Pre existing fluxes at lower L-shells are shown to play a significant role in the apparent response of the belt and make the ratio of pre-to-post enhancement fluxes less predictable, in particular in the region $4.0 < L < 4.5$, which seems to be indicative of wave activity that needs to be further studied. We have also examined the roles of the SYM-H, Kp and AE indices and found that depending on their intensity, the response of different parts of the outer belt can be better quantified, in particular in the regions $3.5 < L < 4.5$ which could be used for improving the current forecasting methods.

Chapter 5 focus was the recently discovered remnant belt associated with a three belt configuration of the radiation belts (*Baker et al.*, 2013a). Although initially thought to be a unique or highly rare configuration, we reported that these remnant belts occur more often than previously thought, with almost 20% of geomagnetic storms resulting in a remnant belt of ultrarelativisic electrons and a three-belt configuration. We reported the main characteristics of 30 three-belt events that occurred between 2012 and 2017 using Van Allen Probes. We found that the formation of a three-belt event can be associated with either a slow erosion of the outer belt that leaves a remnant belt and that is then followed by a disturbance that creates a new outermost belt, or that the formation occurs through a quick partial depletion followed by a re-formation of the outer belt. Events in the second category are most likely influenced by the magnetopause minimum location, suggesting that radial transport may play a role in some events (e.g. *Mann et al.*, 2016, 2018). We also showed that their location correlates with SYM-H minimum index and depends on the energy of the remnant belt, with higher energies presenting remnant belts at lower L-shells. Remnant belts were studied from 1.8 to 7.6 MeV, mostly by instrumentation limitations, since they can also occur at lower energies. We calculated the decay rate of the remnant belts when it showed a simple exponential decay, suggested to be associated with plasmaspheric hiss scattering (*Thorne et al.*, 2013b) and on average their decay rates get longer as energy increases ranging from days at $E = 1.8$ MeV up to months at $E = 6.3$ MeV which also indicates that remnant belts are extremely persistent.

In Chapter 6 we used the decay rates calculated for remnant belts in Chapter 5 and compared them to the theoretical scaling law $\gamma p^{3/2}$ of the lifetimes of ultrarelativistic electrons as a function of energy for $E > 3$ MeV in the region $L < 4.0$ (*Mourenas et al.*, 2017). For this comparison we used the 25 ultrarelativistic electron remnant belts that presented well defined exponential decays in the original study. The theoretical scaling law of electron lifetimes has been derived from quasi-linear theory. We demonstrated that, in general, the observed decay rates and their scaling with electron energy are in good agreement with theoretical lifetimes of ultrarelativistic electrons calculated for hiss-induced loss based on statistics of hiss waves and plasmaspheric density (e.g. *Mourenas and Ripoll*, 2012). In addition, we found in some cases a variation of lifetimes with energy very different from this theoretical scaling, such that lifetimes remained constant over a range of energy $\sim 3 - 5$ MeV, contrary to the theoretical expectation of a continued increase with energy in the presence of hiss alone. This slower increase of lifetimes with energy indicates the likely presence of an additional loss due to other waves than hiss. We showed that this behavior is apparently unrelated to inward radial diffusion. We checked that the combined presence of observed hiss waves and EMIC waves of small time-averaged amplitudes indeed allowed us to recover the observed variation of multi-MeV electron lifetimes with energy.

Future Work

While this dissertation has provided some answers to the problem of the influence of the solar wind on the dynamics of the outer radiation belt, it has also resulted in some new questions that should be addressed in the future for further improving our understanding of the radiation belts. Some possible extensions to this work are now presented.

Chapter 3 presented a study of both relativistic electron enhancement events and persistent depletions, however, in Chapter 4 only enhancements were considered. A study of the radial response of persistent depletions detected at geostationary orbit can lead to further understanding of the coherence in the response of the radiation belt to external solar wind driving. In particular, the question of what is the lowest L of depletion? How persistent in time those depletions are, can help us further understand the balance of loss mechanisms versus acceleration mechanisms at different altitudes.

Chapter 4 also showed that even for enhancement events at geosynchronous orbit, some regions of the outer belt can respond with strong depletions. This is most likely due to localized losses being relevant for the dynamics of the belt at very narrow locations. A study on the conditions that lead to these spatially constrained losses is needed if we plan to utilize remote measurements, such as the geostationary orbit to predict the response of the whole outer radiation belt.

Regarding remnant belts of ultra-relativistic electrons, Chapter 5 opened a whole new set of questions to be answered. The formation process of remnant belts seems to be associated to at least two different process; fast partial depletion and slow erosion of the outer belt, and these mechanisms should be explored in detail. The decay process of remnant belts has already been mostly addressed in Chapter 6, however, the persistence of the second "slot" region must be addressed, as well as the dependence of the remnant belt location with energy. It is important to note that the creation of a remnant belt is in principle not necessarily coupled to the creation of a new outer belt, and therefore we should understand under which circumstances the system will result in an isolated remnant belt and when it is going to lead to a three-belt configuration.

Bibliography

Agapitov, O., D. Mourenas, A. Artemyev, F. S. Mozer, J. W. Bonnell, V. Angelopoulos, V. Shastun, and V. Krasnoselskikh (2018), Spatial Extent and Temporal Correlation of Chorus and Hiss: Statistical Results From Multipoint THEMIS Observations, *Journal of Geophysical Research: Space Physics*, doi:10.1029/2018JA025725.

Agapitov, O. V., A. V. Artemyev, D. Mourenas, Y. Kasahara, and V. Krasnoselskikh (2014), Inner belt and slot region electron lifetimes and energization rates based on AKEBONO statistics of whistler waves, *Journal of Geophysical Research: Space Physics*, *119*(4), 2876–2893, doi:10.1002/2014JA019886.

Albert, J., and Y. Shprits (2009), Estimates of lifetimes against pitch angle diffusion, *Journal of Atmospheric and Solar-Terrestrial Physics*, *71*(16), 1647–1652, doi:10.1016/j.jastp.2008.07.004.

Anderson, B. R., R. M. Millan, G. D. Reeves, and R. H. W. Friedel (2015), Acceleration and loss of relativistic electrons during small geomagnetic storms, *Geophysical Research Letters*, *42*(23), 10,113–10,119, doi:10.1002/2015GL066376.

Antonova, E. E., M. V. Stepanova, P. S. Moya, V. A. Pinto, V. V. Vovchenko, I. L. Ovchinnikov, and N. V. Sotnikov (2018), Processes in auroral oval and outer electron radiation belt, *Earth, Planets and Space*, *70*(1), doi:10.1186/s40623-018-0898-1.

Artemyev, A. V., D. Mourenas, O. V. Agapitov, and V. V. Krasnoselskikh (2013), Parametric validations of analytical lifetime estimates for radiation belt electron diffusion by whistler waves, *Annales Geophysicae*, *31*(4), 599–624, doi:10.5194/angeo-31-599-2013.

Baker, D., X. Li, J. Blake, and S. Kanekal (1998), Strong electron acceleration in the Earth's magnetosphere, *Advances in Space Research*, *21*(4), 609–613, doi:10.1016/S0273-1177(97)00970-8.

Baker, D. N. (2000), The occurrence of operational anomalies in spacecraft and their relationship to space weather, *IEEE Transactions on Plasma Science*, *28*(6), 2007–2016.

Baker, D. N., J. B. Blake, R. W. Klebesadel, and P. R. Higbie (1986), Highly relativistic electrons in the Earth's outer magnetosphere: 1. Lifetimes and temporal history 1979–1984, *Journal of Geophysical Research*, *91*(A4), 4265, doi:10.1029/JA091iA04p04265.

Baker, D. N., R. L. McPherron, T. E. Cayton, and R. W. Klebesadel (1990), Linear prediction filter analysis of relativistic electron properties at 6.6 R_E, *Journal of Geophysical Research*, *95*(A9), 15,133, doi:10.1029/JA095iA09p15133.

Baker, D. N., J. B. Blake, L. B. Callis, J. R. Cummings, D. Hovestadt, S. Kanekal, B. Klecker, R. A. Mewaldt, and R. D. Zwickl (1994), Relativistic electron acceleration and decay time scales in the inner and outer radiation belts: SAMPEX, *Geophys. Res. Lett.*, *21*(6), 409–412, doi:10.1029/93GL03532.

Baker, D. N., S. G. Kanekal, V. C. Hoxie, M. G. Henderson, X. Li, H. E. Spence, S. R. Elkington, R. H. W. Friedel, J. Goldstein, M. K. Hudson, G. D. Reeves, R. M. Thorne, C. A. Kletzing, and S. G. Claudepierre (2013a), A Long-Lived Relativistic Electron Storage Ring Embedded in Earth's Outer Van Allen Belt, *Science*, *340*(6129), 186–190, doi:10.1126/science.1233518.

Baker, D. N., S. G. Kanekal, V. C. Hoxie, S. Batiste, M. Bolton, X. Li, S. R. Elkington, S. Monk, R. Reukauf, S. Steg, J. Westfall, C. Belting, B. Bolton, D. Braun, B. Cervelli, K. Hubbell, M. Kien, S. Knappmiller, S. Wade, B. Lamprecht, K. Stevens, J. Wallace, A. Yehle, H. E. Spence, and R. Friedel (2013b), The Relativistic Electron-Proton Telescope (REPT) Instrument on Board the Radiation Belt Storm Probes (RBSP) Spacecraft: Characterization of Earth's Radiation Belt High-Energy Particle Populations, *Space Science Reviews*, *179*(1-4), 337–381, doi:10.1007/s11214-012-9950-9.

Baker, D. N., A. N. Jaynes, S. G. Kanekal, J. C. Foster, P. J. Erickson, J. F. Fennell, J. B. Blake, H. Zhao, X. Li, S. R. Elkington, M. G. Henderson, G. D. Reeves, H. E. Spence, C. A. Kletzing, and J. R. Wygant (2016), Highly relativistic radiation belt electron acceleration, transport, and loss: Large solar storm events of March and June 2015, *Journal of Geophysical Research: Space Physics*, *121*(7), 6647–6660, doi:10.1002/2016JA022502.

Baker, D. N., P. J. Erickson, J. F. Fennell, J. C. Foster, A. N. Jaynes, and P. T. Verronen (2018), Space Weather Effects in the Earth's Radiation Belts, *Space Science Reviews*, *214*(1), doi:10.1007/s11214-017-0452-7.

Baker, D. N., H. Zhao, X. Li, S. G. Kanekal, and A. N. Jaynes (2019), Comparison of Van Allen Probes Energetic Electron Data with Corresponding GOES-15 Measurements: 2012 - 2018, *Journal of Geophysical Research: Space Physics*.

Balikhin, M. A., R. J. Boynton, S. N. Walker, J. E. Borovsky, S. A. Billings, and H. L. Wei (2011), Using the NARMAX approach to model the evolution of energetic electrons fluxes at geostationary orbit, *Geophysical Research Letters*, *38*(18), n/a–n/a, doi:10.1029/2011GL048980.

Baumjohann, W., and R. A. Treumann (1997), *Basic space plasma physics*, reprinted ed., Imperial College Press, London, oCLC: 253914511.

Bingham, S. T., C. G. Mouikis, L. M. Kistler, A. J. Boyd, K. Paulson, C. J. Farrugia, C. L. Huang, H. E. Spence, S. G. Claudepierre, and C. Kletzing (2018), The outer radiation belt response to the storm time development of seed electrons and chorus wave activity during CME and CIR storms, *Journal of Geophysical Research: Space Physics*, doi:10.1029/2018JA025963.

Blake, J. B., D. N. Baker, N. Turner, K. W. Ogilvie, and R. P. Lepping (1997), Correlation of changes in the outer-zone relativistic-electron population with upstream solar wind and magnetic field measurements, *Geophysical Research Letters*, *24*(8), 927–929, doi:10.1029/97GL00859.

Blum, L. W., and A. W. Breneman (2019), Observations of radiation belt losses due to cyclotron wave-particle interactions, in *The Dynamic Loss of Earth's Radiation Belts*, pp. 49–98, Elsevier, doi:10.1016/B978-0-12-813371-2.00003-2.

Blum, L. W., A. Halford, R. Millan, J. W. Bonnell, J. Goldstein, M. Usanova, M. Engebretson, M. Ohnsted, G. Reeves, H. Singer, M. Clilverd, and X. Li (2015), Observations of coincident EMIC wave activity and duskside energetic electron precipitation on 18-19 January 2013: EMIC Waves and Electron Precipitation, *Geophysical Research Letters*, *42*(14), 5727–5735, doi:10.1002/2015GL065245.

Borovsky, J. E. (2017), Time-Integral Correlations of Multiple Variables With the Relativistic-Electron Flux at Geosynchronous Orbit: The Strong Roles of Substorm-Injected Electrons and the Ion Plasma Sheet: Time-Integral Radiation Belt Correlation, *J. Geophys. Res. Space Physics*, *122*(12), 11,961–11,990, doi:10.1002/2017JA024476.

Borovsky, J. E., and M. H. Denton (2006), Differences between CME-driven storms and CIR-driven storms, *Journal of Geophysical Research*, *111*(A7), doi:10.1029/2005JA011447.

Borovsky, J. E., and M. H. Denton (2010), Magnetic field at geosynchronous orbit during high-speed stream-driven storms: Connections to the solar wind, the plasma sheet, and the outer electron radiation belt, *Journal of Geophysical Research: Space Physics*, *115*(A8), n/a–n/a, doi:10.1029/2009JA015116.

Bortnik, J., and R. Thorne (2007), The dual role of ELF/VLF chorus waves in the acceleration and precipitation of radiation belt electrons, *Journal of Atmospheric and Solar-Terrestrial Physics*, *69*(3), 378–386, doi:10.1016/j.jastp.2006.05.030.

Bortnik, J., R. M. Thorne, T. P. O'Brien, J. C. Green, R. J. Strangeway, Y. Y. Shprits, and D. N. Baker (2006), Observation of two distinct, rapid loss mechanisms during the 20 November 2003 radiation belt dropout event, *Journal of Geophysical Research*, *111*(A12), doi:10.1029/2006JA011802.

Bortnik, J., R. M. Thorne, and N. P. Meredith (2008), The unexpected origin of plasmaspheric hiss from discrete chorus emissions, *Nature*, *452*(7183), 62–66, doi:10.1038/nature06741.

Bortnik, J., W. Li, R. M. Thorne, V. Angelopoulos, C. Cully, J. Bonnell, O. Le Contel, and A. Roux (2009), An Observation Linking the Origin of Plasmaspheric Hiss to Discrete Chorus Emissions, *Science*, *324*(5928), 775–778, doi:10.1126/science.1171273.

Boynton, R. J., M. A. Balikhin, and S. A. Billings (2015), Online NARMAX model for electron fluxes at GEO, *Annales Geophysicae*, *33*(3), 405–411, doi:10.5194/angeo-33-405-2015.

Boynton, R. J., D. Mourenas, and M. A. Balikhin (2016), Electron flux dropouts at Geostationary Earth Orbit: Occurrences, magnitudes, and main driving factors, *Journal of Geophysical Research: Space Physics*, *121*(9), 8448–8461, doi:10.1002/2016JA022916.

Cao, X., Y. Y. Shprits, B. Ni, and I. S. Zhelavskaya (2017), Scattering of Ultra-relativistic Electrons in the Van Allen Radiation Belts Accounting for Hot Plasma Effects, *Scientific Reports*, *7*(1), doi:10.1038/s41598-017-17739-7.

Carpenter, D. L. (1963), Whistler measurements of electron density and magnetic field strength in the remote magnetosphere, *J. Geophys. Res.*, *68*(12), 3727–3730, doi:10.1029/JZ068i012p03727.

Carpenter, D. L., and R. R. Anderson (1992), An ISEE/whistler model of equatorial electron density in the magnetosphere, *J. Geophys. Res.*, *97*(A2), 1097, doi:10.1029/91JA01548.

Chen, F. F. (1983), *Introduction to Plasma Physics and Controlled Fusion*, Springer International Publishing, Cham, doi:10.1007/978-3-319-22309-4.

Chen, L., R. M. Thorne, and R. B. Horne (2009), Simulation of EMIC wave excitation in a model magnetosphere including structured high-density plumes: EMIC EXCITATION IN PLUMES, *J. Geophys. Res.*, *114*(A7), n/a–n/a, doi:10.1029/2009JA014204.

Chen, L., R. M. Thorne, and J. Bortnik (2011), The controlling effect of ion temperature on EMIC wave excitation and scattering, *Geophysical Research Letters*, *38*(16), n/a–n/a, doi:10.1029/2011GL048653.

Claudepierre, S. G., T. P. O'Brien, J. B. Blake, J. F. Fennell, J. L. Roeder, J. H. Clemmons, M. D. Looper, J. E. Mazur, T. M. Mulligan, H. E. Spence, G. D. Reeves, R. H. W. Friedel, M. G. Henderson, and B. A. Larsen (2015), A background correction algorithm for Van

Allen Probes MagEIS electron flux measurements, *Journal of Geophysical Research: Space Physics*, *120*(7), 5703–5727, doi:10.1002/2015JA021171.

Comfort, R. H., I. T. Newberry, and C. R. Chappell (1988), Preliminary statistical survey of plasmaspheric ion properties from observations by DE 1/RIMS, in *Geophysical Monograph Series*, vol. 44, edited by T. E. Moore, J. H. Waite, T. W. Moorehead, and W. B. Hanson, pp. 107–114, American Geophysical Union, Washington, D. C., doi:10.1029/GM044p0107.

Daglis, I. A., R. M. Thorne, W. Baumjohann, and S. Orsini (1999), The terrestrial ring current: Origin, formation, and decay, *Reviews of Geophysics*, *37*(4), 407–438, doi:10.1029/1999RG900009.

Denton, M. H., and J. E. Borovsky (2012), Magnetosphere response to high-speed solar wind streams: A comparison of weak and strong driving and the importance of extended periods of fast solar wind, *J. Geophys. Res.*, *117*(A9), n/a–n/a, doi:10.1029/2011JA017124.

Drozdov, A. Y., Y. Y. Shprits, K. G. Orlova, A. C. Kellerman, D. A. Subbotin, D. N. Baker, H. E. Spence, and G. D. Reeves (2015), Energetic, relativistic, and ultrarelativistic electrons: Comparison of long-term VERB code simulations with Van Allen Probes measurements, *Journal of Geophysical Research: Space Physics*, *120*(5), 3574–3587, doi:10.1002/2014JA020637.

Gao, X., W. Li, J. Bortnik, R. M. Thorne, Q. Lu, Q. Ma, X. Tao, and S. Wang (2015), The effect of different solar wind parameters upon significant relativistic electron flux dropouts in the magnetosphere, *Journal of Geophysical Research: Space Physics*, *120*(6), 4324–4337, doi:10.1002/2015JA021182.

Gonzalez, W. D., J. A. Joselyn, Y. Kamide, H. W. Kroehl, G. Rostoker, B. T. Tsurutani, and V. M. Vasyliunas (1994), What is a geomagnetic storm?, *Journal of Geophysical Research*, *99*(A4), 5771, doi:10.1029/93JA02867.

Green, J. C. (2004), Relativistic electrons in the outer radiation belt: Differentiating between acceleration mechanisms, *Journal of Geophysical Research*, *109*(A3), doi: 10.1029/2003JA010153.

Hajra, R., B. T. Tsurutani, E. Echer, W. D. Gonzalez, and O. Santolik (2015), Relativistic (E > 0.6, > 2.0, AND > 4.0 MeV) Electron Acceleration at Geosynchronous Orbit During High-Intensity, Long-Duration, Continuous AE Activity (HILDCAA) Events, *The Astrophysical Journal*, *799*(1), 39, doi:10.1088/0004-637X/799/1/39.

Hietala, H., E. K. J. Kilpua, D. L. Turner, and V. Angelopoulos (2014), Depleting effects of ICME-driven sheath regions on the outer electron radiation belt, *Geophysical Research Letters*, *41*(7), 2258–2265, doi:10.1002/2014GL059551.

Hill, T. W., and A. J. Dessler (1991), Plasma Motions in Planetary Magnetospheres, *Science*, *252*(5004), 410–415, doi:10.1126/science.252.5004.410.

Horne, R. B., R. M. Thorne, S. A. Glauert, N. P. Meredith, D. Pokhotelov, and O. Santolík (2007), Electron acceleration in the Van Allen radiation belts by fast magnetosonic waves, *Geophysical Research Letters*, *34*(17), doi:10.1029/2007GL030267.

Horne, R. B., S. A. Glauert, N. P. Meredith, D. Boscher, V. Maget, D. Heynderickx, and D. Pitchford (2013), Space weather impacts on satellites and forecasting the Earth's electron radiation belts with SPACECAST, *Space Weather*, *11*(4), 169–186, doi:10.1002/swe.20023.

Hudson, M. K., B. T. Kress, H.-R. Mueller, J. A. Zastrow, and J. Bernard Blake (2008), Relationship of the Van Allen radiation belts to solar wind drivers, *Journal of Atmospheric and Solar-Terrestrial Physics*, *70*(5), 708–729, doi:10.1016/j.jastp.2007.11.003.

Hwang, J. A., D.-Y. Lee, L. R. Lyons, A. J. Smith, S. Zou, K. W. Min, K.-H. Kim, Y.-J. Moon, and Y. D. Park (2007), Statistical significance of association between whistler-mode chorus enhancements and enhanced convection periods during high-speed streams, *Journal of Geophysical Research: Space Physics*, *112*(A9), n/a–n/a, doi: 10.1029/2007JA012388.

Hyun, K., K.-H. Kim, E. Lee, H.-J. Kwon, D.-H. Lee, and H. Jin (2014), Loss of geosynchronous relativistic electrons by EMIC wave scattering under quiet geomagnetic conditions, *Journal of Geophysical Research: Space Physics*, *119*(10), 8357–8371, doi: 10.1002/2014JA020234.

Iles, R. H. A., A. N. Fazakerley, A. D. Johnstone, N. P. Meredith, and P. Bühler (2002), The relativistic electron response in the outer radiation belt during magnetic storms, *Annales Geophysicae*, *20*, 957–965.

Jaynes, A. N., D. N. Baker, H. J. Singer, J. V. Rodriguez, T. M. Loto'aniu, A. F. Ali, S. R. Elkington, X. Li, S. G. Kanekal, S. G. Claudepierre, J. F. Fennell, W. Li, R. M. Thorne, C. A. Kletzing, H. E. Spence, and G. D. Reeves (2015), Source and seed populations for relativistic electrons: Their roles in radiation belt changes, *Journal of Geophysical Research: Space Physics*, *120*(9), 7240–7254, doi:10.1002/2015JA021234.

Jordanova, V. K., J. Albert, and Y. Miyoshi (2008), Relativistic electron precipitation by EMIC waves from self-consistent global simulations, *Journal of Geophysical Research: Space Physics*, *113*(A3), n/a–n/a, doi:10.1029/2008JA013239.

Kan, J. R., and L. C. Lee (1979), Energy coupling function and solar wind-magnetosphere dynamo, *Geophysical Research Letters*, *6*(7), 577–580.

Kanekal, S. G., D. N. Baker, and J. B. Blake (2001), Multisatellite measurements of relativistic electrons: Global coherence, *Journal of Geophysical Research: Space Physics*, *106*(A12), 29,721–29,732, doi:10.1029/2001JA000070.

Kataoka, R., and Y. Miyoshi (2006), Flux enhancement of radiation belt electrons during geomagnetic storms driven by coronal mass ejections and corotating interaction regions, *Space Weather*, *4*(9), n/a–n/a, doi:10.1029/2005SW000211.

Katsavrias, C., I. A. Daglis, and W. Li (2019), On the Statistics of Acceleration and Loss of Relativistic Electrons in the Outer Radiation Belt: A Superposed Epoch Analysis, *J. Geophys. Res. Space Physics*, p. 2019JA026569, doi:10.1029/2019JA026569.

Kellerman, A. C., Y. Y. Shprits, D. Kondrashov, D. Subbotin, R. A. Makarevich, E. Donovan, and T. Nagai (2014), Three-dimensional data assimilation and reanalysis of radiation belt electrons: Observations of a four-zone structure using five spacecraft and the VERB code, *Journal of Geophysical Research: Space Physics*, *119*(11), 8764–8783, doi: 10.1002/2014JA020171.

Kersten, T., R. B. Horne, S. A. Glauert, N. P. Meredith, B. J. Fraser, and R. S. Grew (2014), Electron losses from the radiation belts caused by EMIC waves, *Journal of Geophysical Research: Space Physics*, *119*(11), 8820–8837, doi:10.1002/2014JA020366.

Kim, H.-J., and A. A. Chan (1997), Fully adiabatic changes in storm time relativistic electron fluxes, *Journal of Geophysical Research: Space Physics*, *102*(A10), 22,107–22,116, doi:10.1029/97JA01814.

Kim, H.-J., K. C. Kim, D.-Y. Lee, and G. Rostoker (2006), Origin of geosynchronous relativistic electron events, *Journal of Geophysical Research*, *111*(A3), doi:10.1029/2005JA011469.

Kim, H.-J., L. Lyons, V. Pinto, C.-P. Wang, and K.-C. Kim (2015), Revisit of relationship between geosynchronous relativistic electron enhancements and magnetic storms, *Geophysical Research Letters*, *42*(15), 6155–6161, doi:10.1002/2015GL065192.

Kim, K. C., D.-Y. Lee, H.-J. Kim, E. S. Lee, and C. R. Choi (2010), Numerical estimates of drift loss and Dst effect for outer radiation belt relativistic electrons with arbitrary pitch angle, *Journal of Geophysical Research: Space Physics*, *115*(A3), n/a–n/a, doi:10.1029/2009JA014523.

Kissinger, J., L. Kepko, D. N. Baker, S. Kanekal, W. Li, R. L. McPherron, and V. Angelopoulos (2014), The importance of storm time steady magnetospheric convection in determining the final relativistic electron flux level, *Journal of Geophysical Research: Space Physics*, *119*(9), 7433–7443, doi:10.1002/2014JA019948.

Kivelson, M. G., and C. T. Russell (Eds.) (1995), *Introduction to space physics*, Cambridge University Press, Cambridge ; New York.

Kletzing, C. A., W. S. Kurth, M. Acuna, R. J. MacDowall, R. B. Torbert, T. Averkamp, D. Bodet, S. R. Bounds, M. Chutter, J. Connerney, D. Crawford, J. S. Dolan, R. Dvorsky, G. B. Hospodarsky, J. Howard, V. Jordanova, R. A. Johnson, D. L. Kirchner, B. Mokrzycki, G. Needell, J. Odom, D. Mark, R. Pfaff, J. R. Phillips, C. W. Piker, S. L. Remington, D. Rowland, O. Santolik, R. Schnurr, D. Sheppard, C. W. Smith, R. M. Thorne, and J. Tyler (2013), The Electric and Magnetic Field Instrument Suite and Integrated Science (EMFISIS) on RBSP, *Space Science Reviews*, *179*(1-4), 127–181, doi: 10.1007/s11214-013-9993-6.

Kozyreva, O., V. Pilipenko, M. Engebretson, K. Yumoto, J. Watermann, and N. Romanova (2007), In search of a new ULF wave index: Comparison of Pc5 power with dynamics of geostationary relativistic electrons, *Planetary and Space Science*, *55*(6), 755–769, doi: 10.1016/j.pss.2006.03.013.

Kurth, W. S., S. De Pascuale, J. B. Faden, C. A. Kletzing, G. B. Hospodarsky, S. Thaller, and J. R. Wygant (2015), Electron densities inferred from plasma wave spectra obtained by the Waves instrument on Van Allen Probes: Van Allen Probes Electron Densities, *Journal of Geophysical Research: Space Physics*, *120*(2), 904–914, doi: 10.1002/2014JA020857.

Li, L. Y., J. B. Cao, G. C. Zhou, and X. Li (2009), Statistical roles of storms and substorms in changing the entire outer zone relativistic electron population, *Journal of Geophysical Research: Space Physics*, *114*(A12), n/a–n/a, doi:10.1029/2009JA014333.

Li, W., Y. Y. Shprits, and R. M. Thorne (2007), Dynamic evolution of energetic outer zone electrons due to wave-particle interactions during storms, *Journal of Geophysical Research: Space Physics*, *112*(A10), n/a–n/a, doi:10.1029/2007JA012368.

Li, W., R. M. Thorne, J. Bortnik, G. D. Reeves, C. A. Kletzing, W. S. Kurth, G. B. Hospodarsky, H. E. Spence, J. B. Blake, J. F. Fennell, S. G. Claudepierre, J. R. Wygant, and S. A. Thaller (2013), An unusual enhancement of low-frequency plasmaspheric hiss in the outer plasmasphere associated with substorm-injected electrons, *Geophysical Research Letters*, *40*(15), 3798–3803, doi:10.1002/grl.50787.

Li, W., Q. Ma, R. M. Thorne, J. Bortnik, C. A. Kletzing, W. S. Kurth, G. B. Hospodarsky, and Y. Nishimura (2015a), Statistical properties of plasmaspheric hiss derived from Van Allen Probes data and their effects on radiation belt electron dynamics, *Journal of Geophysical Research: Space Physics*, *120*(5), 3393–3405, doi:10.1002/2015JA021048.

Li, W., R. M. Thorne, J. Bortnik, D. N. Baker, G. D. Reeves, S. G. Kanekal, H. E. Spence, and J. C. Green (2015b), Solar wind conditions leading to efficient radiation belt electron acceleration: A superposed epoch analysis, *Geophysical Research Letters*, *42*(17), 6906–6915, doi:10.1002/2015GL065342.

Li, X., D. N. Baker, M. Teremin, T. E. Cayton, G. D. Reeves, R. S. Selesnick, J. B. Blake, G. Lu, S. G. Kanekal, and H. J. Singer (1999), Rapid enchancements of relativistic electrons deep in the magnetosphere during the May 15, 1997, magnetic storm, *J. Geophys. Res.*, *104*(A3), 4467–4476, doi:10.1029/1998JA900092.

Li, X., M. Temerin, D. N. Baker, G. D. Reeves, and D. Larson (2001), Quantitative prediction of radiation belt electrons at geostationary orbit based on solar wind measurements, *Geophysical Research Letters*, *28*(9), 1887–1890.

Li, X., D. N. Baker, M. Temerin, G. Reeves, R. Friedel, and C. Shen (2005), Energetic electrons, 50 keV to 6 MeV, at geosynchronous orbit: Their responses to solar wind variations, *Space Weather*, *3*(4), n/a–n/a, doi:10.1029/2004SW000105.

Lyatsky, W., and G. V. Khazanov (2008), Effect of solar wind density on relativistic electrons at geosynchronous orbit, *Geophysical Research Letters*, *35*(3), doi:10.1029/2007GL032524.

Lyons, L., D.-Y. Lee, H.-J. Kim, J. Hwang, R. Thorne, R. Horne, and A. Smith (2009), Solar-wind–magnetosphere coupling, including relativistic electron energization, during high-speed streams, *Journal of Atmospheric and Solar-Terrestrial Physics*, *71*(10-11), 1059–1072, doi:10.1016/j.jastp.2008.04.016.

Lyons, L. R., and R. M. Thorne (1973), Equilibrium structure of radiation belt electrons, *Journal of Geophysical Research*, *78*(13), 2142–2149, doi:10.1029/JA078i013p02142.

Lyons, L. R., R. M. Thorne, and C. F. Kennel (1972), Pitch-angle diffusion of radiation belt electrons within the plasmasphere, *Journal of Geophysical Research*, *77*(19), 3455–3474, doi:10.1029/JA077i019p03455.

Lyons, L. R., D.-Y. Lee, R. M. Thorne, R. B. Horne, and A. J. Smith (2005), Solar wind-magnetosphere coupling leading to relativistic electron energization during high-speed streams, *Journal of Geophysical Research*, *110*(A11), doi:10.1029/2005JA011254.

Ma, Q., W. Li, R. M. Thorne, B. Ni, C. A. Kletzing, W. S. Kurth, G. B. Hospodarsky, G. D. Reeves, M. G. Henderson, H. E. Spence, D. N. Baker, J. B. Blake, J. F. Fennell, S. G. Claudepierre, and V. Angelopoulos (2015), Modeling inward diffusion and slow decay of energetic electrons in the Earth's outer radiation belt: Modeling gradual diffusion processes, *Geophysical Research Letters*, *42*(4), 987–995, doi:10.1002/2014GL062977.

Malaspina, D. M., A. N. Jaynes, C. Boulé, J. Bortnik, S. A. Thaller, R. E. Ergun, C. A. Kletzing, and J. R. Wygant (2016), The distribution of plasmaspheric hiss wave power with respect to plasmapause location, *Geophysical Research Letters*, *43*(15), 7878–7886, doi:10.1002/2016GL069982.

Mann, I., T. O'Brien, and D. Milling (2004), Correlations between ULF wave power, solar wind speed, and relativistic electron flux in the magnetosphere: solar cycle dependence, *Journal of Atmospheric and Solar-Terrestrial Physics*, *66*(2), 187–198, doi: 10.1016/j.jastp.2003.10.002.

Mann, I. R., E. A. Lee, S. G. Claudepierre, J. F. Fennell, A. Degeling, I. J. Rae, D. N. Baker, G. D. Reeves, H. E. Spence, L. G. Ozeke, R. Rankin, D. K. Milling, A. Kale, R. H. W. Friedel, and F. Honary (2013), Discovery of the action of a geophysical synchrotron in the Earth's Van Allen radiation belts, *Nature Communications*, *4*, doi: 10.1038/ncomms3795.

Mann, I. R., L. G. Ozeke, K. R. Murphy, S. G. Claudepierre, D. L. Turner, D. N. Baker, I. J. Rae, A. Kale, D. K. Milling, A. J. Boyd, H. E. Spence, G. D. Reeves, H. J. Singer, S. Dimitrakoudis, I. A. Daglis, and F. Honary (2016), Explaining the dynamics of the ultra-relativistic third Van Allen radiation belt, *Nature Physics*, *12*(10), 978–983, doi: 10.1038/nphys3799.

Mann, I. R., L. G. Ozeke, S. K. Morley, K. R. Murphy, S. G. Claudepierre, D. L. Turner, D. N. Baker, I. J. Rae, A. Kale, D. K. Milling, A. J. Boyd, H. E. Spence, H. J. Singer, S. Dimitrakoudis, I. A. Daglis, and F. Honary (2018), Reply to 'The dynamics of Van Allen belts revisited', *Nature Physics*, *14*(2), 103–104, doi:10.1038/nphys4351.

Mathie, R. A., and I. R. Mann (2000), A correlation between extended intervals of Ulf wave power and storm-time geosynchronous relativistic electron flux enhancements, *Geophysical Research Letters*, *27*(20), 3261–3264, doi:10.1029/2000GL003822.

Mauk, B. H., N. J. Fox, S. G. Kanekal, R. L. Kessel, D. G. Sibeck, and A. Ukhorskiy (2013), Science Objectives and Rationale for the Radiation Belt Storm Probes Mission, *Space Science Reviews*, *179*(1-4), 3–27, doi:10.1007/s11214-012-9908-y.

McIlwain, C. E. (1961), Coordinates for mapping the distribution of magnetically trapped particles, *Journal of Geophysical Research*, *66*(11), 3681–3691, doi:10.1029/JZ066i011p03681.

McPherron, R., D. Baker, and N. Crooker (2009), Role of the Russell–McPherron effect in the acceleration of relativistic electrons, *Journal of Atmospheric and Solar-Terrestrial Physics*, *71*(10-11), 1032–1044, doi:10.1016/j.jastp.2008.11.002.

Meredith, N. P. (2002), Outer zone relativistic electron acceleration associated with substorm-enhanced whistler mode chorus, *Journal of Geophysical Research*, *107*(A7), doi: 10.1029/2001JA900146.

Meredith, N. P. (2003), Evidence for chorus-driven electron acceleration to relativistic energies from a survey of geomagnetically disturbed periods, *Journal of Geophysical Research*, *108*(A6), doi:10.1029/2002JA009764.

Meredith, N. P., R. B. Horne, S. A. Glauert, and R. R. Anderson (2007), Slot region electron loss timescales due to plasmaspheric hiss and lightning-generated whistlers, *Journal of Geophysical Research: Space Physics*, *112*(A8), n/a–n/a, doi:10.1029/2007JA012413.

Meredith, N. P., R. B. Horne, J. Bortnik, R. M. Thorne, L. Chen, W. Li, and A. Sicard-Piet (2013), Global statistical evidence for chorus as the embryonic source of plasmaspheric hiss, *Geophysical Research Letters*, *40*(12), 2891–2896, doi:10.1002/grl.50593.

Meredith, N. P., R. B. Horne, T. Kersten, B. J. Fraser, and R. S. Grew (2014), Global morphology and spectral properties of EMIC waves derived from CRRES observations, *Journal of Geophysical Research: Space Physics*, *119*(7), 5328–5342, doi:10.1002/2014JA020064.

Millan, R., and R. Thorne (2007), Review of radiation belt relativistic electron losses, *Journal of Atmospheric and Solar-Terrestrial Physics*, *69*(3), 362–377, doi:10.1016/j.jastp.2006.06.019.

Miyoshi, Y., and R. Kataoka (2008), Flux enhancement of the outer radiation belt electrons after the arrival of stream interaction regions, *Journal of Geophysical Research: Space Physics*, *113*(A3), n/a–n/a, doi:10.1029/2007JA012506.

Mourenas, D., and J.-F. Ripoll (2012), Analytical estimates of quasi-linear diffusion coefficients and electron lifetimes in the inner radiation belt, *Journal of Geophysical Research: Space Physics*, *117*(A1), doi:10.1029/2011JA016985.

Mourenas, D., A. V. Artemyev, Q. Ma, O. V. Agapitov, and W. Li (2016), Fast dropouts of multi-MeV electrons due to combined effects of EMIC and whistler mode waves, *Geophysical Research Letters*, *43*(9), 4155–4163, doi:10.1002/2016GL068921.

Mourenas, D., Q. Ma, A. V. Artemyev, and W. Li (2017), Scaling laws for the inner structure of the radiation belts, *Geophysical Research Letters*, *44*(7), 3009–3018, doi:10.1002/2017GL072987.

Mourenas, D., X.-J. Zhang, A. V. Artemyev, V. Angelopoulos, R. M. Thorne, J. Bortnik, A. I. Neishtadt, and A. A. Vasiliev (2018), Electron Nonlinear Resonant Interaction with Short and Intense Parallel Chorus Wave Packets, *Journal of Geophysical Research: Space Physics*, doi:10.1029/2018JA025417.

Mourenas, D., A. V. Artemyev, and X. Zhang (2019), Impact of significant time-integrated geomagnetic activity on 2 MeV electron flux, *J. Geophys. Res. Space Physics*, p. 2019JA026659, doi:10.1029/2019JA026659.

Moya, P. S., V. A. Pinto, D. G. Sibeck, S. G. Kanekal, and D. N. Baker (2017), On the Effect of Geomagnetic Storms on Relativistic Electrons in the Outer Radiation Belt: Van Allen Probes Observations, *Journal of Geophysical Research: Space Physics*, *122*(11), 11,100–11,108, doi:10.1002/2017JA024735.

Murphy, K. R., C. E. J. Watt, I. R. Mann, I. Jonathan Rae, D. G. Sibeck, A. J. Boyd, C. F. Forsyth, D. L. Turner, S. G. Claudepierre, D. N. Baker, H. E. Spence, G. D. Reeves, J. B. Blake, and J. Fennell (2018), The Global Statistical Response of the Outer Radiation Belt During Geomagnetic Storms, *Geophysical Research Letters*, *45*(9), 3783–3792, doi:10.1002/2017GL076674.

Nakamura, S., Y. Omura, D. Summers, and C. A. Kletzing (2016), Observational evidence of the nonlinear wave growth theory of plasmaspheric hiss, *Geophysical Research Letters*, *43*(19), 10,040–10,049, doi:10.1002/2016GL070333.

Ni, B., X. Cao, Y. Y. Shprits, D. Summers, X. Gu, S. Fu, and Y. Lou (2018), Hot Plasma Effects on the Cyclotron-Resonant Pitch-Angle Scattering Rates of Radiation Belt Electrons Due to EMIC Waves: EMIC wave scattering in hot plasmas, *Geophysical Research Letters*, *45*(1), 21–30, doi:10.1002/2017GL076028.

O'Brien, T. P., and M. B. Moldwin (2003), Empirical plasmapause models from magnetic indices, *Geophysical Research Letters*, *30*(4), doi:10.1029/2002GL016007.

O'Brien, T. P., R. L. McPherron, D. Sornette, G. D. Reeves, R. Friedel, and H. J. Singer (2001), Which magnetic storms produce relativistic electrons at geosynchronous orbit?, *Journal of Geophysical Research: Space Physics*, *106*(A8), 15,533–15,544, doi:10.1029/2001JA000052.

Onsager, T., R. Grubb, J. Kunches, L. Matheson, D. Speich, R. W. Zwickl, and H. Sauer (1996), Operational uses of the GOES energetic particle detectors, pp. 281–290, doi:10.1117/12.254075.

Ozeke, L. G., I. R. Mann, K. R. Murphy, I. Jonathan Rae, and D. K. Milling (2014), Analytic expressions for ULF wave radiation belt radial diffusion coefficients: Analytic Radial Diffusion Coefficients, *Journal of Geophysical Research: Space Physics*, *119*(3), 1587–1605, doi:10.1002/2013JA019204.

Ozhogin, P., J. Tu, P. Song, and B. W. Reinisch (2012), Field-aligned distribution of the plasmaspheric electron density: An empirical model derived from the IMAGE RPI measurements, *Journal of Geophysical Research: Space Physics*, *117*(A6), n/a–n/a, doi:10.1029/2011JA017330.

Pandya, M., V. Bhaskara, Y. Ebihara, S. Kanekal, and D. N. Baker (2019), Variation of Radiation Belt Electron Flux During CME- and CIR-Driven Geomagnetic Storms: Van Allen Probes Observations, *J. Geophys. Res. Space Physics*, p. 2019JA026771, doi:10.1029/2019JA026771.

Parker, E. N. (1955), Hydromagnetic Dynamo Models., *ApJ*, *122*, 293, doi:10.1086/146087.

Paulikas, G., and J. Blake (1979), Effects of the Solar Wind on Magnetospheric Dynamics: Energetic Electrons at the Synchronous Orbit, in *Geophysical Monograph Series*, edited by W. P. Olson, pp. 180–202, American Geophysical Union, Washington, D. C., doi:10.1029/GM021p0180.

Pinto, V. A., H.-J. Kim, L. R. Lyons, and J. Bortnik (2018a), Interplanetary Parameters Leading to Relativistic Electron Enhancement and Persistent Depletion Events at Geosynchronous Orbit and Potential for Prediction, *Journal of Geophysical Research: Space Physics*, *123*(2), 1134–1145, doi:10.1002/2017JA024902.

Pinto, V. A., J. Bortnik, P. S. Moya, L. R. Lyons, D. G. Sibeck, S. G. Kanekal, H. E. Spence, and D. N. Baker (2018b), Characteristics, Occurrence, and Decay Rates of Remnant Belts Associated With Three-Belt Events in the Earth's Radiation Belts, *Geophysical Research Letters*, *45*(22), 12,099–12,107, doi:10.1029/2018GL080274.

Pinto, V. A., D. Mourenas, J. Bortnik, X. Zhang, A. V. Artemyev, P. S. Moya, and L. R. Lyons (2019), Decay of Ultrarelativistic Remnant Belt Electrons Through Scattering by Plasmaspheric Hiss, *J. Geophys. Res. Space Physics*, *124*(7), 5222–5233, doi:10.1029/2019JA026509.

Pizzella, G., C. D. Laughlin, and B. J. O'Brien (1962), Note on the electron energy spectrum in the inner Van Allen Belt, *J. Geophys. Res.*, *67*(9), 3281–3287, doi:10.1029/JZ067i009p03281.

Potapov, A., B. Tsegmed, and L. Ryzhakova (2014), Solar cycle variation of "killer" electrons at geosynchronous orbit and electron flux correlation with the solar wind parameters and ULF waves intensity, *Acta Astronautica*, *93*, 55–63, doi:10.1016/j.actaastro.2013.07.004.

Reeves, G. D. (1998), Relativistic electrons and magnetic storms: 1992-1995, *Geophysical Research Letters*, *25*(11), 1817–1820, doi:10.1029/98GL01398.

Reeves, G. D., K. L. McAdams, R. H. W. Friedel, and T. P. O'Brien (2003), Acceleration and loss of relativistic electrons during geomagnetic storms, *Geophysical Research Letters*, *30*(10), n/a–n/a, doi:10.1029/2002GL016513.

Reeves, G. D., S. K. Morley, R. H. W. Friedel, M. G. Henderson, T. E. Cayton, G. Cunningham, J. B. Blake, R. A. Christensen, and D. Thomsen (2011), On the relationship between relativistic electron flux and solar wind velocity: Paulikas and Blake revisited, *Journal of Geophysical Research: Space Physics*, *116*(A2), n/a–n/a, doi:10.1029/2010JA015735.

Reeves, G. D., H. E. Spence, M. G. Henderson, S. K. Morley, R. H. W. Friedel, H. O. Funsten, D. N. Baker, S. G. Kanekal, J. B. Blake, J. F. Fennell, S. G. Claudepierre, R. M.

Thorne, D. L. Turner, C. A. Kletzing, W. S. Kurth, B. A. Larsen, and J. T. Niehof (2013), Electron Acceleration in the Heart of the Van Allen Radiation Belts, *Science*, *341*(6149), 991–994, doi:10.1126/science.1237743.

Reeves, G. D., R. H. W. Friedel, B. A. Larsen, R. M. Skoug, H. O. Funsten, S. G. Claudepierre, J. F. Fennell, D. L. Turner, M. H. Denton, H. E. Spence, J. B. Blake, and D. N. Baker (2016), Energy-dependent dynamics of keV to MeV electrons in the inner zone, outer zone, and slot regions, *Journal of Geophysical Research: Space Physics*, *121*(1), 397–412, doi:10.1002/2015JA021569.

Rodger, C. J., K. Cresswell-Moorcock, and M. A. Clilverd (2016), Nature's Grand Experiment: Linkage between magnetospheric convection and the radiation belts, *Journal of Geophysical Research: Space Physics*, *121*(1), 171–189, doi:10.1002/2015JA021537.

Rodriguez, J. V., J. C. Krosschell, and J. C. Green (2014), Intercalibration of GOES 8-15 solar proton detectors, *Space Weather*, *12*(1), 92–109, doi:10.1002/2013SW000996.

Rostoker, G., S. Skone, and D. N. Baker (1998), On the origin of relativistic electrons in the magnetosphere associated with some geomagnetic storms, *Geophysical Research Letters*, *25*(19), 3701–3704, doi:10.1029/98GL02801.

Sandanger, M., F. Søraas, K. Aarsnes, K. Oksavik, and D. S. Evans (2007), Loss of relativistic electrons: Evidence for pitch angle scattering by electromagnetic ion cyclotron waves excited by unstable ring current protons, *Journal of Geophysical Research: Space Physics*, *112*(A12), n/a–n/a, doi:10.1029/2006JA012138.

Schiller, Q., X. Li, L. Blum, W. Tu, D. L. Turner, and J. B. Blake (2014), A nonstorm time enhancement of relativistic electrons in the outer radiation belt, *Geophysical Research Letters*, *41*(1), 7–12, doi:10.1002/2013GL058485.

Schiller, Q., S. G. Kanekal, L. K. Jian, X. Li, A. Jones, D. N. Baker, A. Jaynes, and H. E. Spence (2016), Prompt injections of highly relativistic electrons induced by interplanetary shocks: A statistical study of Van Allen Probes observations: Shock-Induced Injections and Depletions, *Geophysical Research Letters*, doi:10.1002/2016GL071628.

Schulz, M., and L. J. Lanzerotti (1974), *Particle Diffusion in the Radiation Belts*, *Physics and Chemistry in Space*, vol. 7, Springer Berlin Heidelberg, Berlin, Heidelberg, doi: 10.1007/978-3-642-65675-0.

Selesnick, R. S., D. N. Baker, A. N. Jaynes, X. Li, S. G. Kanekal, M. K. Hudson, and B. T. Kress (2014), Observations of the inner radiation belt: CRAND and trapped solar protons, *J. Geophys. Res. Space Physics*, *119*(8), 6541–6552, doi:10.1002/2014JA020188.

Shen, X.-C., M. K. Hudson, A. N. Jaynes, Q. Shi, A. Tian, S. G. Claudepierre, M.-R. Qin, Q.-G. Zong, and W.-J. Sun (2017), Statistical study of the storm time radiation belt evolution during Van Allen Probes era: CME- versus CIR-driven storms, *Journal of Geophysical Research: Space Physics*, *122*(8), 8327–8339, doi:10.1002/2017JA024100.

Shprits, Y. Y., R. M. Thorne, R. Friedel, G. D. Reeves, J. Fennell, D. N. Baker, and S. G. Kanekal (2006), Outward radial diffusion driven by losses at magnetopause, *Journal of Geophysical Research*, *111*(A11), doi:10.1029/2006JA011657.

Shprits, Y. Y., D. Subbotin, A. Drozdov, M. E. Usanova, A. Kellerman, K. Orlova, D. N. Baker, D. L. Turner, and K.-C. Kim (2013), Unusual stable trapping of the ultrarelativistic electrons in the Van Allen radiation belts, *Nature Physics*, *9*(11), 699–703, doi: 10.1038/nphys2760.

Shprits, Y. Y., R. B. Horne, A. C. Kellerman, and A. Y. Drozdov (2018), The dynamics of Van Allen belts revisited, *Nature Physics*, *14*(2), 102–103, doi:10.1038/nphys4350.

Shue, J.-H., P. Song, C. T. Russell, J. T. Steinberg, J. K. Chao, G. Zastenker, O. L. Vaisberg, S. Kokubun, H. J. Singer, T. R. Detman, and H. Kawano (1998), Magnetopause location under extreme solar wind conditions, *Journal of Geophysical Research: Space Physics*, *103*(A8), 17,691–17,700, doi:10.1029/98JA01103.

Simms, L. E., V. Pilipenko, M. J. Engebretson, G. D. Reeves, A. J. Smith, and M. Clilverd (2014), Prediction of relativistic electron flux at geostationary orbit following storms: Multiple regression analysis, *Journal of Geophysical Research: Space Physics*, *119*(9), 7297–7318, doi:10.1002/2014JA019955.

Simms, L. E., M. J. Engebretson, V. Pilipenko, G. D. Reeves, and M. Clilverd (2016), Empirical predictive models of daily relativistic electron flux at geostationary orbit: Multiple regression analysis, *Journal of Geophysical Research: Space Physics*, *121*(4), 3181–3197, doi:10.1002/2016JA022414.

Spasojevic, M., Y. Y. Shprits, and K. Orlova (2015), Global empirical models of plasmaspheric hiss using Van Allen Probes, *Journal of Geophysical Research: Space Physics*, *120*(12), 10,370–10,383, doi:10.1002/2015JA021803.

Spence, H. E., G. D. Reeves, D. N. Baker, J. B. Blake, M. Bolton, S. Bourdarie, A. A. Chan, S. G. Claudepierre, J. H. Clemmons, J. P. Cravens, S. R. Elkington, J. F. Fennell, R. H. W. Friedel, H. O. Funsten, J. Goldstein, J. C. Green, A. Guthrie, M. G. Henderson, R. B. Horne, M. K. Hudson, J.-M. Jahn, V. K. Jordanova, S. G. Kanekal, B. W. Klatt, B. A. Larsen, X. Li, E. A. MacDonald, I. R. Mann, J. Niehof, T. P. O'Brien, T. G. Onsager, D. Salvaggio, R. M. Skoug, S. S. Smith, L. L. Suther, M. F. Thomsen, and R. M. Thorne (2013), Science Goals and Overview of the Radiation Belt Storm Probes (RBSP) Energetic Particle, Composition, and Thermal Plasma (ECT) Suite on NASA's Van Allen Probes Mission, *Space Science Reviews*, *179*(1-4), 311–336, doi:10.1007/s11214-013-0007-5.

Su, Z., F. Xiao, H. Zheng, Z. He, H. Zhu, M. Zhang, C. Shen, Y. Wang, S. Wang, C. A. Kletzing, W. S. Kurth, G. B. Hospodarsky, H. E. Spence, G. D. Reeves, H. O. Funsten, J. B. Blake, and D. N. Baker (2014), Nonstorm time dynamics of electron radiation belts observed by the Van Allen Probes, *Geophysical Research Letters*, *41*(2), 229–235, doi:10.1002/2013GL058912.

Su, Z., N. Liu, H. Zheng, Y. Wang, and S. Wang (2018), Multipoint Observations of Nightside Plasmaspheric Hiss Generated by Substorm-Injected Electrons, *Geophysical Research Letters*, *45*(20), 10,921–10,932, doi:10.1029/2018GL079927.

Summers, D. (2003), Relativistic electron pitch-angle scattering by electromagnetic ion cyclotron waves during geomagnetic storms, *Journal of Geophysical Research*, *108*(A4), doi:10.1029/2002JA009489.

Summers, D., R. M. Thorne, and F. Xiao (1998), Relativistic theory of wave-particle resonant diffusion with application to electron acceleration in the magnetosphere, *Journal of Geophysical Research: Space Physics*, *103*(A9), 20,487–20,500, doi:10.1029/98JA01740.

Tang, C. L., Y. X. Wang, B. Ni, Z. P. Su, G. D. Reeves, J. Zhang, D. N. Baker, H. E. Spence, H. O. Funsten, and J. B. Blake (2017), The effects of magnetospheric processes on relativistic electron dynamics in the Earth's outer radiation belt, *J. Geophys. Res. Space Physics*, *122*(10), 9952–9968, doi:10.1002/2017JA024407.

Thorne, R. M. (2010), Radiation belt dynamics: The importance of wave-particle interactions, *Geophysical Research Letters*, *37*(22), n/a–n/a, doi:10.1029/2010GL044990.

Thorne, R. M., and C. F. Kennel (1971), Relativistic electron precipitation during magnetic storm main phase, *Journal of Geophysical Research*, *76*(19), 4446–4453, doi:10.1029/JA076i019p04446.

Thorne, R. M., W. Li, B. Ni, Q. Ma, J. Bortnik, L. Chen, D. N. Baker, H. E. Spence, G. D. Reeves, M. G. Henderson, C. A. Kletzing, W. S. Kurth, G. B. Hospodarsky, J. B. Blake, J. F. Fennell, S. G. Claudepierre, and S. G. Kanekal (2013a), Rapid local acceleration of relativistic radiation-belt electrons by magnetospheric chorus, *Nature*, *504*(7480), 411–414, doi:10.1038/nature12889.

Thorne, R. M., W. Li, B. Ni, Q. Ma, J. Bortnik, D. N. Baker, H. E. Spence, G. D. Reeves, M. G. Henderson, C. A. Kletzing, W. S. Kurth, G. B. Hospodarsky, D. Turner, and V. Angelopoulos (2013b), Evolution and slow decay of an unusual narrow ring of relativistic electrons near L ~ 3.2 following the September 2012 magnetic storm, *Geophysical Research Letters*, *40*(14), 3507–3511, doi:10.1002/grl.50627.

Tsurutani, B. T., S. A. Park, B. J. Falkowski, G. S. Lakhina, J. S. Pickett, J. Bortnik, G. Hospodarsky, O. Santolik, M. Parrot, P. Henri, and R. Hajra (2018), Plasmaspheric Hiss: Coherent and Intense, *Journal of Geophysical Research: Space Physics*, doi: 10.1029/2018JA025975.

Turner, D. L., and X. Li (2008), Quantitative forecast of relativistic electron flux at geosynchronous orbit based on low-energy electron flux, *Space Weather*, *6*(5), n/a–n/a, doi: 10.1029/2007SW000354.

Turner, D. L., Y. Shprits, M. Hartinger, and V. Angelopoulos (2012), Explaining sudden losses of outer radiation belt electrons during geomagnetic storms, *Nature Physics*, *8*(3), 208–212, doi:10.1038/nphys2185.

Turner, D. L., V. Angelopoulos, W. Li, M. D. Hartinger, M. Usanova, I. R. Mann, J. Bortnik, and Y. Shprits (2013), On the storm-time evolution of relativistic electron phase space density in Earth's outer radiation belt, *Journal of Geophysical Research: Space Physics*, *118*(5), 2196–2212, doi:10.1002/jgra.50151.

Turner, D. L., T. P. O'Brien, J. F. Fennell, S. G. Claudepierre, J. B. Blake, E. K. J. Kilpua, and H. Hietala (2015), The effects of geomagnetic storms on electrons in Earth's radiation belts, *Geophysical Research Letters*, *42*(21), 9176–9184, doi:10.1002/2015GL064747.

Turner, D. L., E. K. J. Kilpua, H. Hietala, S. G. Claudepierre, T. P. O'Brien, J. F. Fennell, J. B. Blake, A. N. Jaynes, S. Kanekal, D. N. Baker, H. E. Spence, J.-F. Ripoll, and G. D. Reeves (2019), The response of Earth's electron radiation belts to geomagnetic storms: Statistics from the Van Allen Probes era including effects from different storm drivers, *Journal of Geophysical Research: Space Physics*, doi:10.1029/2018JA026066.

Tverskaya, L., N. Pavlov, J. Blake, R. Selesnick, and J. Fennell (2003), Predicting the L-position of the storm-injected relativistic electron belt, *Advances in Space Research*, *31*(4), 1039–1044, doi:10.1016/S0273-1177(02)00785-8.

Usanova, M. E., A. Drozdov, K. Orlova, I. R. Mann, Y. Shprits, M. T. Robertson, D. L. Turner, D. K. Milling, A. Kale, D. N. Baker, S. A. Thaller, G. D. Reeves, H. E. Spence,

C. Kletzing, and J. Wygant (2014), Effect of EMIC waves on relativistic and ultrarelativistic electron populations: Ground-based and Van Allen Probes observations: Usanova et al.: EMIC Waves and Relativistic Electrons, *Geophysical Research Letters*, *41*(5), 1375–1381, doi:10.1002/2013GL059024.

Van Allen, J. A., and L. A. Frank (1959), Radiation Around the Earth to a Radial Distance of 107,400 km., *Nature*, *183*(4659), 430–434, doi:10.1038/183430a0.

Wing, S., J. R. Johnson, E. Camporeale, and G. D. Reeves (2016), Information theoretical approach to discovering solar wind drivers of the outer radiation belt, *Journal of Geophysical Research: Space Physics*, *121*(10), 9378–9399, doi:10.1002/2016JA022711.

Wrenn, G. (2009), Chronology of 'killer' electrons: Solar cycles 22 and 23, *Journal of Atmospheric and Solar-Terrestrial Physics*, *71*(10-11), 1210–1218, doi:10.1016/j.jastp.2008.08.002.

Wrenn, G. L., D. J. Rodgers, and K. A. Ryden (2002), A solar cycle of spacecraft anomalies due to internal charging, *Annales Geophysicae*, *20*(7), 953–956, doi:10.5194/angeo-20-953-2002.

Wygant, J. R., J. W. Bonnell, K. Goetz, R. E. Ergun, F. S. Mozer, S. D. Bale, M. Ludlam, P. Turin, P. R. Harvey, R. Hochmann, K. Harps, G. Dalton, J. McCauley, W. Rachelson, D. Gordon, B. Donakowski, C. Shultz, C. Smith, M. Diaz-Aguado, J. Fischer, S. Heavner, P. Berg, D. M. Malsapina, M. K. Bolton, M. Hudson, R. J. Strangeway, D. N. Baker, X. Li, J. Albert, J. C. Foster, C. C. Chaston, I. Mann, E. Donovan, C. M. Cully, C. A. Cattell, V. Krasnoselskikh, K. Kersten, A. Brenneman, and J. B. Tao (2013), The Electric Field and Waves Instruments on the Radiation Belt Storm Probes Mission, *Space Sci Rev*, *179*(1-4), 183–220, doi:10.1007/s11214-013-0013-7.

Xiong, Y., L. Xie, Z. Pu, S. Fu, L. Chen, B. Ni, W. Li, J. Li, R. Guo, and G. K. Parks (2015), Responses of relativistic electron fluxes in the outer radiation belt to geomagnetic storms, *Journal of Geophysical Research: Space Physics*, *120*(11), 9513–9523, doi:10.1002/2015JA021440.

Xiong, Y., L. Xie, L. Chen, B. Ni, S. Fu, and Z. Pu (2018), The Response of the Energy Content of the Outer Electron Radiation Belt to Geomagnetic Storms, *Journal of Geophysical Research: Space Physics*, *123*(10), 8227–8240, doi:10.1029/2018JA025475.

Yuan, C., and Q. Zong (2013a), The double-belt outer radiation belt during CME- and CIR-driven geomagnetic storms, *Journal of Geophysical Research: Space Physics*, *118*(10), 6291–6301, doi:10.1002/jgra.50564.

Yuan, C., and Q. Zong (2013b), Relativistic electron fluxes dropout in the outer radiation belt under different solar wind conditions, *Journal of Geophysical Research: Space Physics*, *118*(12), 7545–7556, doi:10.1002/2013JA019066.

Yuan, C., and Q. Zong (2019), The Efficiency of Coronal Mass Ejection With Different IMF Preconditions on the Production of Megaelectronvolt Electron Content in the Outer Radiation Belt, *J. Geophys. Res. Space Physics*, *124*(5), 3222–3235, doi:10.1029/2018JA026263.

Yuan, C. J., and Q.-G. Zong (2012), Quantitative aspects of variations of 1.5-6.0 MeV electrons in the outer radiation belt during magnetic storms, *Journal of Geophysical Research: Space Physics*, *117*(A11), n/a–n/a, doi:10.1029/2011JA017346.

Zhang, X.-J., W. Li, R. M. Thorne, V. Angelopoulos, J. Bortnik, C. A. Kletzing, W. S. Kurth, and G. B. Hospodarsky (2016), Statistical distribution of EMIC wave spectra: Observations from Van Allen Probes, *Geophysical Research Letters*, *43*(24), 12,348–12,355, doi:10.1002/2016GL071158.

Zhang, X.-J., D. Mourenas, A. V. Artemyev, V. Angelopoulos, and R. M. Thorne (2017), Contemporaneous EMIC and whistler mode waves: Observations and consequences for MeV electron loss, *Geophysical Research Letters*, *44*(16), 8113–8121, doi:10.1002/2017GL073886.

Zhao, H., and X. Li (2013), Inward shift of outer radiation belt electrons as a function of *Dst* index and the influence of the solar wind on electron injections into the slot region, *Journal of Geophysical Research: Space Physics*, *118*(2), 756–764, doi: 10.1029/2012JA018179.

Zhao, H., D. N. Baker, X. Li, A. N. Jaynes, and S. G. Kanekal (2019), The effects of geomagnetic storms and solar wind conditions on the ultrarelativistic electron flux enhancements, *Journal of Geophysical Research: Space Physics*, doi:10.1029/2018JA026257.